12-2013

Understanding Mechanical and Fatigue Behavior of a Wrought Magnesium Alloy using In-situ Neutron and Synchrotron X-ray Diffraction

Wei Wu
University of Tennessee - Knoxville, wwu7@utk.edu

To the Graduate Council:

I am submitting herewith a dissertation written by Wei Wu entitled "Understanding Mechanical and Fatigue Behavior of a Wrought Magnesium Alloy using In-situ Neutron and Synchrotron X-ray Diffraction." I have examined the final electronic copy of this dissertation for form and content and recommend that it be accepted in partial fulfillment of the requirements for the degree of Doctor of Philosophy, with a major in Materials Science and Engineering.

Peter K. Liaw, Major Professor

We have read this dissertation and recommend its acceptance:

Ke An, Yanfei Gao, John D. Landes

Accepted for the Council:

Carolyn R. Hodges

Vice Provost and Dean of the Graduate School

(Original signatures are on file with official student records.)

Understanding Mechanical and Fatigue Behavior of a Wrought Magnesium Alloy using In-situ Neutron and Synchrotron X-ray Diffraction

A Dissertation Presented for the
Doctor of Philosophy
Degree
The University of Tennessee, Knoxville

Wei Wu
December 2013

DEDICATION

This work is dedicated to my beloved wife, Lu Huang, who is my sincere colleague, my dearest friend, and the love of my life. And also, to my parents, Kun Wu and Jing Shi, my father- and mother-in-law, Xianming Huang and Weiping Liu, my sister-in-law and her husband, Si Huang and Min Zheng, and the rest of my family, for believing in me, supporting me, and inspiring me.

ACKNOWLEDGEMENTS

I would like to express my utmost gratitude and appreciation to my advisor Dr. Peter K. Liaw, who has been providing me abundant environments and resources to extend my potentials, and inspiring me for my academic research throughout these yeaers. I would like to convey my deep regards to my sincere friend and mentor, Dr. Ke An for his valuable guidance and constructive discussions. I am thankful to Dr. Yanfei Gao for his comprehensive instruction and advice in this work. I wish to express my gratitude to Dr. John D. Landes for his kind suggestions on the fatigue study. Special thanks should be given to Dr. Anna M. Paradowska and Shuyan Zhang at at the ISIS Facility, Rutherford Appleton Laboratory, Dr. Xu Chen from Tianjin University, China, Dr. Alexandru Dan Stoica, and Mr. Harley David Skorpenske from Oak Ridge National Laboratory (ORNL), Dr. Wenjun Liu and Dr. Yang Ren from Argonne National Laboratory, and Dr. Peidong Wu from McMaster University, Canada, for their generous help on neutron and synchrotron X-ray diffraction measurements, as well as theoretical modeling. I also want to thank my great friend, Mr. Douglas E. Fielden, and his team, Mr. Larry D. Smith, and Mr. Dan Hackworth, for their kind help and great efforts on technical supports in the past five years.

I would also like to thank our group members and my friends for their kindness during my Ph.D. study. Many thanks to Dr. Gongyao Wang, Dr. Liang Wu, Dr. Soo Yoel Lee, Dr. E-Wen Huang, Dr. Jiawan Tian, Dr. Fengxiao Liu, Dr. Dongchun Qiao, Dr. Feng Jiang, Dr. Zhenke Tnag, Dr. Shenyan Huang, Dr. Li Li, Dr. Matthew W. Freels, Mr. Andrew Chuang, Mr. Zhinan An, Mr. Wei Guo, Mr. Xie Xie, Mr. Haolin Jia, Mr. Zhi

Tang, Mr. Bilin Chen, Mr. Zhiqian Sun, Mr. Louis J. Santodonato, Mr. Michael A Hemphill, Ms. Haoyan Diao, and Ms. Lu Huang.

I am grateful for the financial support from Columbus McKinnon Corporation and a Laboratory Directed Research and Development (LDRD) project of ORNL.

ABSTRACT

Magnesium (Mg) alloys have received great attentions in the past several decades, due to their unique properties of low density, high strength-to-weight ratio, and high specific stiffness. Previous work on fatigue behavior of Mg alloys typically relies on ex situ microstructural characterization and crack-growth monitoring with replica techniques. The *primary* challenge is thus the lack of an *in situ*, non-destructive measurement on microstructural length scales, which prevents us from linking the stress analyses (top-down point of view) to the failure mechanisms on inter- and intra-granular scales (bottom-up point of view). A unique opportunity that resolves many of these difficulties and challenges is provided by in situ neutron and synchrotron X-ray diffraction methods, which provide the unprecedented information on inter- and intra-granular deformation characteristics at different length scales from mm to sub-μm.

The *primary objective* aims to identify deformation mechanisms during strain-path changes, low-cycle fatigue, and fatigue crack growth tests of Mg alloys from in-situ diffraction and micromechanical studies. We took advantage of the state-of-art VULCAN engineering materials diffractometer of Spallation Neutron Source (SNS), Oak Ridge National Laboratory (ORNL) to achieve the real in-situ neutron diffraction measurement. Instead of the "traditional" step loading method, the neutron diffraction measurements were performed under continuous loading condition at a slow loading rate, which provided the detailed information related to the plastic deformation dynamics of the wrought magnesium alloy. Full-field mapping around fatigue cracks can be performed at ISIS facility, Rutherford Appleton Laboratory, UK. The multiscale nature of deformation

near the fatigue crack tip permits a scale-bridging modeling method. Moreover, the twinning and detwinning behavior in an individual grain inside a polycrystalline wrought Mg alloy has been investigated using sub-micron level synchrotron X-ray microbeam diffraction at 34ID-E, Advanced Photon Source (APS), Argonne National Laboratory (ANL), USA.

Critical issues lie on the deformation dynamics, twinning-detwinning behavior at the grain level, and fatigue crack growth mechanisms.

The *principal outcome* of this research will be the improved microstructural level understanding on deformation dynamics and fatigue mechanisms with which materials scientists can improve the practical applications of Mg alloys.

TABLE OF CONTENTS

LIST OF TABLES

LIST OF FIGURES

CHAPTER 1
INTRODUCTION AND GENERAL INFORMATION

Magnesium (Mg) alloys draw great attention to the science and engineering societies and industries, due to the combined properties of low density (2/3 that of aluminum and 1/4 that of iron), high strength-to-weight ratio, and high specific stiffness [1-5]. Mg alloys have a great potential to reduce the vehicle weight, fuel consumption, and greenhouse-gas emissions. At present, cast Mg alloys take a predominant position over wrought ones, in view of their high productivity, good surface quality, and acceptable dimensional precision. The cast Mg alloys can be used as parts on mechanical systems of automobiles, such as steering wheels, seats, instrument panels, gear boxes, air-intake systems, gearboxes housings, stretchers, tank covers, etc. [5, 6]. Moreover, Mg alloys can be employed as canning materials at the nuclear-power stations [7]. However, the structural components made from wrought alloys have much greater advantage over cast alloys, since the mechanical properties, including the fatigue resistance, of wrought alloys are better than cast alloys [8-12]. Moreover, most of the wrought Mg alloys are heat treatable [13-17]. Therefore, the mechanical properties can be further improved by adjusting the heat-treatment parameters. Furthermore, because wrought Mg alloys are basically defect-free, the research on wrought Mg alloys may shed light on uncovering the intrinsic plastic deformation and fatigue mechanism of hexagonal-close-packed (HCP) structured polycrystalline metals [18].

1.1 Objectives

The *primary* objective aims to investigate the deformation dynamics, low-cycle fatigue mechanisms, and fatigue crack growth mechanisms of Mg alloys from *in situ* diffraction and constitutive modeling. This study allows us to achieve the improved fatigue resistance by tuning the texture, plastic anisotropy, and loading/crack orientations. Thus, materials of interests include commercially available rolled AZ31B Mg alloys. The synergy between experiments and modeling is focused on the following two scientific keywords:

(1) *Plastic Anisotropy*: Yield and flow characteristics of Mg alloys are very sensitive to the polar nature of twin deformation, texture, and thus loading directions and stress multiaxiality. Neutron and synchrotron X-ray diffraction experiments provide the inter- and intra-granular strains, as well as texture evolution information, which can be directly compared with the combination of elastic-viscoplastic self-consistent (EVPSC) polycrystal model with the newly-developed twinning and de-twinning (TDT) model that treats slip and twin explicitly. Such micromechanical comparisons will validate their predictive capabilities for deformation dynamics, especially, the twinning-detwinning behavior, in HCP-structured Mg alloy.

(2) *Fatigue resistance*: The low-cycle fatigue and fatigue crack growth behavior can be investigated using *in situ* diffraction techniques to connect the macroscopic fatigue behavior with microscopic response in a grain level.

The *principal outcome* of this research will be a microstructural level understanding with which materials scientists can improve the practical applications of Mg alloys. It can also have profound impacts on deformation and failure studies of advanced structural materials.

1.2 Outline of the Research

Although significant advances have been developed in fatigue mechanics [19-21], most of previous studies on fatigue performance of wrought Mg alloys rely on mechanical testing, microstructural characterizations, and fractography using optical and electron microscopes, and crack growth monitoring with replica techniques, among many others [8, 22-33]. These studies result in a limited knowledge on the real-time relationship between the macroscopic mechanical behavior and microscopic mechanisms. *In situ* investigations such as the scanning electron microscopy (SEM) and transmission electron microscopy (TEM) [29-34], or electron backscatter diffraction (EBSD) [26-28, 35-37], however, are limited to surface or thin-film information. Consequently, our limited knowledge of material lifetime and failure mechanisms place the ultimate restrictions on technological viability of this class of light-weight materials. : A comparison of literature and proposed work on the study of Mg alloys is illustrated in Fig. 1.1.

A unique opportunity that resolves many of the above difficulties and challenges lies on the *in situ* neutron and synchrotron X-ray diffraction techniques. These advanced nondestructive tools offer us a great opportunity to establish the relationship between macroscopic properties and microstructural mechanisms, including the unprecedented

information on: (i) lattice strain evolution, which relies on intergranular interactions and thus illustrates the deformation anisotropy at the grain scale, (ii) intragranular strains from the line profile analysis that provides the information on dislocations and twin fractions, and (iii) texture evolution from the peak intensity development. Consequently, the following advantages can be taken to investigate the plasticity and fatigue mechanisms of Mg alloys (the schematic is presented in Fig. 1.2):

(1) A recent advancement of our collaborative effort with the Spallation Neutron Source (SNS) at the Oak Ridge National Laboratory (ORNL) enables the real-time, *in situ* neutron diffraction measurements under continuous loading conditions utilizing the state-of-the-art VULCAN Engineering diffractometer [38-40]. These capabilities are of critical importance in understanding the lattice strains and texture evolution. The effect of initial texture and previous deformation history on plastic deformation of a wrought AZ31B Mg alloy under monotonic tension/compression will be addressed.

(2) *In situ* measurements of the twinning-detwinning behavior at a grain level has not been fully explored. The previous techniques cannot provide the information within grains, since they provide an average of all grains which contribute to a given diffraction peak based upon the Bragg condition. By employing the cutting-edge three-dimensional (3D) X-ray microbeam diffraction technique at Advanced Photon Source (APS), Argonne National Laboratory (ANL) [41, 42], the study of the reorientation, intragranular strain, and twin evolution within individual grains become feasible. The investigation of twinning-detwinning behavior in a single

grain inside a polycrystalline wrought AZ31B Mg alloy will be performed in-situ during monotonic compression-tension.

(3) The effect of initial texture, strain amplitude, and deformation history on uniaxial low-cycle fatigue behavior of a wrought AZ31B Mg alloy will be studied using real-time in-situ neutron diffraction under continuous loading condition at VULCAN, SNS, ORNL.

(4) The combination of neutron and synchrotron X-ray techniques allows different investigation windows at microstructure and sub-grain scales. To this end, neutron and synchrotron X-ray diffraction [43-50] have been successfully employed in research on wrought Mg alloys. However, these studies are only limited to simple stress states and monotonic loadings. The effect of initial texture and a single overload on fatigue crack growth behavior of a wrought AZ31B Mg alloy will be investigate using in-situ neutron diffraction.

(5) The combination of elastic-viscoplastic self-consistent (EVPSC) polycrystal model with the newly-developed twinning and de-twinning (TDT) model will be applied for interpreting the real-time in-situ neutron diffraction data from uniaxial tension/compression and low-cycle fatigue.

CHAPTER 2
LITERATURE REVIEW

2.1 Deformation Mechanism in Mg

2.1.1 Deformation systems in Mg

According to the Von Mises criterion, in order to achieve arbitrary homogenous deformation for polycrystalline materials, five independent slip systems are necessary. In principle, magnesium possesses five independent slip systems, as shown in Fig. 2.1. Two independent basal-slip systems in the close-packed direction 1/3<11.0> or <a> on the basal {00.2} plane usually were referred as primary deformation mode in Mg. The incorporation of non-basal-slip systems, <a> on a prismatic {10.0} plane, <a> on the first order pyramidal {10.1} plane, and the second order pyramidal <c + a> slip system {11.2}<11.3> offer three more independent slip systems [47, 51-53]. It should be pointed out that the <c + a> slip system is the only one, which is capable of accommodating strains along the crystallographic <c> direction. However, it is difficult to activate at room temperature due to the high critical resolved shear stress (CRSS) [54]. On the other hand, the mechanical twinning offers an additional independent deformation mode to satisfy the Von Mises criterion, but in a limited sense, due to their unidirectional nature and their limited strain accommodating ability.

2.1.2 Deformation twinning in Mg

Unlike dislocation slip, deformation twinning is a polar (unidirectional deformation) by its nature, thus, the shear can only occur in one direction rather than opposite direction [47, 55, 56]. Twinning modes in HCP metals are distinguished by their

ability to produce either tensile or compressive strain along the crystallographic *c*-axis, but not both. A single twin system can only operate once in a given sample volume unless the strain path is changed. Depending upon the *c*/*a* axial ratio, HCP twinning modes may be either tensile or compressive.

Because the *c*/*a* axial ratio of Mg is $1.624 < \sqrt{3}$, the most prominent twinning in HCP Mg alloys is {10.2}<10.1> tensile twinning (or extension twinning), which results in a tensile strain parallel to the c-axis (a basal pole) or a compression strain perpendicular to the c-axis (a basal pole) [45, 57-59]. Therefore, {10.2}<10.1> tensile twinning in Mg will operate efficiently as tension along the c-axis or compression perpendicular to the c-axis, as presented in Fig. 2.2(a). The tensile twinning will results in a sudden re-orientation of matrix lattice approximate 86.3^{o}, as demonstrated in Fig. 2.2(b). When the tension direction parallel to the c-axis at room temperature, the <a> dislocation slip cannot operate, which makes the tensile twinning the only active deformation mode providing the straining along c-axis. The unfavorable grains for slip can be re-orientated into a favorable orientation, because of the tensile twinning. In polycrystalline Mg alloys, the tensile twinning is activated during the deformation of randomly textured cast materials at high strain rate and low-temperature, and when uniaxial compression is applied along the extrusion direction of extrusion, or along a direction in the rolling plane of plate or sheet [60-62].

Contraction twinning, including {10.1}<10.2> and {10.3}<10.2> twins, can accommodate compression along the c-axis [40, 61, 63-65]. It is activated when there is a compression strain component parallel to the basal pole or when extension is applied

perpendicular to the basal pole, which results in a lattice rotation (approximately 56.2^{o}) towards a more favorable orientation for basal glide, as shown in Fig. 2.3(b).

In addition to primary twinning, secondary twinning can take place within the reoriented primary twins, mainly because a stress state that favors the nucleation of primary contraction twinning will also support secondary extension twinning within the primary twin domain, i.e., the orientation of contraction twinning, {10.1}<10.2> or {10.3}<10.2>, favors the subsequent extension twinning, {10.2}<10.1> [36, 37, 66]. The schematic of double-twinning systems in Mg is illustrated in Fig. 2.3(c), (d), and (e). For {10.1}-{10.2} double twinning, the basal planes are reoriented at an angle of 37.5^{o} around $<1\bar{2}.0>$ direction from their original positions in the untwined matrix. Similarly, for {10.3}-{10.2} double twinning, the basal plane rotates an angle of 29.7^{o} around $<1\bar{2}.0>$ direction. The combination of twinning operations found in double-twins lead to 36 possible final twinned orientations for a given initial orientation, which can be further categorized into four geometrically equivalent types. An important consequence of double-twinning is that the basal plane is reoriented to facilitate the slip, which causes crystallographic softening within the compression twins. The {10.1}-{10.2} double twinning in polycrystalline Mg alloys might result in the premature shear failure, due to the strain softening and localized void formation. Besides the primary contraction-secondary extension twins, {10.1}-{10.2} and {10.3}-{10.2} double twinning, {10.2}-{10.2} double-tensile-twinning has been observed by other researchers [36].

Because deformation twins grow so fast, the nucleation structure is difficult to observe experimentally. The research subject to the deformation twinning nucleation and

growth in HCP structured Mg is very limited. Very recently, Yu and co-workers [34] reported the origin of deformation twinning in a [00.2]-orientated single crystal Mg pillar, as demonstrated in Fig. 2.4(a), prepared by focused ion beam (FIB), employing in-situ TEM observations with unprecedented spatial resolution. It found that a large amount of {10.2} extension twins were initiated during tension tests, accompanying with a sudden load drop. After the formation of nanotwins, in Fig. 2.4(b), an obvious strain hardening was presented, due to a large number of nanotwin boundaries serve as obstacles for the dislocation motion. However, the nucleation of a single {10.1} contraction twins during compression initiated from the corner of the contact surface between the sample and the indenter. Then, this single twin grew gradually as the stress increased continuously until the twin extended across the entire width of the pillar. It results in the strain softening resulting from fully accommodated dislocation activity and the escape of dislocations at the surfaces, in Fig. 2.4(c).

Nucleation and growth of twins are affected by metallurgical conditions like temperature, strain rate, grain size, prestrain and precipitates [58, 67, 68]. Generally speaking, small grain size suppresses twinning nucleation [69, 70]. For smaller grain size ranging from 17 to 30 μm, slip was predominant. For larger grain size ranging from 30 to 87 μm, twinning was dominant [71]. Moreover, twin nucleation in iron [72], niobium [73] and chromium [74] was suppressed by a small prestrain imposed at higher temperatures, where uniform dislocation distribution was more efficient in suppressing twinning than heterogeneous one, simply because the slip was favored during the competition of twinning and slip. Precipitates had similar effects on twinning.

2.2 Plastic Deformation of Mg Alloys under Uniaxial Loading

The plastic deformation of wrought Mg alloys is characterized by a high tension-compression asymmetry and significant anisotropy arising from the texture, polar nature of twinning, limited number of slip systems, and the loading-direction dependence on the activation of different deformation modes [51, 52, 75]. The wrought Mg alloys usually possess strong initial texture. In rolled Mg alloys, the c-axis of nearly all grains tends to align in plate-normal direction, ND (or through thickness direction), and vertical to the rolling direction, RD. In extruded Mg alloys, the basal-plane normal of almost all grains tends to distribute in radial direction and perpendicular to the extrusion direction. It has been established that tensile twinning will be activated during in-plane compression or through-thickness tension [51, 52]. In both of these cases, the dominant slip system, basal <a> slip, cannot operate because the resolved shear stress is zero. Usually, a low yielding strength and a low initial hardening rate, followed by a rapid increase of hardening once the twinning is exhausted, are observed in a twinning-dominant deformation mode [Fig. 2.5(a)] [44]. Figure 2.5(b) represents the plane stress yield loci for a magnesium sheet predicted by the proposed theory and experiments (where experimental points are represented by symbols) [21]. The 1% yield locus for the textured pure magnesium has a highly asymmetrical shape.

Comprehensive researches have concentrated on the effects of the initial texture [55], strain path [28, 53, 76], strain rate [55], temperature [55], microstructure [77, 78], and grain size [79, 80] on the mechanical behavior under a uniaxial loading condition, tension and/or compression, employing a mechanical testing combined with in-situ or ex-

situ optical microscopy (OM), scanning electron microscopy (SEM), electron backscattering diffraction (EBSD), transmission electron microscopy (TEM), etc.. Figure 2.6 present the microstructure evolution for twinning dominated deformation and dislocation dominated deformation [35]. Previous researchers also applied in-situ neutron and high energy synchrotron X-ray diffraction measurements [47, 57, 80-87] to investigate the deformation mechanisms of HCP Mg alloys during discontinuous step-loading. The different dominated deformation modes were successfully distinguished from diffraction point of view subjected to the initial texture and strain path changes, as displayed in Fig. 2.7. However, since step-loading is a discontinuous measurement with limited number of measurements, it is unpractical to capture the exact moment of the transition of deformation mode or phase transformation, e.g., the transition from twinning to dislocation deformation mode in wrought magnesium alloys. Moreover, the dilemma of the experiment design for ductile materials is inevitable. In the plastic deformation region, if a stress-control mode is applied during the in-situ measurements, the strain will flow. On the other hand, the stress will relax if a strain-control mode is employed. Either way will introduce difficulties in interpretation of long-time collected data. The knowledge gap regarding the plastic deformation mechanism of Mg alloys still remains.

2.3 Low-Cycle Fatigue in Mg Alloy

Nearly 90% of all metallic failures results from fatigue during service. The fatigue can be categorized into low-cycle fatigue (LCF) and high-cycle fatigue, based on the fatigue life. Usually LCF is defined if the cycle number up to the initiation of a visible crack or until the final fracture is below 10^4 or 5×10^4 cycles. A distinguishing feature of

LCF is that the peak stresses are above the yield strength, and, hence, the strains induced usually have a noticeable plastic component.

For applications as the load-bearing component, it is vital to understand the fatigue behavior of wrought magnesium alloys. In casting magnesium alloys, defects such as casting porosity and inclusion, which commonly act as crack sources, are harmful for fatigue properties, and may facilitate fatigue crack initiation, reduce lifetimes, and decrease cyclic strength [88-92]. On the contrary, wrought magnesium alloys are basically defect-free and thus exhibit better fatigue properties than casting alloys [12, 93-95]. The wrought Mg alloys usually are highly textured materials and frequently involve twinning during plastic deformation. By tailoring the texture and the applied loading direction with respect to the initial texture, it is possible to introduce a stress state, where extension twinning {10.2}<10.1> is the only dominating deformation mode, thus isolating the effects of twinning for the convenience of the investigation. By properly aligning the sample in certain directions subjected to the tension or compression, the reoriented (~ 86.3^{o}) twin grains relative to the parent lattice could be detwinned during reverse loading. Because the polar nature of twinning and detwinning, wrought Mg alloys demonstrate unique cyclic deformation behavior and fatigue properties.

Previous fatigue studies [8, 44, 94-97] for wrought Mg alloys frequently reported that the strain–life curves exhibited a smooth transition from the low cycle fatigue regime to the high cycle fatigue regime and the strain–life curves can be described well by the Basquin (stress–life curve) and Manson–Coffin (plastic strain–life curve) equations, as

show in Fig. 2.8. The total strain amplitude can be expressed as elastic strain amplitude and plastic strain amplitude, i.e.,

$$\left(\frac{\Delta\varepsilon_t}{2}\right)=\left(\frac{\Delta\varepsilon_e}{2}\right)+\left(\frac{\Delta\varepsilon_p}{2}\right) \tag{1}$$

The elastic strain amplitude can be expressed as Basquin equation,

$$\left(\frac{\Delta\varepsilon_e}{2}\right)=\frac{\sigma'_f(2N_f)^b}{E} \tag{2}$$

The plastic strain amplitude can be expressed as the Coffin-Manson relation,

$$\left(\frac{\Delta\varepsilon_p}{2}\right)=\varepsilon'_f(2N_f)^c \tag{3}$$

Thus,

$$\frac{\Delta\varepsilon_t}{2}=\frac{\sigma'_f(2N_f)^b}{E}+\varepsilon'_f(2N_f)^c \tag{4}$$

where $\Delta\varepsilon_t$ is total strain amplitude, $\Delta\varepsilon_e$ is elastic strain amplitude, $\Delta\varepsilon_p$ is plastic strain amplitude, E is Young's modulus (for wrought AZ31B the value is roughly 45 GPa), N_f is the fatigue life, σ'_f is the fatigue strength coefficient, b is the fatigue strength exponent, ε'_f is the fatigue ductility coefficient, and c is the fatigue ductility exponent.

Comprehensive studies have been concentrated on the effects of strain amplitude [8, 98, 99], mean stress [100-102], strain ratio [93, 95, 102, 103], strain rate [103], microstructure [77, 93, 104, 105], grain size [106, 107], rare earth elements [108-110], Hysteresis energy [100], heat-treatment [111], temperature [92], environment[112-114], and initial texture [44, 115-118] on fully reversed strain-controlled low-cycle fatigue

behavior of wrought Mg alloys. Moreover, in the last decade, progress has been made in theoretical modeling to describe and predict the slip, twinning, and detwinning behavior in HCP-structured material during strain-path changes and cyclic loading [51, 60, 119-131]. Overall, the low-cycle fatigue life of wrought Mg alloys increased with the decrease of strain amplitude, strain ratio, and mean stress, as well as the increase of strain rate. The previous fatigue studies [8, 44, 94-97, 118] demonstrated the strain–life curves can be described well by the Basquin and Manson–Coffin equations, as well as the Holloman relation. Recently, it has been found that a clear kink point around 0.5% total strain (the low-cycle fatigue was conducted at a total strain of 0.5%) can be observed from the strain amplitude - fatigue life curve in extruded AZ61 and ZK60 Mg alloys, indicating the dislocation and twinning-detwinning deformation modes were dominated below and above 0.5% total strain, respectively [102, 104, 132]. Therefore, the twinning and detwinning usually involved in the fully-reversed strain-controlled low-cycle fatigue for the relatively large total strain, which has been proven experimentally by optical microscopy [93], in-situ electron backscatter diffraction (EBSD) [133], in-situ transmission electron microscopy (TEM) [34, 134], and in-situ neutron diffraction measurements [43-45, 135]. The twinning and detwinning during the cyclic loading is thought to be the main reason for the strong tension-compression asymmetry of the hysteresis loops. However, the prior in-situ experiments were commonly employed discontinuous step-loading methods, which contains only a limited number of measurements. For example, the aforementioned in-situ neutron diffraction experiments [135] only cover seven data points per cycle, which is certainly not enough to describe a fatigue cycle. The other in-situ neutron diffraction experiments [43-45] were investigated

in detail in the first cycle; however, only a limited number of data per fatigue cycle were measured in the following fatigue tests. Hence, the understanding on deformation mechanisms of wrought Mg alloys during low-cycle fatigue cycles remains incomplete. Figure 2.9 demonstrated the microstructure evolution during a fatigue cycle [133]. Note that blue arrows: twins kept stable after unloading from compression but became thinner under tensile loading; black arrows: the twins kept stable after unloading from compression but disappeared after tensile loading; white arrows: the twins became smaller after unloading from compression and became much smaller under subsequent tensile loading; red arrows: the twins became smaller due to unloading from compression and disappeared after tensile loading. The twinning and detwinning characteristic can be identified from Fig. 2.9 during compression-tension, but the information is restricted on the sample surface level, due to the limitation of the EBSD technique. Although a limit number of research employed in-situ neutron and synchrotron X-ray diffraction to investigate the LCF behavior of wrought Mg alloys [43-45], as indicated in Fig. 2.10, the fatigue mechanism is not fully understood.

2.4 Fatigue Crack Growth Behavior in Mg Alloy

The life of a fatigue crack has two parts, initiation and propagation. It is well known than the fatigue endurance limit does not exist in non-ferrous alloys. It has been demonstrated that, in wrought Mg alloys, the fatigue crack initiated at early stage of fatigue life, only 5 – 10% of total fatigue life [136], in Fig. 2.11. The total fatigue life can be approximated as the fatigue crack propagation life. Therefore, the study of fatigue crack growth behavior of wrought Mg alloys becomes essential. As an advantage of the

fatigue studies of Mg alloys, the anisotropic effects on the twinning and detwinning behavior can be quantified at both macroscopic and microscopic levels. The wrought Mg material consists of the typical rolling texture. Thus, the development of the plastic fields surrounding the fatigue-crack tip is very sensitive to the crack-growth and loading directions – this is the macroscopic anisotropic behavior. The stress levels in the plastic wake, the extent of the compressive residual-stress zone, and the stress multiaxiality are particularly important in quantifying the microscopic twinning and detwinning behavior. Such a microscopic view will ensure a proper understanding of the fatigue-crack resistance.

The *primary* challenge in the fatigue study is the lack of an *in situ*, nondestructive investigation on the microstructural length scale, which prevents us from linking the stress analyses (from a top-down point of view) and the failure mechanisms at inter- and intra-granular scales (from a bottom-up point of view). Fracture and fatigue cracks have multiscale characteristics [137-140], as shown in Fig. 2.12. At a macroscopic length scale, the deformation field includes a plastic zone in front of the crack tip and a plastic wake left behind, where the compressive stress/strain are developed due to cyclic loading. The magnitude, distribution, and history of the residual strain along the crack path depend on the stress multiaxiality, material properties, and history of the applied stress intensity factor and the resulting crack growth rate. At microscopic length scales, a number of grain aggregates around the crack tip deform to accommodate the multiaxial stress fields exerted from the surrounding plastic field. For a fatigue crack in Fig. 2.12, along the crack path for points A to F, the multiaxial stress states are quite different. The

stress multiaxiality is increasingly complicated from a biaxial tensile stress state in a linear elastic region, as shown at point A, to a triaxial stress state in the plastic zone region (points B and C), and to a biaxial compressive stress state in the plastic wake region (points D, E, and F). Due to a limited number of slip and twinning systems available at room temperature, deformation and failure characteristics of Mg alloys under multiaxial stress states are radically different from those of uniaxial tests. Fatigue process zones in Mg alloys are thus very distinct from typical engineering alloys.

It has been acknowledged that the fatigue crack propagation behavior is time-dependent, and the strain rate, load ratio, oxidation process, crack closure, and microstructure are the key factors for the fatigue crack propagation rate [136, 141-147]. It has been reported [148] that the fatigue crack propagation rate of wrought Mg alloys increased with reducing frequency (or strain rate) and an increase in load ratio, as shown in Fig. 2.13, which may be attributed to the thickness of oxide films on the fracture surfaces or the crack closure effect. The fatigue crack deviation and branching have been observed in previous research, which lead to a decrease of the effective stress intensity at the crack front and an increase of the energy required propagating the crack [141]. However, the in-situ studies of fatigue crack growth behavior of wrought Mg alloys are very limited. The relationship between macroscopic fatigue crack propagation behavior and microscopic response in grain level remain unclear. Regarding to the complexity of plastic deformation (dislocation, twinning, and detwinning) around fatigue crack tip of HCP structured wrought Mg alloys, the investigation of surrounding plasticity is especially critical for improving our understanding on fatigue crack growth behavior.

2.5 Theoretical Modeling

The evolution of the lattice strains during loading in different groups of grains can be used as a very sensitive indicator for plastic deformation mechanisms at microscopic levels [149]. Therefore, combining with macroscopic stress–strain curves and texture evolutions, plastic deformation mechanisms can be studied by analyzing elastic lattice strain data acquired from in-situ neutron and/or synchrotron X-ray diffraction measurements. Self-consistent polycrystal models have been widely applied to interpret experimentally measured lattice strain data, in which the precise surroundings of each grain are not accounted for. This apparent limitation, however, is not so significant in interpreting bulk averaged neutron and/or synchrotron X-ray diffraction data. The visco-plastic self-consistent (VPSC), developed by Molinari et al. [150] and Lebensohn and Tomé [151], was a very popular self-consistent polycrystal model that had been successfully applied to simulate large strain behavior and texture evolution of hexagonal close-packed (HCP) polycrystalline Mg under various deformation modes [51, 54, 60, 152]. Unfortunately, VPSC model does not include elastic deformation and thus is not applicable for the simulation of lattice strains evolution. Thus, most of in-situ neutron and/or synchrotron X-ray diffraction data have been interpreted by using the elastic-plastic self-consistent (EPSC) model developed by Turner and Tomé[153]. However, the EPSC model works only for small deformation and does not include texture evolution associated with slip or twinning reorientation. Very recently, the large strain elasto-viscoplastic self-consistent (EVPSC) model, recently developed by Wang et al. [154-

156], has been successfully applied for prediction of large strain behavior during uniaxial tension-compression in HCP structured Mg alloys.

The EVPSC model for polycrystals is a completely-general elastic-visco-plastic, fully anisotropic, self-consistent polycrystal model, applicable to large strains and to any crystal symmetry [157]. The TDT model keeps track of all active twin variants in each grain and takes into account of all possible twinning and detwinning operations. The TDT model is implemented into the finite-strain EVPSC model for polycrystals in the current study. Moreover, the affine self-consistent scheme is employed, which gives the best overall performance. A detailed description for EVPSC and TDT models can be found elsewhere [154, 157-160].

A brief description of the TDT model is provided here. There are four potential operations related to the twinning and detwinning in a grain, as demonstrated in Fig. 2.14, including (1) Operation A: the twin nucleation [a twin grain (child grain) initiates in the matrix (parent grain)], (2) Operation B: the twin propagation (twin-boundary movement: the twinning dislocations glide toward the side of parent grain), (3) Operation C: detwinning (twin boundary movement: the twinning dislocations glide to the side of a child grain), and (4) Operation D: detwinning (the initiation of twin inside child grains).

The shear rates of Operations A and C for a twinning system, α, is defined in parent grains, and presented as follow:

$$\dot{\gamma}^{\alpha A} = \begin{cases} \dot{\gamma}_0 \left| \tau^{\alpha} / \tau_{cr}^{\alpha} \right|^{1/m} & \tau^{\alpha} = \tau^{\alpha P} > 0 \\ 0 & \tau^{\alpha} = \tau^{\alpha P} \le 0 \end{cases}$$

$$\dot{\gamma}^{\alpha C} = \begin{cases} -\dot{\gamma}_0 \left| \tau^\alpha / \tau_{cr}^\alpha \right|^{1/m} & \tau^\alpha = \tau^{\alpha P} < 0 \\ 0 & \tau^\alpha = \tau^{\alpha P} \geq 0 \end{cases} \tag{5}$$

where $\dot{\gamma}^{\alpha A}$ and $\dot{\gamma}^{\alpha C}$ are the shear rate for Operations A and C, respectively, $\dot{\gamma}_0$ is the reference shear rate, $\tau^\alpha = \sigma : P^\alpha$ (σ is the Cauchy stress tensor and P^α is the Schmid tensor), τ_{cr}^α is the critical resolved shear stress (CRSS), and m is the strain rate sensitivity.

The evolution of the twin-volume fraction subjected to Operations A and C can be represented as:

$$\dot{f}^{\alpha A} = \frac{\left| \dot{\gamma}^{\alpha A} \right|}{\gamma^{tw}}, \qquad \dot{f}^{\alpha C} = \frac{\left| \dot{\gamma}^{\alpha C} \right|}{\gamma^{tw}} \tag{6}$$

where $\dot{f}^{\alpha A}$ and $\dot{f}^{\alpha C}$ are the twin volume fraction for A and C, respectively, γ^{tw} is the characteristic twinning shear strain.

The shear rates for the twinning system, α, inside a child grain are from Operations B and D:

$$\dot{\gamma}^{\alpha B} = \begin{cases} -\dot{\gamma}_0 \left| \tau^\alpha / \tau_{cr}^\alpha \right|^{1/m} & \tau^\alpha = \tau^{\alpha B} < 0 \\ 0 & \tau^\alpha = \tau^{\alpha B} \geq 0 \end{cases}$$

$$\dot{\gamma}^{\alpha D} = \begin{cases} \dot{\gamma}_0 \left| \tau^\alpha / \tau_{cr}^\alpha \right|^{1/m} & \tau^\alpha = \tau^{\alpha D} > 0 \\ 0 & \tau^\alpha = \tau^{\alpha D} \leq 0 \end{cases} \tag{7}$$

where $\dot{\gamma}^{\alpha B}$ and $\dot{\gamma}^{\alpha D}$ are the shear rate for Operations A and C, respectively

The evolution of the twin volume fraction associated with Operations B and D are listed as follows:

$$\dot{f}^{\alpha B} = \frac{\left| \dot{\gamma}^{\alpha B} \right|}{\gamma^{tw}}, \qquad \dot{f}^{\alpha D} = \frac{\left| \dot{\gamma}^{\alpha D} \right|}{\gamma^{tw}} \tag{8}$$

where $\dot{f}^{\alpha B}$ and $\dot{f}^{\alpha D}$ are the twin volume fraction for B and D, respectively.

The evolution of the twin volume fraction due to twinning in a system, α, is governed by:

$$\dot{f}^{\alpha} = f^{0}(\dot{f}^{\alpha A} + \dot{f}^{\alpha C}) + f^{\alpha}(\dot{f}^{\alpha B} + \dot{f}^{\alpha D}) \tag{9}$$

where $\dot{f}^{\alpha}$ is the twin volume fraction and f^{0} is the volume fraction of the parent ($f^{0} = 1 - f^{tw} = 1 - \sum_{\alpha} f^{\alpha}$).

The threshold volume fraction, V^{th}, is defined as:

$$V^{th} = \min\left(1.0, A_1 + A_2 \frac{V^{eff}}{V^{acc}}\right) \tag{10}$$

where A_1 and A_2 are material constants, V^{eff} is the effective twinned fraction related to the volume fraction of twin-terminated grains, and V^{acc} is the accumulated twin fraction associated with the weighted volume fraction of the twinned region.

For slip and twinning, the evolution for the CRSS $\dot{\tau}_{cr}^{\alpha}$ is provided by:

$$\dot{\tau}_{cr}^{\alpha} = \frac{d\hat{\tau}^{\alpha}}{d\Gamma} \sum_{\beta} h^{\alpha\beta} \left|\dot{\gamma}^{\beta}\right| \tag{11}$$

where Γ is the accumulated shear strain ($\Gamma = \sum_{\alpha} \int \left|\dot{\gamma}^{\alpha}\right| dt$), $h^{\alpha\beta}$ are the latent hardening coupling coefficients, and $\hat{\tau}^{\alpha}$ is the threshold stress and is characterized by:

$$\hat{\tau}^{\alpha} = \tau_0^{\alpha} + (\tau_1^{\alpha} + h_1^{\alpha}\Gamma)(1 - \exp(-\frac{h_0^{\alpha}}{\tau_1^{\alpha}}\Gamma)) \tag{12}$$

where τ_0^α is the initial CRSS, h_0^α is the initial hardening rage, h_1^α is the asymptotic hardening rate, and $\tau_0^\alpha + \tau_1^\alpha$ is the back-extrapolated CRSS.

CHAPTER 3
MATERIALS AND METHODS

3.1 Experimental Materials

A commercial polycrystalline wrought AZ31B Mg alloy (3 *wt.*% Al, 1 *wt.*% Zn, and Mg balance) after rolling is chosen as the experimental material, because it is a highly textured alloy. The thickness of the rolling plate is 76 mm, as illustrated in Fig. 3.1. A typical rolling texture can be observed, with (00.2) grains preferably aligned in rolling plate normal direction (ND) and perpendicular to rolling direction (RD) and transverse direction (TD). After sample machining, the specimens were annealed at 345 ^{o}C for 2 hours to remove the existing residual stress due to manufacturing and machining. The average grain size of the annealed wrought AZ31B magnesium alloy is approximate 40 μm. The pole figures of the anneal sample have presented in Fig. 3.2, which is performed at The Canadian Institute for Neutron Scattering (CINS), Chalk River, Ontario, Canada. The neutron diffraction pattern for a powder sample was measured at VULCAN, SNS, ORNL.

The dog-bone cylindrical specimens with 8-mm diameter and 16-mm gage length were machined for tension/compression and low-cycle fatigue, according to the American Society for Testing and Materials (ASTM) Standard E606-04, with the loading direction along either in ND or RD. A plate dog-bone specimen was prepared with its axial direction along the rolling direction (RD) and surface-normal direction parallel to the normal direction (ND) of the rolling plate for the synchrotron X-ray microbeam

diffraction measurements. The sample gauge section was 2 mm length x 1.5 mm width x 1.5 mm thickness.

The Disk-shaped Compact Tension [DC(T)] specimens were prepared from the thick plate, according to the American Society for Testing and Materials (ASTM) Standard E647-13e1 [161]. The specimens were cut in the plane of the rolling direction (RD) and normal direction (ND). Thus, the fatigue-loading direction and crack-propagation direction were parallel to the plate ND and RD, respectively.

3.2 Mechanical Testing

The tension and compression were performed under a constant strain rate, 1.3 x 10^{-5} s^{-1}, using Material Testing System (MTS) 810 electrohydraulic machine and VULCAN loadframe at room temperature in lab air. A clip-on MTS extensometer with a gauge length of 6 mm was used to monitor or control the axial strain.

The fully-reversed strain-controlled low-cycle fatigue experiment was conduct with at different total strain amplitude at room temperature using VULCAN loadframe. Triangular loading waveform was applied during the tests. The frequency in the other fatigue cycles was 1 Hz.

A customized loadframe was specially designed for the in-situ synchrotron X-ray microbeam diffraction measurements. Three strain levels were chosen based on our previous experience, e.g., undeform state, - 2.4 % compressive strain (in the twinning dominant deformation region), and - 5.8 % strain during the reverse tension (in the

detwinning dominant deformation region). The mechanical testing was under strain control using digital image correlation method.

Fatigue-crack-propagation experiments were carried out using an MTS 810 electrohydraulic machine at room temperature in laboratory air under a constant ΔP [$\Delta P = P_{max} - P_{min,}$ where P_{max} and P_{min} are the applied maximum (2,300 N) and minimum (230 N) loads, respectively] control mode. The test frequency was 10 Hz, and the R ratio (P_{min}/P_{max}) was 0.1. The stress-intensity factor, K, was determined by the equation below [30]:

$$K = \frac{P}{B\sqrt{W}} \cdot \frac{(2+\alpha)(0.76+4.8\alpha-11.58\alpha^2+11.43\alpha^3-0.48\alpha^4)}{(1-\alpha)^{3/2}} \qquad (13)$$

where P = applied load, B = thickness, W = width, $\alpha = a/W$, and a = crack length.

During fatigue-crack-propagation tests, the crack length of CT specimens was determined by an unloading-compliance method [31-33]. A crack-opening-displacement (COD) gauge was mounted on the front face of each CT specimen to measure CODs, which, in turn, were converted into crack lengths by the compliance technique. When the crack length reached 15 mm, the crack-growth experiments were stopped, and then the fatigue-cracked CT sample was taken for in-situ neutron strain-mapping experiments.

3.3 Diffraction Techniques

3.3.1 Neutron diffraction

The advantage of employing neutron diffraction in research has been presented below: (1) Neutrons are neutral particles and they are highly penetrating that will provide the bulk information, which can be used as nondestructive probes and to study samples in severe environments. (2) The wavelengths of neutrons are similar to atomic spacing.

They can determine the crystal structures and atomic spacing and other structural information. (3) Neutrons can “see” nuclei. They are sensitive to light atoms. They can exploit isotopic substitution and use contrast variation to differentiate complex molecular structures. (4) The energies of thermal neutrons are similar to energies of elementary excitations in solids. Hence, they can be used to study lattice and molecular dynamics. (5) Neutrons have a magnetic moment. They can be applied to study microscopic magnetic structure and magnetic fluctuations. (6) Neutrons have spin. They can be formed into polarized neutron beams and used to investigate complex magnetic structures and dynamics.

Neutron diffraction has been successfully employed as a method of choice for investigating the twinning behavior and internal-strain evolution in magnesium alloys [43-45, 47, 57, 80, 81, 87]. The state-of-art VULCAN engineering diffractometer of SNS at ORNL in US, the time-of-flight (TOF) neutron diffractometer, ENGIN-X, at the ISIS facility in UK, the E3 spectrometer for bulk texture measurements at the Canadian Neutron Beam Centre, Canada, provide us great opportunities to investigate the internal-strain and texture evolution of magnesium alloys. In-situ neutron-diffraction results offer insights on studying the deformation mechanisms of these alloys at the grain level, which will account for the observed macroscopic mechanical behavior. In this proposal, the internal-strain and texture evolution of wrought magnesium alloys will be examined under static/dynamic and uniaxial/multi-axial loading conditions to provide a basic understanding of plastic deformation mechanism.

The real-time in-situ neutron diffraction measurements were performed under continuous-loading conditions using the state-of-the-art VULCAN Engineering

diffractometer at the Spallation Neutron Source (SNS), Oak Ridge National Laboratory (ORNL) [38, 162, 163]. The schematic setup of the real-time in-situ neutron diffraction measurements was presented in Fig. 3.3. Briefly, the specimen was mounted in the VULCAN loadframe horizontally and carefully aligned, so that the axial and horizontal-radial directions parallel to the RD and ND, respectively. The angle between the incident neutron beam and the sample was 45^{o}. The two stationary detector banks, which located $\pm 90^{o}$ to the incoming beam, recorded simultaneously two complete diffraction patterns in the axial (RD of the rolling plate) and horizontal-radial (ND of the rolling plate) directions with diffraction vectors parallel ($Q_{\parallel}$) and perpendicular ($Q_{\perp}$) to the applied load, respectively. The neutron beam size was defined as 5 mm (horizontal) x 5 mm (vertical), and the 5-mm receiving collimators were selected, leading to a neutron gauge volume of total 125 mm^3. It is worthy to mention that approximately 1.9 million grains (the grain size is 40 μm and the neutron gauge volume is 125 mm^3) were measured during the deformation, which suggests an excellent counting statistics for the neutron diffraction experiments.

The real-time in-situ neutron diffraction measurements were performed under a continuous loading condition, which essentially eliminates the strain flow or the stress relaxation under the stress or strain control [38, 164]. Neutron diffraction data were recorded successively during loading, and the data were chopped into small time bins afterwards using the event-based data reduction software VULCAN Data Reduction and Interactive Visualization softwarE (VDRIVE) [165]. Short time interval was determined based on both the statistics and the quality of different patterns for data fitting, in order to obtain an adequate representative of the actual data. Neutron diffraction data were sliced

every two minutes in the current study and synchronized with loadframe information, such as averaged load/stress and displacement/strain over two minutes. It is worth mentioning that because a small strain interval (1.3×10^{-5} s^{-1} x 120 s = 1.56×10^{-3}) was chosen in the current study, the average stress changes over every two minutes are considered to be acceptable. The stress interval from point to point varies from 2 MPa to 8 MPa in the plastic-deformation regions. The neutron diffraction peak intensities of different *hkl*s after the background subtraction were normalized to the incoming beam energy. The lattice strain of different *hkl*s was calculated based on the equation below:

$$\varepsilon^{hkl} = \frac{d^{hkl} - d_0^{hkl}}{d_0^{hkl}} \tag{14}$$

where ε^{hkl} is the lattice strain, d_0^{hkl} and d^{hkl} are the d-spacings before and after deformation, respectively. The counting time for the measurement of the reference in both samples was 10 minutes, which is longer than the chopped data, in order to minimize the propagated d_0^{hkl} statistic error.

In-situ neutron-diffraction measurements were performed using the time-of-flight (TOF) neutron diffractometer, ENGIN-X, at the ISIS facility, Rutherford Appleton Laboratory, UK. The experimental details were shown elsewhere [166], and only brief experimental descriptions are provided here. Figure 3.4 shows the experimental setup and diffraction geometry. The CT specimens were carefully aligned at the Instron load frame. The loading axis is oriented 45^o relative to the incident beam. The two stationary detector banks were situated at $\pm 90^o$ by simultaneously recording two complete diffraction patterns with diffraction vectors parallel ($Q_{\parallel}$) and perpendicular ($Q_{\perp}$) to the applied load.

Note that banks 1 and 2 collect *hkl*s in the normal direction [ND, Fig. 3.4(b)] and transverse direction [TD, Fig. 3.4(a)], respectively. The slit was defined by 1 (vertically) x 3 (horizontally) mm, and a 3-mm radial collimator, resulting in a gauge volume of 9 mm^3. This arrangement provides 1-mm spatial resolution in the direction of crack propagation. Figure 3.4c shows the diffraction patterns measured in both banks at the location away from the crack tip (which is a stress-free reference position). The initial texture revealed a typical strong rolling texture in which most of the grains have a basal pole parallel to the plate normal (ND).

In-situ neutron-diffraction measurements were performed by mapping the lattice-strain evolution and monitoring the intensity changes of certain *hkl*s at various locations relative to the crack-tip position during the loading-unloading cycles, including 5 different loading sequences, marked with a blue circle, Fig. 3.4(d). Moreover, more detailed loading levels [marked with a triangle, Fig. 3.3(d)] were employed at 0.5 mm in front of the crack-tip, where the high stress concentration is imposed, during the loading-unloading sequences. All lattice parameters were calculated, using a Rietveld Analysis [35] in which multiple peaks are fitted over a user-defined range. The analysis was performed, employing the General Structure Analysis System (GSAS) software in conjunction with the ISIS in-house software OPEN GENIE.

The neutron-diffraction patterns were analyzed, using single-peak fitting for certain *hkl*s interested in order to examine the lattice-strain and intensity variations as a function of the applied load. The lattice strains (Equation 2) and lattice-strain errors (Equation 3) were calculated, using equations below, respectively:

$$\varepsilon = \frac{d - d_0}{d_0} \tag{14}$$

$$\partial\varepsilon = \frac{\partial d}{d_0} - \frac{d\partial d_0}{d_0^2} = (\frac{d - d_0}{d_0})(\frac{d_0\partial d - d\partial d_0}{d_0(d - d_0)}) = \varepsilon(\frac{\partial d}{d - d_0} - \frac{d\partial d_0}{d_0(d - d_0)}) \tag{15}$$

where ε is the lattice strain, d is the lattice spacing under the loaded condition and d_0 is nominally stress-free reference lattice spacing measured far away from the crack in the annealed CT specimen, $\partial\varepsilon$ is the lattice-strain error, ∂d and ∂d_0 are the lattice-spacing errors in the loaded condition and stress-free reference location, respectively.

Neutron bulk texture measurements were carried out, using the E3 spectrometer at the Canadian Neutron Beam Centre, Canada. Three different locations from the crack tip, representing the different fatigue history, were chosen to examine the evolution of the bulk texture during fatigue-crack propagation. A piece with the volume of 2.2 mm (RD) x 3.6 mm (ND) x 6.35 mm (TD) was cut from the following locations covering (i) –2.7 to –0.5 mm along RD behind the crack tip where the material was already subjected to the severe plastic deformation followed by fracture, (ii) 0.5 to 2.7 mm along RD right in front of the crack tip where the material was deformed plastically, and (iii) 3 to 5.2 mm along RD far away from the crack tip where the material was deformed elastically. The wavelength of 2.2Å was selected from the Ge113 monochromator. The samples were exposed to the neutron beam with a cross section of 49 x 24.5 mm. Three pole figures, {10.0}, {00.2}, and {10.1}, were measured to obtain the orientation distribution function (ODF) for each sample. The volume fraction of {00.2} extension twins was estimated from the {00.2} pole-figure data reconstructed by the ODF (see discussion for details).

3.3.2 Synchrotron X-ray microbeam diffraction

The in-situ 3D-XRD at sub-micro level was performed at 34ID-E, Advanced Photon Source (APS), Argonne National Laboratory (ANL), USA. The 3D-XRD uses synchrotron X-ray microbeams to probe local crystal structure, orientation and strain tensors with submicrometer spatial resolution. The schematic of in-situ 3D-XRD is illustrated in Fig. 3.5(a). The sample was 45^{o} to the incoming beam and GE detector. The loading direction was marked in the coordinate X direction. The movement of platinum wire profiler was perpendicular to the sample surface normal direction. For the grain orientation mapping, the white beam (the energy range from 7 – 30 keV) was applied with0.5 x 0.5 μm beam size. The step sizes were 2 μm along loading direction (X-axis) and sample depth direction (Y-axis), respectively. The monobeam (fixed beam energy for a specific *hkl*) was employed for the energy scan at certain locations (the fixed locations at X-axis) with 0.5 x 0.5 μm beam size. The step size along the sample depth direction (Y-axis) was 1 μm.

3.4 The EVPSC constitutive model

In this section, we briefly recapitulate the EVPSC-TDT model, mainly for the purpose of definition and notation. For details we refer to Wang et al. [119, 167]. The EVPSC model developed by Wang et al. [167] for polycrystalline materials is a completely general elastic visco-plastic, fully anisotropic, self-consistent polycrystal model, applicable to large strains and to any crystal symmetry. It has been demonstrated that the EVPSC model can be used to simulate large strain behavior of HCP polycrystalline materials under various deformation processes [160, 168-170]. Very

recently, a new constitutive model to describe Twinning and De-Twinning (TDT) for polycrystalline materials with the HCP crystallographic structure has been developed (Wang et al. [119, 157]) and implemented in the EVPSC polycrystal plasticity mode. The TDT model has been applied to Mg alloy AZ31B sheet under cyclic loadings and strain path changes (see e.g. Wang et al. [119, 157, 171]). It has been demonstrated that the new twinning model is able to capture key features associated with experimentally observed twinning and detwinning.

The plastic deformation of a crystal is assumed to be resulted from crystallographic slip and twinning on crystallographic system $(\mathrm{s}^{\alpha}, \mathrm{n}^{\alpha})$. Here, s^{α} and n^{α} are respectively the slip/twinning direction and the normal of the slip/twinning plane for system α. In the present study, we assume the plastic deformation is due to three types of slip systems: Basal <*a*> $(\{0001\}<11\bar{2}0>)$, Prismatic <*a*> $(\{10\bar{1}0\}<11\bar{2}0>)$ and Pyramidal <*c*+*a*> $(\{\bar{1}\,\bar{1}22\}<\bar{1}\,\bar{1}23>)$, and one twinning mode: the $\{10\bar{1}2\}<\bar{1}011>$ tensile twin system. The plastic strain rate tensor for the crystal can be written as

$$\mathrm{d}^{p} = \sum_{\alpha} \dot{\gamma}^{\alpha} \mathrm{P}^{\alpha} \tag{16}$$

in terms of the shear rate, $\dot{\gamma}^{\alpha}$, and the Schmid tensor, $P^{\alpha} = (s^{\alpha} n^{\alpha} + n^{\alpha} s^{\alpha})/2$ for system α. Regardless of slip or twinning, the driving force for shear rate, $\dot{\gamma}^{\alpha}$, is the resolved shear stress, $\tau^{\alpha} = \sigma : \mathrm{P}^{\alpha}$, where σ is the Cauchy stress tensor. For slip,

$$\dot{\gamma}^{\alpha} = \dot{\gamma}_0 \left| \tau^{\alpha} / \tau_{cr}^{\alpha} \right|^{\frac{1}{m}} \mathrm{sgn}(\tau^{\alpha}) \tag{17}$$

and for twinning,

$$\dot{\gamma}^{\alpha} = \begin{cases} \dot{\gamma}_0 \left| \tau^{\alpha} / \tau_{cr}^{\alpha} \right|^{\frac{1}{m}} & \tau^{\alpha} > 0 \\ 0 & \tau^{\alpha} \le 0 \end{cases} \tag{18}$$

where $\dot{\gamma}_0$ is a reference shear rate, τ_{cr}^{α} is the critical resolved shear stress (CRSS), and *m* is the strain rate sensitivity.

For both slip and twinning, the evolution of CRSS, τ_{cr}^{α}, is given by:

$$\dot{\tau}_{cr}^{\alpha} = \frac{d\hat{\tau}^{\alpha}}{d\Gamma} \sum_{\chi} h^{\alpha\chi} \left| \dot{\gamma}^{\chi} \right| \tag{19}$$

where $\Gamma = \sum_{\beta} \int \left| \dot{\gamma}^{\alpha} \right| dt$ is the accumulated shear strain in the grain, and $h^{\alpha\chi}$ are the latent hardening coupling coefficients, which empirically account for the obstacles on system α associated with system χ. $\hat{\tau}^{\alpha}$ is the threshold stress and is characterized by:

$$\hat{\tau}^{\alpha} = \tau_0^{\alpha} + (\tau_1^{\alpha} + h_1^{\alpha}\Gamma)(1 - \exp(-\frac{h_0^{\alpha}}{\tau_1^{\alpha}}\Gamma)) \tag{20}$$

Here, τ_0, h_0, h_1, and $\tau_0 + \tau_1$ are the initial CRSS, the initial hardening rate, the asymptotic hardening rate, and the back-extrapolated CRSS, respectively.

Because it is rare that a grain can be fully twinned, a threshold twin volume fraction is defined in the model to terminate twinning. Consequently, the TDT model introduces two statistical variables: accumulated twin fraction, V^{acc}, and effective twinned fraction, V^{eff}. More specifically, V^{acc} and V^{eff} are the weighted volume fraction of the twinned region and volume fraction of twin terminated grains, respectively. The threshold volume fraction, V^{th}, is defined as $V^{th} = \min\left(1.0,\ A_1 + A_2 \frac{V^{eff}}{V^{acc}}\right)$, where A_1 and A_2 are two material constants.

CHAPTER 4
RESULTS AND DISCUSSION

4.1 Deformation Dynamics during Uniaxial Loading using Real-Time In-Situ Neutron Diffraction and EVPSC-TDT Model

4.1.1Macroscopic mechanical behavior

Figure 4.1 demonstrates the mechanical-testing results during the aforementioned strain-control profile for both the as-received and pre-deformed samples [164]. The orange arrows and circled numbers marked in Fig. 4.1 identify the loading paths. The open symbols represent the experimental results, and the dashed lines stand for the simulation results.

As shown in Fig. 4.1(a), the as-received sample was compressed to – 7% strains, then unloaded to 0 N, followed by the reverse tension until sample failure. During compression, relative low compressive yield strength was observed, followed by a gradual increase of stresses until approximately – 103 MPa (marked as a red dot). Subsequently, the slope of the stress-strain curve started to increase, which suggests strain hardening. When the sample was unloaded to 0 N, the material exhibited pseudoelastic behavior, which, in general, is defined as nonlinearity during unloading. During the reverse tension, relative low yield strength was observed, followed by slight strain hardening until the stress reached to 118 MPa (marked as a green dot). From approximately 118 MPa to 217 MPa (marked as a blue dot), the stress increased steeply with increasing strain. When the sample was further stretched, the stress-strain curve tended to flat.

The pre-deformed sample [in Fig. 4.1(b)] had a similar trend as the as-received sample [in Fig. 4.1(a)]. However, an obvious increase in the compressive yield strength, approximately 40 MPa, could be observed. Moreover, the pre-deformed sample exhibited apparent strengthening during the compression, resulting from the prior in-plane tension. In the following reverse tension, the effect of pre-tension became less significant, and only a small increase of the tensile yield strength, about 13 MPa, could be identified.

In the simulations shown in Fig. 4.1, the room-temperature elastic constants of the Mg single crystal are $C_{11} = 58.0$, $C_{12} = 25.0$, $C_{13} = 20.8$, $C_{33} = 61.2$ and $C_{44} = 16.6$ (GPa). The reference slip/twinning rate, $\dot{\gamma}_0$, and the rate sensitivity, *m*, are prescribed to be the same for all slip/twinning systems: $\dot{\gamma}_0 = 0.001\,s^{-1}$ and $m = 0.05$, respectively. Values of the hardening parameters were estimated by fitting numerical simulations of monotonic uniaxial tension and compression along the RD to the corresponding experimental flow curves. Therefore, the calculated stress and strain curves shown in Fig. 3 are predictions. It is clear that the EVPSC-TDT model can well reproduce the experimental curves. The values of these parameters are listed in Table 1 and will be used in all the simulations reported in the present paper.

The strain-hardening-rate evolution during the strain-path changes were examined for both the as-received and pre-deformed sample as presented in Fig. 4.2. The hardening rate can be calculated based on the well-known equation below:

$$\theta = \frac{d\sigma}{d\varepsilon} \tag{21}$$

where θ is the work-hardening rate, σ is the stress, and ε is the strain.

For the as-received sample during the compression [a top figure in Fig. 4.2(a)], a steady work-hardening rate can be obtained between the yield strength and – 103 MPa. When the sample was compressed further, the work-hardening rate increased rapidly. When the applied stress reached to – 168 MPa, the work-hardening rate began to decline. During the reverse tension [a bottom figure in Fig. 4.2(a)], a stable work-hardening rate can be perceived, until the applied stress reached to 118 MPa. Then, an abrupt increase of the work-hardening rate was found in the stress range from 118 MPa to 217 MPa. When the sample was further stretched, the work-hardening rate dropped promptly. Thus, the curve was divided into two regions in the compression (designated as stress ranges I and II) and three sections in the reverse tension (designated as stress ranges III, IV, and V) for the as-received sample based on the work-hardening-rate variation. Although three regions were recognized in the compression, in the present study the third region was overlooked on purpose since only one data point after – 168 MPa. For the pre-deformed sample, the work-hardening rate decreased constantly during the tension [a top figure in Fig. 4(b)]. The work-hardening rate vs. stress curve can also be separated into two stages in compression [a middle figure in Fig. 4.2(b), designated as stress ranges i and ii] and three regions in the reverse tension [a bottom figure in Fig. 4.2(b), designated as stress ranges iii, iv, and v], respectively.

4.1.2 Microscopic response at a grain level

Diffraction peak intensity evolution: Figure 4.3 presents diffraction peak intensity evolution in different *hkl*s in the axial direction from the real-time in-situ neutron diffraction measurements and simulations for both the as-received and pre-deformed

samples. The separation of stress ranges in Fig. 4.3 was inherited from Fig. 4.2, based on the work-hardening-rate variation. Thus, the microscopic response can be isolated in each macroscopic stress range to examine.

For the as-received sample in Fig. 4.3(a), little variations on diffraction peak intensities for (10.0) and (11.0) grains can be observed in the elastic region during compression. The (00.2) diffraction peak intensity was absent until the stress exceeded the yield strength. In the stress range I, the diffraction peak intensities of (10.0) and (11.0) grains decreased dramatically, while the (00.2) diffraction peak intensity grew rapidly due to tensile twinning. When the compressive stress went into the stress range II, both the decrease of (10.0) peak intensity and the increase of (00.2) peak intensity decelerated simultaneously. During the unloading, no apparent diffraction peak intensity variation can be observed in (10.0), (00.2), and (11.0) grains, suggesting that no detwinning occurred. No evident detwinning process can be identified even in the elastic region (below 87 MPa) during the reverse tension, since the diffraction peak intensities of (10.0), (00.2), and (11.0) grains remained almost unchanged. In the stress range III, the diffraction peak intensities of (10.0) and (11.0) grains increased abruptly, simultaneously, the diffraction peak intensity of (00.2) twin grains diminished significantly suggesting that the detwinning occur intensively. In the stress range IV, the diffraction peak intensity of (00.2) twin grains decreased gradually, and the diffraction peak intensities of (10.0) and (11.0) detwinned grains increased slowly. Nearly all of the (10.0) and (11.0) diffraction peak intensities recovered and the (00.2) twin grains disappeared, when the stress reached 217 MPa. The diffraction peak intensity of interested *hkl*s stayed unchanged when the sample was further pulled to the stress range V.

The diffraction peak intensity evolution of the pre-deformed sample demonstrated the analogous tendency to the as-received sample during the compression and reverse tension, as shown in Fig. 4.3(b). It is interesting that the stress rang from the activation to the exhaustion of the tensile twinning (stress range i) in the pre-deformed was narrower than the as-received sample (stress range I). Moreover, the duration of the detwinning process was shorter in the pre-deformed sample (stress range iii) than in the as-received sample (stress range III).

To the best of the authors' knowledge, it is the very first time that the EVPSC-TDT model was employed to simulate the twinning and detwinning behavior under a continuous-loading condition during strain-path changes in a HCP-structured Mg alloy. It is illustrated that the simulation results are in a good agreement with the neutron diffraction results. The simulation results also exhibited that no obvious diffraction peak intensity variation in (10.0), (00.2), and (11.0) grains during unloading, indicating that no detwinning occurred, which is contrary to previous studies [43, 45, 62, 81]. The details will be provided in the discussion.

The lattice-strain evolution: Figure 4.4(a) describes the relationships between the internal strain evolution and stress in the axial direction during compression for the as-received sample. In the stress range I, the lattice strain of (11.0) grains increased more rapidly than (10.0) and (10.1) grains. At the emergence of the (00.2) twins, the lattice strain of (00.2) grains increased at a similar rate as those in (10.0) and (10.1) grains, but slower than that in (11.0) grains. In the stress range II, the lattice strain of (11.0) and (10.1) grains increased slowly until saturated. Whereas, the internal strain was rapidly transferred to (00.2) twin grains, which, in the meantime, became the majority of the

population among all orientation grains in the axial direction due to the tensile twinning, as presented in Fig. 4.4(a). The final lattice strain in (00.2) twin grains reached 4,628 με, which was higher than in other orientation grains. In the radial direction, the lattice strain of (00.2) grains saturated immediately at the compressive yield strength, – 63 MPa, as presented in Fig. 4.4(c).

The lattice-strain evolution of the pre-deformed sample in Fig. 4.4(b) in the axial direction during compression resembled the as-received sample in general. However, some differences can be distinguished. First, the yield strength in the pre-deformed sample is much higher than the as-received sample. It should be noted that (10.0) and (11.0) grains contained a small amount of residual tensile strains at 0 MPa, while (10.1) grains had nearly zero residual strain in the pre-deformed sample. Second, at the same stress level, the lattice strain of (00.2) twin grains in the pre-deformed sample was much less than in the as-received sample. For example, at a stress level, 150 MPa, the lattice strain of (00.2) grains in the pre-deformed sample, 2,195 με, was much lower than the as-received sample, 4,256 με. Third, the lattice strain of (11.0) grains in the pre-deformed sample was the highest compared with (10.0), (11.0), and (10.1) grains by the end of compression deformation, while the lattice strain of (00.2) grains was the highest in the as-received sample. In Fig. 4.4(d), the (00.2) grains in the radial direction for the pre-deformed sample also yielded right after the stress reached the yield strength, as the as-received sample. However, a compressive residual strain in (00.2) grains was observed at 0 MPa, which was caused by the pre-deformation.

When the sample was unloaded to 0 MPa after compression, the (10.1) grains exhibited a small amount of tensile residual strains in the as-received sample in the axial

direction, while, surprisingly, the compressive residual strains can be seen in (11.0) grains and (00.2) twin grains, as shown in Fig. 4.4(e). It should be emphasized that (00.2) twin grains contain a relatively large compressive residual strain, about 1,067 με. In Fig. 4.4(f), it is obvious that as the major population, the (00.2) twin grains had a very small tensile residual strain in the pre-deformed sample. Moreover, the (10.1) tensile residual strain in the pre-deformed sample was higher than the as-received sample.

Figure 4.4(g) demonstrates the internal-strain evolution of certain *hkl*s during the reverse tension in the axial direction for the as-received sample. In the stress range III, the lattice strain of (11.0) detwinned grains was higher than otherwise-oriented grains. The (00.2) twin grains started to yield, when the stress approached the stress range III, and completely saturated in the stress range IV. The lattice strain of (10.0) and (11.0) detwinned grains was enhanced rapidly in the stress ranges IV and V. In particular, the lattice strain was built up in (10.0) detwinned grains quickly. Generally, the lattice-strain evolution in the as-received and pre-deformed samples during the reverse tension was similar. The difference lays in the rate of the lattice-strain increase in (10.0) detwinned grains. The rate of the lattice-strain increase in the pre-deformed sample was not as fast as in the as-received sample.

4.1.3 Discussion

Relationship between the macroscopic mechanical behavior and microscopic response: As presented in Figs. 4.1 and 4.2, the stress-strain curve can be divided into two sections in the plastic deformation region under compression for both the as-received and pre-deformed samples, based on the macroscopic-hardening-rate changes. Figure 4.3

illustrated the diffraction peak intensity evolution of certain *hkl*s in the axial direction by the real-time in-situ neutron diffraction measurement and simulations for both samples. It is clear that in the stress ranges I and i, respectively, a slow and steady work hardening can be observed macroscopically for the as-received and pre-deformed samples in Fig. 4.2. Microscopically, the diffraction peak intensity of (10.0) and (11.0) grains decreased significantly, meanwhile, the diffraction peak intensity of (00.2) twin grains increased dramatically in Fig. 4.3. It is well known [172] that a sudden re-orientation of grains of approximately 86^{o} occurs during tensile twinning-dominated deformation, owing to the HCP structure of Mg, which results in the simultaneous variation in the diffraction peak intensity for (10.0) and (00.2) grains in one diffraction bank. It is also confirmed by the simulation results that the twin volume fraction, f^{tw}, enhances considerably in this stress range in Fig. 4.5, and the relative activity of tensile twinning became dominant in Fig. 4.6. Therefore, the stress range I/i can be defined as the tensile twinning-dominant deformation region. In the stress range II/ii, a rapid strain hardening can be observed in Figs. 4.1 and 4.2, while the rate of diffraction peak intensity changes in (10.0) and (00.2) grains decelerated in Fig. 4.3. This trend indicates that the volume of tensile twinning kept rising but tended to exhaust. In the meantime, the hard deformation mechanisms (i.e., prismatic or pyramidal dislocation slip) under the current loading condition were activated and became dominant in the twin grains [43, 45]. The simulation results manifest that the rate of the twin-volume fraction increase tends to decline in Fig. 4.5, in this stress range. Moreover, the basal <a> slip turns out to be dominant, while the prismatic and pyramidal <a> slips also become active, as demonstrated in Fig. 4.6. Consequently, the stress range II/ii can be characterized as the transition region from

tensile twinning- to dislocation-dominated deformation. Similarly, during the reverse tension, the stress ranges III/iii and IV/iv can be labeled as detwinning-dominated, and transition from detwinning- to dislocation-dominated deformation, respectively. In the stress range V/v, an uninterrupted declined work-hardening rate can be perceived in Fig. 4.2, as the diffraction peak intensities of (10.0), (00.2), and (11.0) grains cease changing in Fig. 4.3. So, it can be tagged as the dislocation-dominated region.

The current study demonstrates that the relationship between the macroscopic mechanical behavior and microscopic response at a grain level can be clarified and elucidated by real-time in-situ neutron diffraction measurements. Moreover, the EVPSC-TDT model can be employed to quantify the deformation mechanisms during the strain-path changes.

The activation of the extension twinning: It has been acknowledged that the Schmid law [Eq. (22)] is valid to calculate the onset of deformation twinning by assuming that the deformation twinning is governed by CRSS on the twin plane and in the twinning direction under a uniaxial loading condition [43, 45, 46, 86, 87, 173].

$$\tau_{CRSS} = \sigma_c \cos\lambda \cos\chi \tag{22}$$

where τ_{CRSS} is the CRSS, σ_c is the critical applied stress, λ and χ are the angles between the loading axis and twin plane normal and between the loading axis and the twinning direction, respectively. The lattice strain of (00.2) grains in the radial direction was used to calculate the onset of activation of tensile twinning during compression. As marked in Figs. 4.4(c) and (d), the (00.2) grains began to yield, when the lattice strain reached 415 and 677 με for the as-received and pre-deformed samples, respectively.

Multiplying the Young's modulus of (00.2) for Mg (48 GPa) with lattice strain, the critical applied stress can be attained. Since the values of both λ and χ equal approximately 45^{o}, the CRSS of the as-received sample can be determined to be 10.0 MPa, which is somewhat lower than the results from previous studies [43, 45, 173]. The calculated CRSS of the pre-deformed sample is 16.2 MPa, which is higher than the as-received sample. It suggests that the activation of tensile twinning in the pre-deformed sample is more difficult than the as-received sample.

It has been recognized that the onset of tensile twinning is governed by the CRSS. In the current study, the pre-deformed sample exhibits the higher CRSS for the activation of the tensile twinning than the as-received sample. It is believed that the high CRSS in the pre-deformed sample results from the intergranular residual strain/stress due to the deformation history. As shown in Fig. 4.4(d), the compressive intergranular residual strain was observed in (00.2) twin grains in the radial direction in the pre-deformed sample, which is caused by the pre-deformation. It is abnormal for Mg, since the tensile intergranular residual strain was usually expected in the radial direction after tension deformation. A possible mechanism can be proposed that in order to activate the tensile twinning, the compressive residual strain needs to be overcome in the pre-deformed sample, which leads to a high CRSS.

The deformation-twinning mechanism can be categorized into two stages: twin nucleation and twin propagation. It is believed that the early stage of tensile twinning is governed by the twin nucleation [34], while the later stage is controlled by the twin propagation. By introducing a large amount of dislocations through in-plane tension in the current study, which serve as the twin nucleation sites, the twin nucleation process

should be facilitated. Therefore, as long as the tensile twinning is activated, the twinning process could be accelerated. It agrees with the experimental observation in the present research that the shorter duration of twinning and detwinning process in the pre-deformed sample than the as-received sample.

The detwinning process: During unloading, the pseudoelastic behavior can be observed in the stress-strain curves for both samples, in Fig. 4.1. In previous studies, it was stated that the detwinning process occurred immediately upon unloading in wrought Mg alloys [43, 45]. The pseudoelastic behavior of wrought Mg alloys was attributed to the detwinning process previously [81, 174]. In our previous paper [164], it is claimed that no detwinning was observed during unloading from the bulk average neutron diffraction results in both samples, since no apparent simultaneous diffraction peak intensity variation could be detected in (10.0) and (00.2) grains in the same detector bank, as displayed in Fig. 4.3. In the current paper, the EVPSC-TDT model was employed, and the simulation results indicate that the twin volume fraction, f^{tw}, kept almost constant for both samples (Fig. 4.5), and the basal <a> slip rules over other deformation modes (Fig. 4.6) during unloading, which agrees well with real-time in-situ neutron diffraction observation. Although the tensile twinning became more active by the end of unloading in both samples as seen in Fig. 4.6, the amount of grains involved in detwinning during the unloading must be very few, since no simultaneous diffraction peak intensity variation can be detected from the real-time in-situ neutron diffraction measurement.

In our previous paper [164], it states that no apparent detwinning process can be identified even in the elastic region during the reverse tension for both samples, as shown in Fig. 4.3. Although the diffraction peak intensity of (00.2) twin grains decreased in the

elastic region during the reverse tension in the pre-deformed sample, no simultaneous diffraction peak intensity variation can be detected in (10.0) grains. This phenomenon is attributed to the grain rotation resulting from the microscopic stress relaxation and macroscopic rapid stress drop [164, 175]. In the present paper, the EVPSC-TDT simulation results approve that no apparent detwinning occurred as demonstrated in Fig. 4.5 that no obvious twin volume fraction varied in the early stage of the elastic region during the reverse tension for both samples and in Fig. 4.6 that basal slip was the dominant deformation mode in nearly all the elastic region.

The pronounced detwinning process did not occur, until the applied stress passed the yield strength during the reverse tension. A certain amount of lattice strains (2,181 and 2,145 με in the as-received and pre-deformed samples, respectively) has to be accumulated in twin grains before detwinning, as marked in Figs. 4.4(g) and (h). It is thought to account for the little difference in the tensile yield strength during the reverse tension between the as-received and pre-deformed samples. The EVPSC-TDT simulation results in Fig. 4.5 exhibit that (1) in the stress range III/iii the twin volume fraction decreased dramatically, (2) in the stress range IV/iv the trend of the decrease became gradually, and (3) in the stress range V/v the twin volume fraction kept constant. It indicates that the massive detwinning process occurred in the stress range III/iii and the detwinning process was completed by the stress range V/v, which agree with the experimental observation very well. For the as-received sample in Fig. 4.6, it reveals that (1) in the stress range III the detwinning process was the dominant mode, (2) in the stress range IV the basal <a> slip ruled over other deformation modes and prismatic <a> slip became more and more active while the detwinning became less and less active, and (3)

in the stress range V the basal <a> slip and prismatic <a> slip turned out to be equally dominant and detwinning remain inactive. The pre-deformed sample has a comparable trend as the as-received sample, but there are some differences, such as in the pre-deformed sample, the detwinning deformation mode was dominant for the most time in the stress range iv, and the basal <a> slip was the dominant deformation mode, and the prismatic <a> was inactive in the stress range v.

4.1.4 Summary

The real-time in-situ neutron diffraction technique under a continuous loading condition and numerical simulations using the EVPSC-TDT model were employed to study the plastic-deformation dynamics on twinning and detwinning behavior of the wrought AZ31B Mg alloy. An effective relationship has been established between the macroscopic mechanical properties and the microscopic response. The following conclusions can be drawn based on the present research:

(1) The plastic deformation can be divided into several stages during the compression and reverse tension, based on the work-hardening-rate variations. In each stage, a certain deformation mode becomes dominant, which is characterized by real-time in-situ neutron diffraction and supported by simulation results.

(2) An obvious strengthening behavior was obtained during compression by pre-tension. However, the pre-deformation has limited impacts on mechanical behavior during the reverse tension.

(3) It is evident that the residual strain is responsible for the delay of the onset of tensile twinning in the subsequent compression in the pre-deformed sample.

However, by increasing the dislocation density through pre-tension, the twinning and detwinning process can be accelerated, once the twinning or detwinning process was activated.

(4) As previously reported [44], no apparent detwinning activities were observed during unloading after compression. Detwinning did not occur until the applied stress was beyond the tensile yield strength during the reverse tension.

(5) In the pre-deformed sample, grain rotation is thought to account for the diffraction peak intensity decrease in (00.2) twin grains in the elastic deformation region during the reverse tension, since no simultaneous diffraction peak intensity changes in (10.0) grains was detected.

(6) The EVPSC-TDT model was employed for the first time to predict the deformation dynamics under a continuous-loading condition during strain-path changes in a HCP-structured Mg alloy. The simulation results concur with the experimental observation of the alternate deformation mechanisms during the strain-path changes.

4.2 Deformation Twinning in an Individual Grain using In-Situ Synchrotron X-ray Microbeam Diffraction

4.2.1Tensile twinning and detwinning behavior at a sub-micron length scale

The grain orientation maps were constructed to characterize the twinning and detwinning behavior of a wrought AZ31B Mg alloy at three strain levels using in-situ synchrotron X-ray microbeam diffraction measurements with white beam, as shown in Fig. 4.7. The grain orientation map of the un-deformed sample is illustrated in Fig. 4.7

(a).The sample surface located at 0 μm depth, discerned with black solid line. In total 8 distinct grains were identified from sample surface to ~ 140 μm into the material. The grain size varied from 20 to 100 μm. The grain orientation of 8 grains was displayed in Fig. 4.7(b). The (00.1) poles in the most of grains (except grain ⑤) are close to ND, which is known as the typical rolling texture. It should note that in the current study all of the Laue patterns were indexed with respect to the sample surface normal direction [Q vector of (00.1) planes in the sample surface normal direction]. The crystalline plane of grain ①in the sample surface normal direction is $(\bar{1}1.6)$, which is about 17.4^{o} apart from (00.1) plane. In the current study, the grain ①, which is approximately 50 μm beneath the sample surface and 100 μm grain size, was chosen for the in-situ measurement, because the twinning and detwinning were highly possible to appear in grain ① during the specific customized loading-path changes. The grain orientation of grain ① at 3% compression strain [point (ii) in Fig. 3.5(b)] was exhibited in Fig. 4.7(c). The red dotted line symbolizes the shape of grain ① before deformation. A small portion of "parent grain" was remained after deformation. It should point out that in the current study when the Q vector of (00.1) planes is parallel to the loading direction, the diffraction pattern cannot be indexed, therefore the blank area inside red dotted line was identified as tensile twins with nearly 90^{o}misorientation with the parent grain ①. Figure 4.7(d) is the grain orientation map after 7% compression – relative 3% reverse tension [point (iii) in Fig. 1(b)], which is the same area marked by black dotted rectangle in Fig. 4.7(c).The size of Fig. 4.7(d) and black dotted rectangle in Fig. 4.7(c) is the same for the comparison. After

reverse tension, the remained parent grains were recovered, due to the detwinning process.

Figures 4.8 demonstrate the diffraction peak intensity and d-spacing variation of $(\bar{1}2.8)$ peak as a function of sample depth at three different locations [3,878, 3,880, and 3,882 μm on X-axis in Fig. 4.7(c)] under 3% compression strain [point (ii) in Fig. 3.5 (b)] during twinning dominated deformation using monobeam energy scan. The $(\bar{1}2.8)$ peak is chosen arbitrarily. As show in Fig. 4.8(a), the diffraction peak intensity of $(\bar{1}2.8)$ went to zero around 76 μm depths, which means the other orientation grains appear. Comparing with Fig. 4.7(c), the tensile twins emerged at 76 μm depth in the remained parent grain, when the distance is 3,878 μm on the X-axis. Hence, it is reasonable to claim that a tensile twin appears at approximately 76 μm depth, which is indicated by a dotted orange colored rectangle. It manifests that the monobeam energy scan results are consistent with white beam grain orientation mapping. The same twin band can be observed at the distance of 3,880 μm [Fig. 4.8(b)], but no twins can be found at 3,382 μm position [Fig. 4.8(c)]. Since the Q vector was measured by in-situ synchrotron X-ray microbeam diffraction in the sample surface-normal direction, when the sample was compressed along axial direction, the measured d-spacing of a certain *hkl* was under tension loading, and vice versa. Fig. 4.8(d) demonstrates the d-spacing evolution of $(\bar{1}2.8)$ peak in a parent grain as a function of depth at a distance of 3,878 μm on the X-axis. In general, the d-spacing of $(\bar{1}2.8)$ peak is decreased with the increase of the sample depth. A dramatic d-spacing decrease can be discovered at 76μm depth, where a twin is located in the remained parent grain marked as orange colored rectangle. It

indicates that the d-spacing of $(\bar{1}2.8)$ peak in a parent grain varies significantly on the two sides of a twin. Moreover, the relatively large plateaus of d-spacing in remained parent grains can be found near twins, as shown in Fig. 4.8(d) and (e).

Figure 4.9 exhibits the diffraction peak intensity and d-spacing variation of $(\bar{2}1.8)$ peak in remained parent grains as a function of sample depth at three different locations [3,439, 3,441, and 3,443 μm on X-axis in Fig. 4.7(d)] after 7% compression – relative 3% reverse tension [point (iii) in Fig. 3.5(b)] during detwinning dominated deformation. The twins are indicated as the dotted orange colored rectangles. Generally, the d-spacing of $(\bar{2}1.8)$ peak in a parent grain near surface side is higher than the other side, similar to 3% compression condition, as shown in Fig. 4.9(d), (e), and (f). However, unlike Fig. 4.8(d) and (e), no apparent d-spacing variation of $(\bar{2}1.8)$ peak in a parent grain can be observed on the two sides of the twins. The d-spacing of $(\bar{2}1.8)$ peak decreases constantly with the sample depth.

4.2.2 Discussion

The in-situ synchrotron X-ray microbeam diffractionhas been employed in the current study to investigate twinning and detwinning behavior of a wrought AZ31B Mg alloy in an individual grain. To the best of authors' knowledge, it is the first time that the twinning and detwinning behavior has been observed in-situ in a single grain inside a polycrystalline HCP-structured Mg alloy.

It has been proven that the tensile twinning can be easily activated during in-plane compression or through-thickness tension in rolled Mg alloys through in-situ EBSD and neutron diffraction measurements. In the current study, it is evident that the tensile

twinning occurred during compression along the RD, as shown in Fig. 4.7(c). The majority of a grain has been twinned, and only a small portion of the parent grain was persisted at 3% compression strain. Moreover, the remained parent grain was separated into several small grains.

Two possible detwinning mechanisms have been proposed by Wang and co-authors that (1) a propagation of parent grains into twin grains by migration of twin boundaries into the twins via the glide of the twinning dislocations, and (2) a shrinking of the twinned region through twin nucleation inside the twin by means of the activation of twinning dislocations inside the twinned region. In the present study, the first mechanism, a propagation of a parent grain into a twin grain, was witnessed, as present in Fig. 4.7(d). The detwinning process was governed by the motion of the twinning dislocations toward a twin grain.

The d-spacing evolution in the parent grain during twinning and detwinning processes has been investigated using monobeam energy scan. It was found that the d-spacing of the parent grain on the surface side is much higher than the inside for both twinning and detwinning processes, as shown in Fig. 4.8 and 4.9. Moreover, the d-spacing decrease gradually in the parent grain with the increase of the sample depth. It is interesting to note that a distinct d-spacing decrease on two sides of a twin band during the twinning deformation, as presented in Fig. 4.8 (d) and (e). It suggests that a tensile strain was supposed on the twin, which could facilitate the motion of twinning dislocations toward the parent grain. On the contrary, no d-spacing variation on two sides of twin bands can be discerned during detwinning deformation, as demonstrated in Fig. 4.9 (d), (e), and (f). The d-spacing decreases rapidly in the remained parent grains. The

parent grains suffered the tensile strain, which could assist the twin boundaries move toward parent grains.

4.2.3 Summary

The twinning and detwinning behavior in an individual grain in a wrought AZ31B Mg alloy has been investigated using in-situ synchrotron X-ray microbeam diffraction at sub-micro level. The grain orientation mapping was performed using white beam scan, and the d-spacing evolution was measured using monobeam scan under different strain levels. The main results can be summarized as follows:

(1) The tensile twinning and detwinning process have been observed in an individual grain for a HCP structured Mg alloy during in-situ compression and reverse tension, respectively, along RD.

(2) The operation of detwinning process was through the migration of twin boundaries into the twins via the glide of the twinning dislocations.

(3) The distinct d-spacing decrease in a parent grain can be observed on two sides of twin during twinning dominated deformation, but no d-spacing variation was detected during detwinning dominated deformation.

4.3 Low-Cycle Fatigue Behavior using Real-Time In-Situ Neutron Diffraction

4.3.1 Macroscopic low-cycle fatigue behavior

The hysteresis loops at selected fatigue cycles for the real-time in-situ neuron diffraction measurement are plotted in different colors, as shown in Fig. 4.10(a). The Roman numerals, I, II, III, IV, V, and VI, marked in Fig. 4.10(a) stands for maximum

strain (+ 2%), zero stress on the tensile strain side, zero strain during compression, minimum strain (– 2%), zero stress on the compressive strain side, and zero strain during tension, respectively, which will be used throughout the paper. The asymmetry shape of the hysteresis loops can be witnessed through the entire fatigue life (sample failed at the 71st cycle). In general, the tension side of stress-strain curve demonstrated a typical concave-down shape, while the compression side exhibits a concave-up shape. However, in the 1st cycle (black line), a sigmoidal shape with the concave-down first and followed by concave-up can be noticed. It is distinct that the shape of stress-strain curve in the first cycle is very different from the other fatigue cycles. For the 1st tension in the 1st cycle [marked in the Fig. 4.10(a)], the yield strength is much lower than the following fatigue cycles in the tension side. Moreover, the entire stress-strain curve of the 1st tension in the 1st cycle is below that of the other fatigue cycles during tension. During the compression in the 1st cycle, stress-strain curve exhibits a stable strain hardening, followed by a sudden strain hardening, and then another constant strain hardening, while the stress-strain curve in the other fatigue cycles displays a steady strain hardening, and followed by a rapid strain hardening. The mechanical behavior of the 2nd tension in the 1st fatigue cycle is comparable with that in the following fatigue cycles.

The peak stresses at maximum and minimum strains [black solid square symbols, corresponding to I and IV in Fig. 4.10(a), respectively], the compressive and tensile stresses at zero strain [blue open triangle symbols corresponding to III and VI in Fig. 4.10(a), respectively], and mean stress (red open circle symbols) variation during the low-cycle fatigue are displayed in Fig. 4.10(b). The compressive peak stresses are much higher than the tensile peak stresses in each selected fatigue cycle, which lead to a

compressive mean stress throughout the fatigue life. The apparent strain hardening can be distinguished from the tensile peak stress evolution in the first five cycles, followed by a stable cyclic stress response. On the other hand, the compressive peak stress saturated after two fatigue cycles. The consistence of mean stresses during the fatigue tests can be perceived. It is interesting to note that the tensile and compressive stresses at zero strain during the low-cycle fatigue are comparable. A slight increase can be identified in both the tensile and compressive stresses at zero strain in the first five cycles, and then no changes.

The yield strength evolution of the selected fatigue cycles is plotted in Fig. 4.10(c). The tensile yield strength in the 1^{st} tension in the 1^{st} fatigue cycle was only 65 MPa, which is much lower than that in the other fatigue cycles. The tensile yield strengths keep increasing in the first 5 cycles, and then stay unchanged. The compressive yield strengths increased continuously until the 50^{th} cycle. There is no change in the compressive yield strength between the 50^{th} and 70^{th} cycle. The tensile yield strengths were higher than the compressive yield strengths in the whole fatigue life. It appears that in the early fatigue life, up to 20^{th} cycle, the differences between the tensile and compressive yield strength decreased persistently, while it remains unchanged from the 20^{th} to 70^{th} cycle. The yield strength evolution in Fig. 4.10(c) shows an opposite trend, compared with the peak stress variation in Fig. 4.10(b).

The plastic strain on the tension side [II in Fig. 4.10(a)], the plastic strain on the compression side [V in Fig. 4.10(a)], and the plastic strain amplitude, $\Delta\varepsilon_p/2$, as a function of fatigue cycles were shown in Fig. 4.10(d). The tensile plastic strains are marginally higher than compressive plastic strains during low-cycle fatigue. For the

plastic strain on the tension side, a slight decrease can be discerned in the early fatigue life (up to 5th cycle), and then the tensile plastic strains cease changing in the following fatigue cycles. The plastic strains on the compression side remain unchanged in the entire fatigue life. There is little change in the plastic strain amplitude evolution during fatigue.

The work-hardening rates as a function of applied stresses in each selected fatigue cycles were elucidated individually in Fig. 4.11. The hardening rate can be calculated based on the well-known equation below:

$$\theta = \frac{d\sigma}{d\varepsilon} \tag{21}$$

where θ is the work-hardening rate, σ is the stress, and ε is the strain. In the first cycle as revealed in Fig. 4.11(a), during the 1st and 2nd tension (top and bottom figures, respectively), the work-hardening rates stay constant. However, for the compression in the 1st cycle, the curve of work-hardening rate versus applied stress can be divided into three regions: (1) below – 77 MPa, the work-hardening rate keeps unchanged; (2) between – 77 and – 129 MPa, the work-hardening rate increases rapidly; and (3) beyond – 129 MPa, the work-hardening rate decreased gradually. From the 2nd to 10th cycles [in Fig. 4.11(b), (c), and (d)], during the tension, the constant work-hardening rate can be distinguished. In the 20th, 50th, and 70th cycles, there are insignificant increases in work-hardening rate, higher than 2,000 MPa, after approximately 130 MPa tensile stresses. For the compression in the 2nd cycle, the work-hardening rate vs. applied stress curve can be separated into three regions: (1) beneath – 110 MPa, a stable work-hardening rate can be seen; (2) from – 110 MPa to – 217 MPa, the work-hardening rate increases gradually; and (3) above – 217 MPa, the work-hardening rate decreases. However, in the 5th, 10th, 20th,

50^{th}, and 70^{th} cycle, the work-hardening rate vs. applied stress curve can only be split into 2 regions, (1) a steady work-hardening rate, and (2) an increase of work-hardening rate. The applied stress at the splitting point increased slowly with fatigue cycles.

4.3.2 Microscopic response

The two-dimensional (2-D) and three-dimensional (3-D) real-time in-situ neutron diffraction results of the measured d range for both axial and radial direction during the low-cycle fatigue were presented in Fig 4.12. The deformation dynamics in each selected fatigue cycles, including the simultaneously evolution of d-spacing, diffraction peak intensity, and diffraction peak width evolution of certain *hkl*s in both axial and radial directions, were illustrated. In the axial direction, as presented in Fig. 4.12(a), the diffraction peak intensity of (10.0) grains experiences appear-disappear and the d-spacing of (00.2) grains undergoes repeatedly increase-decrease sequence during tension-compression in each fatigue cycle, corresponding to the twinning-detwinning deformation. In Fig. 4.12(c), the diffraction peak intensity of (00.2) grains in the axial direction exhibits repetitively increase-decrease, designating the twinning-detwinning behavior during cyclic loading. The opposite trend can be perceived in the radial direction, as displayed in Figs. 4.12(b) and (d).

The diffraction peak intensity evolution of certain *hkl*s in both axial and radial directions in the selected fatigue cycles was presented in Fig. 4.13(a) and (b), respectively. As previously mentioned, the tensile twinning-dominated deformation leads to a sudden re-orientation of grains of approximately 86^{o}, owing to the HCP structure of magnesium. Consequently, when tensile twinning is activated (tension along ND in the

present study), the diffraction peak intensity of (00.2) grains decreases, which is the majority in the axial direction, and the (10.0) diffraction peak intensity increases simultaneously on the same detector bank. While in the radial direction, the opposite trend can be anticipated that the (00.2) diffraction peak intensity increases and (10.0) peak intensity decreases. The repetitive increase-decrease or decrease-increase can be distinguished from diffraction peak intensities of (10.0), (00.2), and (11.0) grains in both axial and radial directions during the fully reversed low-cycle fatigue, as demonstrated Fig. 4.13(a) and (b). The simultaneously variation of diffraction peak intensities of (10.0) and (00.2) grains, also, can be found on the same detector bank. It manifests that the alternative twinning and detwinning deformation occurred during tension-compression loading sequence in each fatigue cycle. Moreover, the diffraction peak intensity of (00.2) grains in axial direction (red solid symbol) at + 2% strain in each fatigue cycle decreases in Fig. 4.13(a) [or increases in Fig. 4.13(b)] progressively with the increase of fatigue life (marked as the purple dashed line), suggesting more and more (00.2) grains involved in tensile twinning deformation. It should point out that, in the 1^{st} fatigue cycle, the diffraction peak intensity decrease in (00.2) grains during the 1^{st} tension was apparently less in Fig. 4.13(a) [or more in Fig. 4.13(b)] than during the 2^{nd} tension, which is cause by the different tension strains. As shown in Fig. 4.10(a), the tension strain after 1^{st} tension of the 1^{st} cycle was 2%, while that after 2^{nd} tension became 4% (from – 2% to 2%). Furthermore, in the 1^{st}, 2^{nd}, 5^{th}, and 10^{th} fatigue cycles, the diffraction peak intensity of (00.2) grains fully recovered during compression, as shown in Fig. 4.13(a) and (b). However, after 10^{th} cycles, the diffraction peak intensity of (00.2) grains at -2% gradually decreases in Fig. 4.13(a) [or increases in Fig. 4.13(b)] with the rise of fatigue cycles

(marked as the green dashed line). It implies that, in the first 10 fatigue cycles, the twins from tension are fully detwinned during the compression in each fatigue cycle, while, from the 20th fatigue cycle, the accumulated residual twins appear.

The internal strain evolution of certain *hkl*s in the axial direction in the selected fatigue cycles was presented in Fig. 4.13(c). During tension, the lattice strain of (11.0) grains is higher than that of (10.0) and (00.2) grains at the same macroscopic stress level through the fatigue life, while the lattice strain of (10.0) grains and (00.2) grains are similar. In addition, the lattice strain of (11.0) grains at + 2% strain was enhanced apparently with fatigue life, but only insignificant increase in lattice strain of (10.0) grains and (00.2) grains can be discerned. During compression, the lattice strain of (00.2) grains at – 2% strain was decreased with increase of fatigue cycles, while that of (11.0) grains was kept rising.

The diffraction peak width evolution [full width at half maximum (FWHM)] of (00.2) grains in the axial direction during cyclic loading in each selected fatigue cycle is presented in Fig. 4.13(d). In each selected fatigue cycle, a distinct peak can be detected, starting from the beginning of the rapid strain hardening region during compression, reaching to the highest value when the compressive strain reach to – 2%, and falling down in unloading after compression and the elastic region in the reverse tension. When the applied compressive stress was in the steady strain hardening region and tensile stress was above the yield strength, the recurrent ups and downs of diffraction peak width in the (00.2) grains was noticed. Overall, the diffraction peak width of the (00.2) grains grew with fatigue life (marked as purple dashed line).

It is worth to emphases that the twinning and detwinning deformation modes can be determined from the simultaneous diffraction peak intensity variation of (10.0) and (00.2) grain on the same detection bank. Additionally, basically no intense variation of diffraction peak intensity in different *hkl*s can be observed during the dislocation dominated deformation. Correspondingly, the twinning, detwinning, and dislocation dominated deformation can be distinguished from the diffraction peak intensity evolution in a qualitative manner. The diffraction peak intensity evolution of certain *hkl*s in the axial direction during fully-reversed fatigue cycles was demonstrated in Fig. 4.14, in which the loading sequence was marked. Based on the work-hardening rate changes in Fig. 4.11, the tension and compression were separated into several regions in the 1st cycle, as illustrated in Fig. 4.14(a), including: (1) In the elastic region the 1st tension, no diffraction peak intensity variation of (10.0), (00.2), and (11.0) grains can be detected. (2) After tensile yield strength, the diffraction peak intensity of (00.2) grains decreases, while that of (10.0) and (11.0) grains enhances simultaneously, suggesting a tensile twinning dominated deformation. (3) During unloading after tension, no diffraction intensity changes in (10.0), (00.2), and (11.0) grains can be detected, indicating that no detwinning occurred. (4) In the elastic region during the compression, instantaneous diffraction peak intensity variation in (10.0) and (00.2) grains can be identified, representing that detwinning is activated. (5) When the applied stress is between – 33 MPa (compressive yield strength) and – 77 MPa [the beginning of the steady work-hardening rate region as marked in the middle figure in Fig. 4.11(a)], the diffraction peak intensity of (00.2) grains increases significantly, accompanying with the decrease of (10.0) and (11.0) diffraction peak intensities, recognizing as detwinning dominated deformation region. (6) When the

compressive stress is from – 77 MPa to – 129 MPa [the rapid strain hardening region as marked in the middle figure in Fig. 4.11(a)], the diffraction peak intensity of (10.0) and (11.0) grains disappear completely and of (00.2) grain increased slowly, which represents that the twins are fully detwinned, and the dislocation deformation mode is activated, designating as transition region from detwinning to dislocation dominated deformation. (7) When the sample is further compressed beyond – 129 MPa [the work-hardening rate constantly decease region as marked in the middle figure in Fig. 4.11(a)], it is labeled as dislocation dominated deformation, since no diffraction peak intensity change in (10.0), (00.2), and (11.0) grains can be discriminated. (8) In the following unloading, there is no diffraction peak intensity variation in different *hkl*s. (9) In the elastic region in the 2nd tension in the 1st cycle, the tensile twinning did not happen since no simultaneous diffraction peak intensity changes in (10.0) and (00.2) grains. (10) As the applied stress exceeded the tensile yield strength in the 2nd tension in the 1st cycle, the tensile twinning deformation mode can be decided, because the decrease of diffraction peak intensity of (00.2) grains accompanies with the increases of (10.0) diffraction peak intensity. Based on the real-time in-situ neutron diffraction measurement results, the dominant deformation modes in different deformation stages within each fatigue cycle are labeled in both Fig. 4.11 and Fig. 4.14. All of the tension region in all of the fatigue cycles, as presented in Fig. 4.14, can be divided into two sessions: elasticity (before yielding) and tensile twinning deformation (after yielding). Comparing compression region in the 1st cycle [Fig. 4.14(a)] and 2nd cycle [Fig. 4.14(b)], the detwinning dominated deformation is completed faster, transition from detwinning to dislocation region is narrower, and the dislocation dominated deformation region is much wider in the 1st fatigue cycle than the

2^{nd} cycle. From the 5^{th} cycle, in the compression region, three discrete deformation modes (i.e., elasticity, detwinning dominated, and transition from detwinning to dislocation) are distinguished, and the dislocation dominated deformation region completely disappears. Moreover, from the 20^{th} fatigue cycle, a small amount of residual twins is discovered after compression, while the twins are detwinned completely in the 1^{st}, 2^{nd}, 5^{th}, and 10^{th} fatigue cycles. Furthermore, no detwinning occurs in unloading after tension in all selected fatigue cycles. The twinning dominated deformation mode takes place in the plastic deformation region, in the first five fatigue cycles. From the 10^{th} to 70^{th} fatigue cycle, a small amount of tensile twinning activities are spotted in the elastic region during tension, as shown in Figs. 4.14(d)-(g). Whereas, the detwinning dominated deformation is not initiated until compression in each selected fatigue cycle. Thus, it is evident that the low-cycle fatigue could facilitate the activation of the tensile twinning, but have little influence on the initiation of the detwinning deformation.

The lattice strain evolution of (00.2) grains as a function of applied stress in the axial direction in each selected cycle is demonstrated in Fig. 4.15. It should point out that the maximum and minimum lattice strain, the tensile and compressive residual lattice strain, and the lattice strains responsible for the activation of tensile twinning were marked on each figure. The Roman numerals, i, ii, iii, and iv, signify unloading after tension (elastic deformation), compression (detwinning and dislocation deformation modes), unloading after compression (elastic deformation), and tension (tensile twinning deformation mode), respectively, as shown in Fig. 4.15(h). The upper left inset in Fig. 4.15(a) is the lattice strain of (00.2) grains vs. applied stress in the 1^{st} tension in the 1^{st}

cycle. After unloading from the 1st tension, a small amount of tensile residual strain, 111 με, can be perceived. And a relative large amount of compressive residual strain, – 388 με, was witnessed after unloading from compression. The hysteresis loop of (00.2) lattice strain in each fatigue cycle exhibits tension-compression asymmetry, with the maximum compressive lattice strain higher than the maximum tensile lattice. The asymmetry in the stress-lattice strain of (00.2) grains hysteresis loop in the 1st fatigue cycle is more severe than the other fatigue cycles.

4.3.3 Discussion

Low-cycle fatigue behavior: The tension-compression asymmetry in the stress-strain hysteresis loop during the fully-reversed low-cycle fatigue in wrought Mg alloys is frequently observed in the previous studies [44, 99, 101, 102, 115, 176], which strongly depends on the strain amplitudes and strain ratio. It has been reported [101] that when the strain amplitude is lower than 0.45% the symmetry stress-strain hysteresis loop is observed in extruded AZ61A Mg alloys, owing to the absence of the twinning-detwinning activities. On the other hand, when the strain amplitude is high than 0.52%, the stress-strain hysteresis loop becomes asymmetry, due to the anisotropic plastic deformation caused by deformation twinning.

In the current study, the total strain amplitude was 2% resulting in an asymmetry shape of the stress-strain hysteresis loop, as presented in Fig. 4.10(a). The stress-strain curve of the 50th fatigue cycle is chosen for the detail analyses, because it is close to the middle fatigue life, as illustrated in Fig. 4.16(a). It has been confirmed the stress-strain curve during compression can be divided into two regions in the 50th fatigue cycle, based

on the work-hardening rate variation [the breaking point locates at – 136 MPa in Fig. 4.11(f)]. The real-time in-situ neutron diffraction results manifest that the two regions in compress are detwinning dominated deformation and transition from detwinning to dislocation dominated deformation, respectively, in Fig. 4.14(f). The tension deformation region with a steady work-hard rate in Fig. 4.11(f) can be identified as the tensile twinning dominated deformation, according to neutron diffraction peak intensity evolution of different *hkl*s in Fig. 4.14(f). Therefore, the stress-strain hysteresis loop of the 50^{th} fatigue cycle in Fig. 4.16(a) can be separated into three regions, including, (One) tensile twinning dominated deformation in tension (filled with diagonal pattern in red), (Two) detwinning dominated deformation in compression (filled with diagonal pattern in blue), and (Three) transition from detwinning to dislocation dominated deformation (filled with diagonal pattern in green). The dividing point of work-hardening rate change (a black dot) is marked in Fig. 4.16(a). An imaginary line (black dashed line) was drawn on Fig. 4.16(a), in consonance with the stress-strain flow in the detwinning dominated deformation region. It is obvious that the region (One) and (Two) are symmetric in shape to each other. The asymmetry shape of the stress-strain hysteresis loop results from the additional region (Three). It should emphases that the whole tension region (One) was rule over by the tensile twinning dominated deformation. As demonstrated in Fig. 4.13(a), the (00.2) grains in the axial direction were never fully twinned during low-cycle fatigue, since the diffraction peak intensity of (00.2) grain always higher than zero. In our previous study, the sample was fully twinned after 7 % strain [164]. In other words, a majority of grains is suitable for the tensile twinning, which happens to be the easiest deformation mode in the current loading condition (tension along ND), but only a portion

of those grains involves in twinning to achieve the imposed macroscopic strain (nearly 4% tensile strain in the current study). Moreover, it is very interesting to note the detwinning dominated deformation was completed with 2.7% strain. Unlike tension region with a large amount of grains applicable for tensile twinning, only the twinned grains could be involved in detwinning process, which is thought to be the main reason for the early exhaustion of detwinning in the compression. Hence, in order to accommodate a further imposed compressive strain, about 0.9% strain, the dislocation slip has to be activated, which is the main reason for the asymmetry shape of the stress-strain hysteresis loop.

The areas of stress-strain hysteresis loop above and below 0 MPa and their ratio was displayed in Fig. 4.16(b). The area of hysteresis loop above 0 MPa (black solid square) enhanced rapidly in the first 5 fatigue cycle, followed by a marginal increase. It indicates that more and more mechanical energy are required for the deformation in the first 5 fatigue cycles, which is caused by the work hardening. After that, comparable amount of mechanical energy is need in the following fatigue cycles, since the mechanical becomes stable. The variation of the area of hysteresis loop below 0 MPa (red solid square) has a similar trend as the area above 0 MPa, except in the 1^{st} fatigue cycle. The area of stress-strain hysteresis loop in the 1^{st} fatigue cycle is much larger than in the following fatigue cycles. The ratio of area of stress-strain hysteresis loop above 0 MPa over below 0 MPa (blue open circle) almost stayed at 1, except the 1^{st} fatigue cycle. It suggests that the areas of stress-strain hysteresis loop on tension side actually equal to the compression side, although the shape of hysteresis loop is asymmetry. The peak stresses (solid square), yield strengths (open circle), the stresses at dividing point between the

detwinning dominated deformation and transition region (open triangle), and the stresses at dividing point between the transition region and dislocation dominated deformation (open pentangle) as a function of fatigue life in the selected fatigue cycles are illustrated in Fig. 4.16(c). The stress ranges for tensile twinning dominated deformation (R1), detwinning dominate deformation (R2), and transition from detwinning to dislocation dominated deformation were filled with diagonal patterns by colors red, blue, and green, respectively. The transition region contributes nearly 50% of the compression peak stress in Fig. 4.16(c). The tensile peak stresses (black solid square) are comparable to the stresses at dividing point between the detwinning dominated deformation and transition region (red open triangle) in each fatigue cycle, except the 1^{st} cycle, as displayed on the top of Fig. 4.16(d). Moreover, the stress range for the tensile twinning dominated deformation, R1, is identical to the stress range for the detwinning dominated deformation, R2, as presented on the bottom of Fig. 4.16(d). Thus, it is further confirmed that the rapid strain hardening in the transition region is responsible for the asymmetry shape of stress-strain hysteresis loop.

Because the deformation anisotropy in HCP-structured polycrystalline wrought Mg alloys, the tensile mean stress is often witnessed during uniaxial fully-reversed low-cycle fatigue with relative high total strain amplitudes. The magnitude of mean stress depended on the strain amplitude, strain path, and sample orientation [100, 132, 177]. It has been reported that the reduced tensile mean stress can significantly diminish the asymmetry shape of the stress-strain hysteresis loop [111]. Moreover, it has been accepted that the tensile mean stress is detrimental to the fatigue resistance by facilitating

the fatigue crack initiation and propagation processes. In the present research, a compressive mean stress was introduced, as shown in Fig. 4.10(b). In the previous study [118], it is found that ND sample exhibit a superior fatigue resistance as compared to RD specimen in rolled AZ31B magnesium alloy at the same strain amplitude during low-cycle fatigue, which is attributed to the compressive mean stress that impedes the fatigue crack initiation and growth. However, the conflicted conclusion has been drawn by the other researchers that the ND sample has the lowest fatigue resistance [44] compared to RD and TD samples, which agrees with the results in the current study. In the present research, the compressive mean stress is acquired with the axial direction of the fatigue sample parallel to ND of the rolled plate. The mean stress in HCP-structured wrought Mg alloys significantly relies on the initial texture and the sample orientations. If the axial direction of the sample is along any direction in the rolling plane or extruded direction, the tensile mean stress can be expected under a relative large total strain (larger than 0.5%). It reveals that the compressive mean stress is not necessary for the better fatigue resistance and longer fatigue life in wrought Mg alloys during fully-reversed low-cycle fatigue. It is believed that the fatigue resistance and fatigue life of wrought Mg alloys greatly depends on the initial texture and the fatigue sample orientations.

Correlation between the macroscopic behavior and microscopic response in low-cycle fatigue: It has been approved that the real-time in-situ neutron diffraction measurements can be successfully employed to study the deformation dynamics and mechanisms of wrought Mg alloys during the strain-path changes [164]. In the present study, the work-hardening rate during tension in each selected fatigue cycle keeps almost constant (Fig. 4.11), which correlates with the tensile twinning dominated deformation (Fig. 4.14).

However, during compression, curves of work-hardening rate vs. applied stress can be separated into three regions (steady state, rapid increase, and gradually decrease regions) or two (steady state and rapid increase regions), as presented in Fig. 4.11. It is confirmed that a specific deformation mode was activated in each region by neutron diffraction results. The three regions during compression in the 1st and 2nd cycles, as demonstrated in the middle figure in Fig. 4.11(a) and (b) can be tagged as detwinning dominated deformation, transition from detwinning to dislocation dominated deformation, and dislocation dominated deformation, respectively, based on the diffraction peak intensity evolution of certain *hkl*s, as previously mentioned. The two regions during compression in the other selected fatigue cycles can be labeled as detwinning dominated deformation and transition from detwinning to dislocation dominated deformation.

Comparing the work-hardening rate variation during compression in the 1st cycle [the middle figure in 4.11(a)] with the 2nd cycle [the top figure in 4.11(b)], it is obvious that the stable and rapid increase regions are expanded, but the gradually decrease region almost disappeared in the 2nd fatigue cycle. It can be easily explained by neutron diffraction results in Fig. 4.14(a) and (b) that the detwinning dominated deformation and transition from detwinning to dislocation dominated deformation are finished much more slowly in the 2nd than the 1st fatigue cycle, which leads to broader steady and rapid strain hardening regions in the 2nd fatigue cycle. The dislocation dominated deformation occurred by the end of compression deformation in the 2nd cycle [Fig. 4.14(b)], which results in the work-hardening rate decrease region almost disappears [top figure in Fig. 4.11(b)]. The difference in the microscopic response during compression between the 1st

and 2nd fatigue cycles is considered to be responsible for the dissimilar hysteresis loop shape of stress-strain curve.

After the first two fatigue cycles, the stress-strain hysteresis loops are very resembling with each other [Fig. 4.10(a)]. In compression, the two regions (steady state and rapid increase regions) can be labeled as detwinning dominated deformation and transition from detwinning to dislocation dominated deformation in the work-hardening rate as a function of applied stress curve from the 5th to 70th cycle, as presented in Figs. 4.11(c)-(g).

As previously mentioned, overall, the diffraction peak width of (00.2) grains in the axial direction increased with the fatigue life, which is believed to be caused by the dislocation density increase during the cyclic loading. During the twinning and detwinning dominated deformation in each fatigue cycle, the diffraction peak width of (00.2) grains exhibit the recurrent ups and downs. Though the twinning and detwinning dominated deformation lead to the grain size changes, the contribution of the effect of grain size on the diffraction peak width must be very limited in the current study. In each fatigue cycle, a peak can be identified in the diffraction peak width evolution of (00.2) grains, which appears in the transition region (from detwinning to dislocation dominated deformation) during compression, reaching to the peak value when the compressive stress reach to the maximum value, decreasing upon unloading, and falling back when the applied stress reached to the tensile yield strength. There are three main sources for the diffraction peak broadening, including, the increase of the dislocation density, the increase of the applied stress, the decrease of the grain size. Since the diffraction peak

width is very insensitive to the grain size changes during the twinning and detwinning deformation, it is reasonable to believe that the spike of the diffraction peak width variation of (00.2) grains in each selected fatigue cycle mainly results from the dislocation density and the rapid stress changes. Moreover, in theory, unloading and elastic region in reverse tension will not affect the dislocation density. Therefore, the increase and decrease of diffraction peak width of (00.2) grains mainly results from the applied stress changes. It is noticed that the ending point is always higher than the beginning point of the spike in each fatigue cycle, which can be attributed to the increase of the dislocation density.

Therefore, in the current study, the relationship between the macroscopic mechanical behavior and microscopic response at grain level is successfully established using real-time in-situ neutron diffraction technique.

The twinning and detwinning behavior during low-cycle fatigue: The in-situ neutron diffraction has been employed to investigate the twinning and detwinning behavior in wrought Mg alloys using step-loading methods during cyclic loading [43-45, 135]. It has been established that the tension-compression strength asymmetry in wrought Mg alloys results from the mechanical twinning, e.g., tensile twinning is activated during in-plane compression and through-thickness tension in rolled plates or along extrusion direction compression in extruded bars, while the strength of material is controlled by the non-basal slip mechanisms in the reverse loading direction. Moreover, the alternative twinning-detwinning behavior was observed during the cyclic loading. With the increase of the fatigue cycles, the residual twins were detected, which is thought to be an

important factor to dictate the low-cycle fatigue behavior of wrought Mg alloys. In the present study, the similar conclusions can be drawn based on the real-time in-situ neutron diffraction results.

Besides the above mentioned phenomenon, it is found that deformation history has significantly impact on the tensile twinning, which tends to delay the activation of tensile twinning. As previously mentioned, the tensile yield strength in the 1st tension in the 1st fatigue cycle is much lower than the following fatigue cycles, as shown in Fig. 4.10(c). The tensile yield strengths in the selected fatigue cycles increase gradually in the first five fatigue cycles, and then cease changing in the following fatigue cycles. It has been widely accepted that the Schmid law [Eq. (22)] is valid to calculate the onset of deformation twinning under a uniaxial loading condition by assuming that the deformation twinning is governed by critical resolved shear stress (CRSS) on the twin plane and in the twinning direction [43, 45, 46, 54, 87]:

$$\tau_{CRSS} = \sigma_c \cos\lambda \cos\chi \tag{22}$$

where τ_{CRSS} is the CRSS, σ_c is the critical applied stress, λ and χ are the angles between the loading axis and twin plane normal and between the loading axis and the twinning direction, respectively. The CRSS variation as a function of fatigue cycles was exhibited in Fig. 4.17. It is obvious that the CRSS in the 1st tension in the 1st fatigue cycle is much lower than the other fatigue cycles. It manifests that the tensile twinning can be more easily activated in the anneal sample than the fatigued sample. Moreover, the CRSS variation in different fatigue cycles strongly depends on the residual lattice strain of (00.2) grains in the axial direction after compression. It is believed that the

compressive residual strain developed in each selected fatigue cycle, presented in Fig. 4.15, is responsible the increase of the yield strength and the postponement of the operation of the tensile twinning dominated deformation in tension.

On the other hand, the compressive yield strengths enhanced greatly in the first 2 fatigue cycles, then gradually increased until 50^{th} cycle, after that kept constant, which implies that the detwinning dominated process was postponed with the increase of fatigue life. The neutron diffraction results validate this statement by demonstrating the detwinning dominated deformation mode is activated upon unloading. In the elastic region during compression, detwinning operates in a relatively slow speed. The intense detwinning occurs, when the applied stress passes the yield strength, as shown in Figs. 4.13(a), 4.13(b), and 4.14. It is interesting to note that, in the whole fatigue life, the tensile yield strengths are higher than the compressive yield strengths in Fig. 4.13(c), which suggests that the operation of tensile twinning dominated deformation is more difficult than the detwinning dominated deformation.

The aforementioned the diffraction peak intensity of (00.2) grains decreased more and more in the axial direction (or increase more and more in the radial direction) as shown in Fig. 4.13(a) and (b), suggesting more and more grains involved in tensile twinning and detwinning deformation with the increase of fatigue cycles. Meanwhile, the stress ranges for twinning (R1) and detwinning dominated deformation (R2) increased with the fatigue life, in Fig. 4.16(d). It also confirms that the twinning and detwinning process was prolonged with the increase of fatigue cycles.

In our previous study [164], it states that no apparent detwinning occurred after unloading from compression (sample was machined from the same rolled plate as the current study with the axial direction parallel to the RD) during strain-path changes under uniaxial loading condition. The simulation results [120] have also indicated that no twin volume fraction changes and no twinning activities during unloading after the twinning dominated deformation. In the current research, as a matter of a fact, there is no obvious detwinning activities during unloading from previous tension deformation (tensile twinning dominated deformation), even by the end of fatigue life, as displayed in Fig. 4.14. The twinning and detwinning dominated deformation are prevailed in the plastic deformation region in the whole fatigue life, although the activation of tensile twinning is advanced in the elastic region during tension and detwinning arises upon compression.

Furthermore, the residual twins were observed in the early fatigue life (the 20^{th} fatigue cycle) and accumulated with the fatigue cycles. The previous researchers [45] state that the residual twins are in the "hard" orientation and difficult to be deformed. The residual twins also could serve as barriers to obstruct the dislocation motion. They are responsible for the hardening behavior in the twinning dominated deformation side of the stress-strain hysteresis loop. It agrees very well with our experimental observations in the current study.

The internal strain evolution during low-cycle fatigue: In the previous studies, the internal strain evolution has been investigated using step-loading controlled in-situ neutron diffraction methods under uniaxial loading condition. It has been concluded that once the tensile twinning is activated, it leads to a stress relaxation in parent and twin

grains relative to the surrounding grains in extruded ZK60 Mg alloys [43]. It has been found that the stress relaxation due to the tensile twinning in fine-grain alloys is much more significant than the coarse-grain alloys in extruded ZM20 Mg alloys [80]. Very recently, it has been reported that the loading modes (stress-control or strain-control and step-loading or continuous loading) has an obvious impact on (10.0) and (11.0) group of grains, in which a large amount of plasticity has been detected, but the (00.2) grains was unaffected by the loading modes in rolled HCP-structured Zircaloy-2 alloys [178].

In the current study, the internal strain evolution was investigated using real-time in-situ neutron diffraction method under continuous loading condition in strain control mode with a constant strain rate in each selected fatigue cycle. Only lattice strain variation of (00.2) grains in the axial direction was presented in the current paper, since there is no zero diffraction peak intensity in this group grains during the cyclic loading. In each fatigue cycle, the stress-lattice strain of (00.2) grains hysteresis loop can be witnessed with the obvious tension-compression asymmetry in Fig. 4.15. The areas of stress-lattice strain of (00.2) grains in the axial direction hysteresis loop above and below 0 MPa and their ratio were illustrated in Fig. 4.18(a). The area of stress-lattice strain of (00.2) grains hysteresis loop above 0 MPa has very little variation during the low-cycle fatigue. The area of stress-lattice strain of (00.2) grains hysteresis loop below 0 MPa has an analogous fashion as above 0 MPa, except in the 1^{st} fatigue cycle the area is larger than in the following fatigue cycles. The ratio of stress-lattice strain of (00.2) grains hysteresis loop above 0 MPa over below 0 MPa fluctuates around 0.4 through the fatigue life. Consequently, not only the shape but also the area of stress-lattice strain of (00.2)

grains hysteresis loop are asymmetric in the whole fatigue life, unlike the solely shape asymmetry in macroscopic stress-strain hysteresis loop as presented in Figs. 4.16(a) and (b).

The lattice strain evolution of (00.2) grains in axial direction at maximum and minimum macroscopic strains (+/– 2% strain) as a function of fatigue life was illustrated in Fig. 4.18(b). It is noticed that the peak values of the tensile lattice strain of (00.2) grains keeps increasing during the fatigue tests, because the work hardening during the fatigue. However, the maximum value of compressive lattice strain declined consecutively after 2 fatigue cycles, although the macroscopic compressive peak stress remains consistent after the first 2 cycles [in Fig. 4.10(b)], which is thought to be due to the accumulation of the residual twins with fatigue life. If the twinned grains are fully detwinned during compression, the load has to be imposed on the majority of grains, (00.2) grains at maximum compressive strain. With the existence of the residual twins, a portion of load has to be distributed to them. The real-time in-situ neutron diffraction results indicate that the residual twins appeared from the 20^{th} fatigue cycle [Fig. 4.13(a) and (b)], but there must be a small amount of residual twins before that, which are "invisible" to neutrons. Since the neutron diffraction measurement provide the bulk averaged information, a certain amount of residual twins has to be aggregated to become detectable. The lattice strain evolution of (00.2) grain in the axial direction indicates an early appearance of the residual twins in the 5^{th} fatigue cycle, than the diffraction peak intensity, in the 20^{th} cycle.

The lattice strain evolution of (00.2) grains in the axial direction in the 1st fatigue cycle was presented in Fig. 4.19. During the 1st tension in the 1st cycle, the lattice strain of (00.2) grains increased linearly in the elastic region, followed by a rapid increase in a small applied stress range from 64 to 68 MPa, and then ceasing to accept the lattice strain after 68 MPa. During the compression, the lattice strain of (00.2) grains deviates towards the lower side of linearity in the detwinning dominated deformation region, which indicates a stress relaxation behavior. In the transition and dislocation dominated deformation regions, the lattice strain of (00.2) grains diverges to the upper side of the linearity, which implies that the (00.2) grains tends to carry more load. In the 2nd tension in the 1st fatigue cycle, the lattice strain of (00.2) grains exhibit a zigzag shape in the twinning dominated deformation region. The lattice strain variation of (00.2) grain in the other selected fatigue cycles is very analogous to the compression and the 2nd tension in the 1st fatigue cycle. Subsequently, the lattice strain evolution of (00.2) grains in the axial direction has a strong connection with the alternative deformation modes in each fatigue cycle.

4.3.4 Summary

The real-time in-situ neutron diffraction has been taken advantage of in the current study to investigate fatigue mechanisms of a rolled AZ31B Mg alloy during fully-reversed strain-controlled low-cycle fatigue with total strain amplitude, 2%, under continuous loading-condition. The relationship between macroscopic low-cycle fatigue behavior and microscopic response at a grain level has been successfully established. The main conclusions were drawn based on the present research as follows:

(1) The rapid strain hardening in the transition region, from detwinning to dislocation dominated deformation, during compression is responsible for the asymmetry shape of stress-strain hysteresis loop, although the area of stress-strain hysteresis loop on tension and compression sides essentially equal to each other.

(2) The stress-strain curves in every fatigue cycle can be divided in to several regions based on the work hardening rate variation. In each region, an alternative twinning, detwinning, transition from detwinning to dislocation, and dislocation dominant deformation mode is activated.

(3) The fatigue resistance and fatigue life of HCP-structured wrought Mg alloys depends on the initial texture of the fatigue samples. The compressive mean stress is not necessary for the better fatigue resistance and longer fatigue life in wrought Mg alloys during fully-reversed low-cycle fatigue.

(4) With the increase of fatigue cycles, more and more grains involve in twinning and detwinning. The activation of tensile twinning is much more difficult in the fatigued sample than in the un-deformed sample, due to the residual strain. In the whole fatigue life, the activation of detwinning dominated deformation is easier than twinning dominated deformation.

(5) In the elastic region, there is no obvious twinning and detwinning activities. The twinning and detwinning dominated deformation modes occurred in plastic deformation regions in every fatigue cycle.

(6) The residual twins appear at early fatigue life, and being responsible for the hardening behavior in the twinning dominated deformation.

(7) The shape and the area of stress-lattice strain of (00.2) grains hysteresis loop stay asymmetric in the whole fatigue. The evolution of the maximum value of the lattice strain in the (00.2) grain in the axial direction is sensitive to the appearance of the residual twins.

(8) In the 1st tension in the 1st fatigue cycle, the lattice strain of (00.2) grains in the axial direction yield rapidly in twinning dominated deformation. In the following fatigue cycles, during compression, the lattice strain of (00.2) grains tends to relax in detwinning dominated deformation, and carry more load in the transition region. During tension, the zigzag shape of the lattice strain variation in (00.2) grains is observed during twinning dominated deformation.

4.4 Fatigue Crack Growth Behavior using In-Situ Neutron Diffraction

4.4.1 Twinning and detwinning behavior around fatigue crack tip

Figures 4.20(a) and (b) show the elastic-lattice strain and normalized intensity variations of the {00.2} peak in the normal direction [ND, Fig. 3.4(a)] as a function of the distance from the crack tip along the crack-propagation direction [RD, Fig. 3.4(a)] at various applied loads [i.e., 5 load points (LPs); LP1 (P_{max}), LP2 (P_{min}), LP3 ($1.3P_{max}$), LP4 (P_{max}), and LP5 (P_{min}), blue circles in Fig. 3.4(d)] during base-line tensile loading-unloading and subsequent tensile overloading-unloading cycles. For these measurements, the {00.2} orientation has a basal pole (c-axis) parallel to the normal direction (ND) of the plate, which is also the loading direction [see Figs. 3.4(a) and (b)]. Thus, the {00.2} grains are favorably oriented for the {10.2}<10.1> extension twinning in tension. Neither of the family of grains is oriented favorably for the <a>-slip on any planes.

When a base-line tensile loading was applied and then unloaded (LP2, Fig. 4.20), the compressive residual strains were developed up to about 1 mm ahead of the crack tip [Fig. 4.20(a)], and a larger increase in the {00.2} peak intensity from LP1 to LP2 was observed especially at the locations close to the crack tip [Fig. 4.20(b)]. The tensile overload of 2,990 N (= $1.3P_{max}$, LP3 in Fig. 4.20) was applied after the base-line tensile loading. The lattice strains, especially ahead of the crack tip, were significantly increased from LP2 to LP3 due to the higher stress concentration induced by overloading. On the other hand, a relatively smaller change of lattice strains was observed behind the crack tip. The tensile overload led to a more significant decrease in the {00.2} peak intensity than the base-line tensile loading [LP3 vs. LP1, Fig. 4.20(b)]. As the load was decreased from LP3 ($1.3P_{max}$, an overloading point) to LP4 (P_{max}), the magnitude of lattice strains at all investigated locations was slightly reduced, while the {00.2} peak intensities near the crack tip were partially increased. When the sample was further unloaded from LP4 to LP5, the enlarged compressive strains in both the magnitude and zone size were found in front of the crack tip, and the {00.2} peak intensities kept increasing. However, unloading followed by overloading did not lead to a full recovery of the decreased {00.2} intensities, as shown in the smaller {00.2} peak intensities of LP5 than LP2 at the locations from approximately –0.5 mm behind the crack tip to 3 mm ahead of the crack tip. At both –1 and –2 mm positions, the {00.2} peak intensities in both cases were similar to each other.

Figure 4.21 shows lattice strains and diffraction peak intensities, respectively, plotted chronologically as a function of the applied load [marked with triangles, Fig. 3.4(d)] at the location of 0.5 mm in front of the crack tip, in order to demonstrate clearly

how the measured values change during the test. A schematic of the evolution of microstructure at applied loads marked in Fig. 4.21(b) was presented in Fig. 4.22. In Fig 4.22, G1, G2, and G3 represent three grains with different crystallographic orientations in front of the fatigue crack tip. Among them, the basal plane normal of a grain, G2, is parallel to the loading direction (ND), where twinning and detwinning will occur during the loading and unloading sequence. It is worth noting that the {00.2} diffraction peak intensity in ND shown in Fig. 4.21(b) is normalized by the reference diffraction peak intensity (far away from the crack tip and no fatigue history). After the base-line tensile loading was applied and unloaded, the {00.2} peak intensity reduced due to loading was fully recovered after unloading to P_{min} [A in Fig. 4.21(b)]. Both {00.2} and {10.3} grain orientations revealed small compressive residual strains, although there is an applied tensile load, P_{min}. As the sample was loaded up to 1.3 P_{max} [C in Fig. 4.21(b)], the intensity of the {00.2} peak remained stable starting from P_{min} [A in Fig. 4.21(b)] until the load level reached to 0.6 P_{max} [B in Fig. 4.21(b)], and then decreased gradually. The lattice strains also showed the deviation from linearity at $0.6P_{max}$, where the {00.2} peak intensity starts to decrease. When the sample was unloaded to P_{min} [D in Fig. 4.21(b)] after tensile overloading [C in Fig. 4.21(b)], the {00.2} peak intensity was increased immediately and recovered by about 97%. Slightly larger compressive residual strains were observed in the {00.2} and {10.3} grain orientations after the tensile overloading, as compared with those after the base-line tension [Fig. 4.21(a)].

4.4.2 Discussion

The understanding of results in Figs. 4.20 and 4.21 can be facilitated by a general understanding of the stress evolution near a fatigue crack tip. From our previous modelling and experimental studies of fatigue cracks [140, 179], Fig. 4.23 depicts that the plastic zone resembles a stationary crack at K_{max}, while the unloading from K_{max} to K_{min} leads to a compressive residual stress zone immediately near the crack tip and a tensile stress zone ahead of the crack tip. The plastic wake under K_{min} is also in a compressive stress state. The stress distribution is schematically illustrated in Fig. 4.23(c), showing the complex history in the vicinity of the fatigue tip. It is cautioned that results in Fig. 4.23 are qualitative in nature and are based on the isotropic Mises plasticity model. However, the strong plastic anisotropy in Mg alloys will change the magnitude of the stress fields and the location and extent of the compressive stress zone, but the stress distributions should resemble Fig. 4.23(c) for tests under positive R ratios. We next discuss if a correlation between the macroscopic stress state near a fatigue crack and the twinning/detwinning behavior can be established.

Strain and diffraction-peak intensity fields at K_{max} or $K_{overload:}$ According to Fig. 4.23, at K_{max} (LP1 and LP4) and $K_{overload}$ (LP3), there *exists* a large tensile-stress zone behind and ahead of the crack tip, which agrees with the strain measurements in Fig. 4.20(a). When determining if extension twinning occurs in this tensile stress zone, we also need to pay attention to other stress components, since twinning is generally driven by the resolved shear stress.

The intensity of a diffraction peak changes when the amount of materials satisfied with Bragg diffraction varies. Since the *scattering* volume is constant through the

measurements, and phase transformation does not occur in this material, the change of the intensity could only be explained by the re-orientation of grains. In the magnesium alloy, {10.2}<10.1> extension twinning is commonly observed at room temperature in favourably oriented grains, relative to the loading direction. This twinning mode is easily activated by a tensile stress perpendicular to the basal plane or a compressive stress parallel to the basal plane, by giving rise to an approximate 86.6 ^{o} reorientation of the crystal lattice. Since our material, the AZ31B Mg alloy, has a strong rolling texture in which the basal-plane normal in most of the grains is parallel to ND [Fig. 3.4(c)], the tensile loading in ND (Fig. 1b) would lead to the {10.2} extension twinning, resulting in a decrease in the {00.2} peak intensity. In Fig. 4.20(b), the peak intensity decreased within the regime of about [-1 mm, 2 mm], which agreed with the tensile zone depicted in Fig. 4.23(c). Our recent numerical simulations reveal that a large degree of stress triaxiality exists near the peak normal stress (or equivalently, right in front of the crack tip) at $K_{\max}$ [140, 179]. Such a triaxial stress state does not favor twinning because of the reduced resolved shear stress. This observation also agrees well with the observation in Fig. 4.20(b), e.g., the peak intensity does not vary noticeably in the regime of [0 mm, 1 mm] for LP3.

Development of compressive *stresses and detwinning behavior at* $K_{min:}$ An increase of the {00.2} peak intensity in ND during unloading [Figs. 4.20(b) and 4.21(b)] can be obtained either from the {10.2} extension twining in {10.0} grains under compression or detwinning of the volumes twinned under the tensile loading. As no diffraction peaks of {10.0} in ND and {00.2} in TD are found in the initial texture [see Fig. 3.4(c)], the possible {10.2} extension twining under compression in such {10.0}

grain orientations is negligible. Therefore, it is evident that only the detwinning behavior is responsible for the observed increase of the {00.2} peak intensities in ND during unloading [Figs. 4.20(b) and 4.21(b)].

After the tensile loading [LP2, Fig. 4.20(a)], the compressive stresses were developed near the crack tip, even though the tensile load of 230 N is applied. In an unloaded condition after the tensile overload [LP4, Fig. 4.20(a)], the magnitude of strains both at the crack tip and ahead of the crack tip was decreased, as compared to that at LP1 (the immediately preceding cycle). The reduced strains at LP4 reveal that the overload-induced larger plastic deformation developed larger compressive residual stresses during unloading, which finally results in the enlarged compressive stresses around the crack tip at P_{min} (LP5), relative to LP2. It is thought that the development of compressive residual stresses generated near the crack tip during unloading as a result of plastic deformation is responsible for the detwinning behavior.

Activation of twinning and detwinning near the crack tip, compared to uniaxial loading: The twinning-detwinning phenomena have been reported during the strain-path changes [180] or cyclic loading [44, 45] under monotonic-loading conditions. In the previous studies, the full recovery of the twinned volume is usually obtained when reverse loading is applied. However, our crack-tip deformation study demonstrates that the twinned volume is fully detwinned even at $0.3P_{max}$ during unloading after the base-line tensile loading, and approximately 97% of twinned volume is detwinned after unloading to P_{min} in the overload cycle, even though no reverse loading is applied [Figs. 4.21(b) and 4.22]. Moreover, it should be pointed out that while twinning is activated above a certain critical stress value ($0.6P_{max}$ in this study), detwinning occurs

immediately upon unloading. The activation of the detwinning behavior during unloading is attributed to the compressive residual stresses developed near the crack tip immediately after plastic deformation.

It is interesting to estimate the activation stress of extension twinning based on our experimentally-determined lattice strain measurements. In the previous research [43, 46, 87], it has been acknowledged that the Schmid law, as shown below, could be applied to calculate the onset of the deformation twinning by assuming that the deformation twinning is governed by CRSS on the twin plane and in the twinning direction under the uniaxial loading condition.

$$\tau_{CRSS} = \sigma_c \cos\lambda \cos\chi \tag{22}$$

where τ_{CRSS} is the CRSS, σ_c is the critical applied stress, λ and χ are the angles between the loading axis and twin plane normal and between the loading axis and the twinning direction, respectively. In the present study, the internal strain of the {00.2} orientation grains in the ND direction could be used to calculate the activation stress for extension twinning. Since this point of interest is slightly ahead of the fatigue crack tip but within the plastic zone at $K_{\max}$, the stress state is roughly $\sigma_{11} \approx \sigma_{33} \approx 0.5\sigma_{22}$. From the Fig. 4.21(a), the lattice strain of the {00.2} orientation grains corresponding to $0.6P_{\max}$ equals 730 με. Such a strain, $\varepsilon_{22}^{elastic}$, together with the elastic constants leads to stress levels of about σ_{22} = 50 MPa and σ_{11} = σ_{33} = 25 MPa, which are approximately equivalent to a uniaxial tension of 25 MPa plus a hydrostatic tension of 25 MPa. Since a hydrostatic part does not lead to any resolved shear stress, the CRSS of 12.5 MPa is obtained by a product of the critical applied stress (σ_c = 25 MPa) and a Schmid factor ($\cos\lambda\cos\chi$) of ~0.5 under

the uniaxial test condition. Although the stress state is very approximate, this value agrees very well with previous studies giving CRSS of 15 MPa [16,17].

As shown in Fig. 4.21(a), it is noted that both {00.2} and {10.3} grain orientations, favourably oriented for extension twinning, reveal compressive residual strains at P_{min} after unloading. The compressive residual strains in those grain orientations result from the stress relaxation due to the activation of extension twinning, which is typically observed in "soft" grain orientation, where the grains are plastically deformed. Once the extension twinning occurs, internal stresses of the grains experiencing the twinning are relaxed and transfer the load to the other "hard" grain orientations, i.e., the new twins [17]. Thus, it is thought that the load re-distribution phenomenon, caused by the development of intergranular stresses in polycrystal aggregates, influenced the compressive residual stresses in {00.2} and {10.3} grain orientations after unloading.

Texture evolution with the crack propagation: Since the initial texture of the studied alloy has the twinning–detwinning dominant deformation mechanism, it is expected that only a small amount of residual twins remain in the plastic zone. It is interesting to examine how many residual twins are left as the crack propagates. Figure 4.20(b) shows neutron-diffraction peak-intensity variations as a function of the distance from the crack tip. It should be noted that the different locations away from the crack tip represent a different fatigue history, and the diffraction peak intensities at the various locations could be related to the amount of residual twins. For example, the materials at the location of 2 mm behind the crack tip (–2 mm) were subjected to cyclic loading experiencing the elastic deformation, plastic deformation, final fracture, and further deformation after fracture until the stresses are not applied, as the crack approaches and

propagates through this position. The {00.2} peak intensity at the –2 mm location [LP2, Fig. 4.20(b)] decreased by about 11%, as compared to that at the 3 mm location where the elastic and small plastic deformation occurred. It means that most of the twinned volumes are detwinned during unloading, but approximately 11% of grains contributing to the initial {00.2} peak intensity remained as residual twins. In order to confirm the results of the in-situ neutron-diffraction measurements, more quantitative texture analyses were performed by measuring the bulk texture on the same DC(T) specimen used for in-situ test (Fig. 4.24). Noting that a decrease of the {00.2} diffraction peak in ND during tensile loading is caused by the activities of {10.2} extension twinning, the volume fraction of extension twins can be obtained from a decrease in the volume fraction of grains where extension twinning is expected. Since the grains present near the center of the {00.2} pole figure would undergo the extension twinning, the volume fraction of the grains experiencing twinning is calculated by integrating the normalized intensity from center to the inner rim (e.g. χ = 0 to χ = 30) in the {00.2} pole figure. Thus, the twinned volume fraction was estimated in Fig. 4.25 from the comparison of the volume fraction of grains within the rim. A similar approach has been recently employed [60, 181].

Figure 4.24 shows the several pole figures measured at locations far away from the crack tip [Fig. 4.24(a)], right ahead of the crack tip [Fig. 4.24(b)], and behind the crack tip [Fig. 4.24(c)]. It was found that the texture in the fatigue-wake region [Fig. 4.24(c)] did not change significantly, compared to that in the undeformed region far away from the crack tip [Fig. 4.24(a)]. Furthermore, the volume fraction analysis revealed that the volume fraction of the residual twins in the fatigue-wake region was in the range of 7 to 14% (Fig. 7), which was in a good agreement with that from in-situ neutron-diffraction

measurement. The texture measurement results confirm that most of the twinned materials undergo detwinning during unloading under the current fatigue loading condition. Therefore, it is concluded that reversible twinning and detwinning characteristics are the dominant deformation mechanism for the studied material subjected to cyclic loading, and only a small amount of residual twins remain after the crack propagation.

4.4.2 Summary

In-situ neutron-diffraction experiments were carried out to investigate the twinning-detwinning behavior during fatigue-crack propagation in a wrought magnesium alloy, AZ31B, disk-shaped compact-tension specimen. The main results are summarized as follows:

(1) During the base-line tensile loading and unloading, reversible twinning and detwinning were observed at 0.5 mm in front of the crack tip, such that the volume twinned during tensile loading was completely detwinned during unloading. On the other hand, the recovery of the {00.2} peak intensity by almost 97% during unloading, followed by tensile overloading, indicated that a very small amount of residual twins remained after the tensile overload.

(2) While twinning was activated above a certain critical stress value ($0.6P_{max}$ in the current study), detwinning occurred immediately at the beginning of unloading and continued during this process. The development of compressive residual stresses generated near the crack tip during unloading is thought of as being responsible for the detwinning behavior.

(3) When the extension twinning occurs, internal strains in the {00.2} and {10.3} grains experiencing the extension twinning were relaxed, which developed the compressive residual stresses after unloading.

(4) Neutron-diffraction texture-measurement results show that the texture in the fatigue-wake region did not change much, compared to that in the undeformed region far away from the crack tip, and approximately 11% of residual twins were left behind the crack tip. The results reveal that the reversible twinning and detwinning are the dominant deformation mechanism for the studied material subjected to cyclic loading, and only a small amount of residual twins remain after the crack propagation.

CHAPTER 5
CONCLUSIONS AND RECOMMENDATIONS

The real-time in-situ neutron diffraction technique under a continuous loading condition and numerical simulations using the EVPSC-TDT model were employed to study the plastic-deformation dynamics on twinning and detwinning behavior of the wrought AZ31B Mg alloy. The twinning and detwinning behavior in an individual grain inside polycrystalline Mg alloy was investigated using in-situ synchrotron X-ray microdiffraction. The fully-reversed low-cycle fatigue behavior of a HCP-structured Mg alloy was characterized by real-time in-situ neutron diffraction measurements. The fatigue crack growth behavior was also studied using in-situ neutron diffraction method. The following conclusions can be drawn based on the present research:

(1) The plastic deformation can be divided into several stages during strain path changes and in each low-cycle fatigue cycle, based on the work-hardening-rate variations. In each stage, a certain deformation mode becomes dominant, which is characterized by real-time in-situ neutron diffraction and supported by simulation results.

(2) No apparent detwinning activities were observed in unloading during strain path changes and low-cycle fatigue. Detwinning did not occur until reverse tension. While, in the fatigue crack propagation experiments, detwinning occurred immediately at the beginning of unloading and continued during this process, which results from the development of

compressive residual stresses generated near the crack tip during unloading.

(3) An obvious strengthening behavior was obtained during compression by pre-tension. However, the pre-deformation has limited impacts on mechanical behavior during the reverse tension.

(4) The residual strain is responsible for the delay of the onset of tensile twinning in the subsequent compression in the pre-deformed sample. However, by increasing the dislocation density through pre-tension, the twinning and detwinning process can be accelerated, once the twinning or detwinning process was activated.

(5) In the pre-deformed sample, grain rotation is thought to account for the diffraction peak intensity decrease in (00.2) twin grains in the elastic deformation region during the reverse tension, since no simultaneous diffraction peak intensity changes in (10.0) grains was detected.

(6) The EVPSC-TDT model was employed for the first time to predict the deformation dynamics under a continuous-loading condition during strain-path changes in a HCP-structured Mg alloy. The simulation results concur with the experimental observation of the alternate deformation mechanisms during the strain-path changes.

(7) The tensile twinning and detwinning process have been observed in an individual grain for a HCP structured Mg alloy using synchrotron X-ray

microdiffraction during in-situ compression and reverse tension, respectively, along RD.

(8) The operation of detwinning process was through the migration of twin boundaries into the twins via the glide of the twinning dislocations.

(9) The distinct d-spacing decrease in a parent grain can be observed on two sides of twin during twinning dominated deformation, but no d-spacing variation was detected during detwinning dominated deformation.

(10) The asymmetry shape of stress-strain hysteresis loop during low-cycle fatigue results from the rapid strain hardening in the transition region, from detwinning to dislocation dominated deformation, during compression, although the area of stress-strain hysteresis loop on tension and compression sides essentially equal to each other.

(11) The fatigue resistance and fatigue life of HCP-structured wrought Mg alloys depends on the initial texture of the fatigue samples. The compressive mean stress is not necessary for the better fatigue resistance and longer fatigue life in wrought Mg alloys during fully-reversed low-cycle fatigue.

(12) With the increase of fatigue cycles, more and more grains involve in twinning and detwinning. The activation of tensile twinning is much more difficult in the fatigued sample than in the un-deformed sample, due to the residual strain. In the whole fatigue life, the activation of detwinning dominated deformation is easier than twinning dominated deformation.

(13) In the elastic region, there is no obvious twinning and detwinning activities. The twinning and detwinning dominated deformation modes occurred in plastic deformation regions in every fatigue cycle.

(14) The residual twins appear at early fatigue life, and being responsible for the hardening behavior in the twinning dominated deformation.

(15) The shape and the area of stress-lattice strain of (00.2) grains hysteresis loop stay asymmetric in the whole fatigue. The evolution of the maximum value of the lattice strain in the (00.2) grain in the axial direction is sensitive to the appearance of the residual twins.

(16) In the 1^{st} tension in the 1^{st} fatigue cycle, the lattice strain of (00.2) grains in the axial direction yield rapidly in twinning dominated deformation. In the following fatigue cycles, during compression, the lattice strain of (00.2) grains tends to relax in detwinning dominated deformation, and carry more load in the transition region. During tension, the zigzag shape of the lattice strain variation in (00.2) grains is observed during twinning dominated deformation.

(17) During the base-line tensile loading and unloading, reversible twinning and detwinning were observed at 0.5 mm in front of the crack tip, such that the volume twinned during tensile loading was completely detwinned during unloading. On the other hand, the recovery of the {00.2} peak intensity by almost 97% during unloading, followed by tensile overloading, indicated that a very small amount of residual twins remained after the tensile overload.

(18) When the extension twinning occurs, internal strains in the {00.2} and {10.3} grains experiencing the extension twinning were relaxed, which developed the compressive residual stresses after unloading.

(19) Neutron-diffraction texture-measurement results show that the texture in the fatigue-wake region did not change much, compared to that in the undeformed region far away from the crack tip, and approximately 11% of residual twins were left behind the crack tip. The results reveal that the reversible twinning and detwinning are the dominant deformation mechanism for the studied material subjected to cyclic loading, and only a small amount of residual twins remain after the crack propagation.

(20) Future work: (1) Effects of precipitates on plastic deformation, such as twinning and detwinning behavior, and fatigue-crack growth characteristics for novel precipitation-hardenable wrought Mg alloys have been rarely reported. The precipitates shape, inter-precipitates distance, and the precipitate volume fraction changes under different loading conditions can be characterized, using small-angle neutron scattering (SANS) at SNS and/or small angle X-ray scattering (SAXS) at APS. (2) Nearly all of the low-cycle fatigue studies were performed under fully-reversed conditions. The low-cycle fatigue mechanisms under the asymmetry loading still remain unclear. The real-time in-situ neutron diffraction at VULCAN, SNS, ORNL can be used for such a topic. (3) The twinning-detwinnning behavior under biaxial and/or triaxial loading conditions are not fully explored.

LIST OF REFERENCES

[1] Aghion E, Bronfin B. Magnesium alloys development towards the 21(st) century. In: Kojima Y, Aizawa T, Kamado S, editors. Magnesium Alloys 2000, vol. 350-3. Zurich-Uetikon: Trans Tech Publications Ltd, 2000. p.19.
[2] Mordike BL, Ebert T. Magnesium - Properties - Applications - Potential. Mat Sci Eng a-Struct 2001;302:37.
[3] Luo A. Recent magnesium alloy development for elevated temperature applications. International Materials Reviews 2004:13.
[4] Polmear IJ. Magnesium alloys and applications. Mater. Sci. Technol. 1994;10:1.
[5] Schumann S, Friedrich H. Current and future use of magnesium in the automobile industry. Magnesium Alloys 2003, Pts 1 and 2 2003:51.
[6] Rosen GI, Segal G, Lubinsky A. Large profile magnesium alloys extrusions for automotive applications. Magnesium - Science, Technology and Applications 2005;488-489:509.
[7] Doldon R. The Fatigue Behaviour of Magnesium-Zirconium and Magnesium-Aluminum Canning Materials. Journal of Nuclear Materials 1963;8:169.
[8] Chen LJ, Wang CY, Wu W, Liu Z, Stoica GM, Wu L, Liaw PK. Low-cycle fatigue behavior of an as-extruded AM50 magnesium alloy. Metall. Mater. Trans. A-Phys. Metall. Mater. Sci. 2007;38A:2235.
[9] Doege E, Droder K. Sheet metal forming of magnesium wrought alloys - formability and process technology. Journal of Materials Processing Technology 2001;115:14.
[10] Park SC, Lim JD, Eliezer D, Shin KW. Microstructure and mechanical properties of Mg-Zn-Ag alloys. In: Kojima Y, Aizawa T, Higashi K, Kamado S, editors. Magnesium Alloys 2003, Pts 1 and 2, vol. 419-4. Zurich-Uetikon: Trans Tech Publications Ltd, 2003. p.159.
[11] Shih TS, Liu WS, Chen YJ. Fatigue of as-extruded AZ61A magnesium alloy. Mat Sci Eng a-Struct 2002;325:152.
[12] Chen LJ, Shen J, Wu W, Li F, Wang Y, Liu Z. Low-cycle fatigue behavior of magnesium alloy AZ91. Magnesium - Science, Technology and Applications 2005;488-489:725.
[13] Schumann S. The paths and strategies for increased magnesium applications in vehicles. Magnesium - Science, Technology and Applications 2005;488-489:1.
[14] Li RG, Nie JF, Huang GJ, Xin YC, Liu Q. Development of high-strength magnesium alloys via combined processes of extrusion, rolling and ageing. Scripta Mater 2011;64:950.
[15] Sasaki TT, Ju JD, Hono K, Shin KS. Heat-treatable Mg-Sn-Zn wrought alloy. Scripta Mater 2009;61:80.
[16] Mendis CL, Oh-ishi K, Hono K. Enhanced age hardening in a Mg-2.4 at.% Zn alloy by trace additions of Ag and Ca. Scripta Mater 2007;57:485.
[17] Sasaki TT, Oh-ishi K, Ohkubo T, Hono K. Enhanced age hardening response by the addition of Zn in Mg-Sn alloys. Scripta Mater 2006;55:251.
[18] Agnew S. Wrought magnesium: A 21st century outlook. Jom 2004:20.
[19] Ritchie RO. The conflicts between strength and toughness. Nature Materials 2011;10:817.
[20] Suresh S. Fatigue of materials. Cambridge: Cambridge University Press, 1998.

[21] Cazacu O, Barlat F. A criterion for description of anisotropy and yield differential effects in pressure-insensitive metals. Int. J. Plast. 2004;20:2027.
[22] Ogarevic VV, Stephens RI. Fatigue of Magnesium Alloys. Annu Rev Mater Sci 1990;20:141.
[23] Wu L, Stoica GM, Liao HH, Agnew SR, Payzant EA, Wang GY, Fielden DE, Chen L, Liaw PK. Fatigue-property enhancement of magnesium alloy, AZ31B, through equal-channel-angular pressing. Metall Mater Trans A 2007;38A:2283.
[24] Yang F, Yin SM, Li SX, Zhang ZF. Crack initiation mechanism of extruded AZ31 magnesium alloy in the very high cycle fatigue regime. Mat Sci Eng a-Struct 2008;491:131.
[25] Jiang L, Jonas JJ, Luo AA, Sachdev AK, Godet S. Twinning-induced softening in polycrystalline AM30 Mg alloy at moderate temperatures. Scripta Mater 2006;54:771.
[26] Barnett MR, Nave MD, Bettles CJ. Deformation microstructures and textures of some cold rolled Mg alloys. Mat Sci Eng a-Struct 2004;386:205.
[27] Nave MD, Barnett MR. Microstructures and textures of pure magnesium deformed in plane-strain compression. Scripta Mater 2004;51:881.
[28] Jiang L, Jonas JJ, Mishra RK, Luo AA, Sachdev AK, Godet S. Twinning and texture development in two Mg alloys subjected to loading along three different strain paths. Acta Mater 2007;55:3899.
[29] Wang XS, Liang F, Fan JH, Zhang FH. Low-cycle fatigue small crack initiation and propagation behaviour of cast magnesium alloys based on in-situ SEM observations. Philos Mag 2006;86:1581.
[30] Yin DL, Zhang KF, Wang GF, Han WB. Warm deformation behavior of hot-rolled AZ31 Mg alloy. Mat Sci Eng a-Struct 2005;392:320.
[31] Honma T, Ohkubo T, Hono K, Kamado S. Chemistry of nanoscale precipitates in Mg-2.1Gd-0.6Y-0.2Zr (at.%) alloy investigated by the atom probe technique. Mat Sci Eng a-Struct 2005;395:301.
[32] Antion C, Donnadieu P, Perrard F, Deschamps A, Tassin C, Pisch A. Hardening precipitation in a Mg-4Y-3RE alloy. Acta Mater 2003;51:5335.
[33] Wu LY, Yang Z, He E, Zhang LZ, Chen ZH, Yang L. The tensile properties at 448 K and the fracture behaviors under in situ transmission electron microscope strain for the Mg-6.0Gd-1.2Zn-0.15Y alloy. Mater Design 2012;40:199.
[34] Yu Q, Qi L, Chen K, Mishra RK, Li J, Minor AM. The Nanostructured Origin of Deformation Twinning. Nano Lett. 2012;12:887.
[35] Yang HJ, Yin SM, Huang CX, Zhang ZF, Wu SD, Li SX, Liu YD. EBSD Study on Deformation Twinning in AZ31 Magnesium Alloy During Quasi-in-Situ Compression. Advanced Engineering Materials 2008;10:955.
[36] Jain J, Zou J, Sinclair CW, Poole WJ. Double tensile twinning in a Mg-8Al-0.5Zn alloy. J Microsc-Oxford 2011;242:26.
[37] Beyerlein IJ, Wang J, Barnett MR, Tome CN. Double twinning mechanisms in magnesium alloys via dissociation of lattice dislocations. P R Soc A 2012;468:1496.

[38] An K, Skorpenske HD, Stoica AD, Ma D, Wang XL, Cakmak E. First In Situ Lattice Strains Measurements Under Load at VULCAN. Metall Mater Trans A 2011;42A:95.
[39] Liaw PK, Choo H, Buchanan RA, Hubbard CR, Wang XL. Development of an in situ neutron-scattering facility for research and education in the mechanical behavior of materials. Mat Sci Eng a-Struct 2006;437:126.
[40] Barnett MR. Twinning and the ductility of magnesium alloys Part II. "Contraction" twins. Mater. Sci. Eng. A-Struct. Mater. Prop. Microstruct. Process. 2007;464:8.
[41] Larson BC, Yang W, Ice GE, Budai JD, Tischler JZ. Three-dimensional X-ray structural microscopy with submicrometre resolution. Nature 2002;415:887.
[42] Barabash R, Gao YF, Sun YN, Lee SY, Choo H, Liaw PK, Brown DW, Ice GE. Neutron and X-ray diffraction studies and cohesive interface model of the fatigue crack deformation behavior. Phil Mag Lett 2008;88:553.
[43] Wu L, Agnew SR, Brown DW, Stoica GM, Clausen B, Jain A, Fielden DE, Liaw PK. Internal stress relaxation and load redistribution during the twinning-detwinning-dominated cyclic deformation of a wrought magnesium alloy, ZK60A. Acta Mater. 2008;56:3699.
[44] Wu L, Agnew SR, Ren Y, Brown DW, Clausen B, Stoica GM, Wenk HR, Liaw PK. The effects of texture and extension twinning on the low-cycle fatigue behavior of a rolled magnesium alloy, AZ31B. Mater. Sci. Eng. A-Struct. Mater. Prop. Microstruct. Process. 2010;527:7057.
[45] Wu L, Jain A, Brown DW, Stoica GM, Agnew SR, Clausen B, Fielden DE, Liaw PK. Twinning-detwinning behavior during the strain-controlled low-cycle fatigue testing of a wrought magnesium alloy, ZK60A. Acta Mater. 2008;56:688.
[46] Agnew SR, Tome CN, Brown DW, Holden TM, Vogel SC. Study of slip mechanisms in a magnesium alloy by neutron diffraction and modeling. Scr. Mater. 2003;48:1003.
[47] Brown DW, Agnew SR, Bourke MAM, Holden TM, Vogel SC, Tome CN. Internal strain and texture evolution during deformation twinning in magnesium. Mater. Sci. Eng. A-Struct. Mater. Prop. Microstruct. Process. 2005;399:1.
[48] Agnew SR, Brown DW, Vogel SC, Holden TM. In-situ measurement of internal strain evolution during deformation dominated by mechanical twinning. Ecrs 6: Proceedings of the 6th European Conference on Residual Stresses 2002;404-7:747.
[49] King A, Ludwig W, Herbig M, Buffiere JY, Khan AA, Stevens N, Marrow TJ. Three-dimensional in situ observations of short fatigue crack growth in magnesium. Acta Mater 2011;59:6761.
[50] Woo W, Choo H, Brown DW, Liaw PK, Feng Z. Texture variation and its influence on the tensile behavior of a friction-stir processed magnesium alloy. Scripta Mater 2006;54:1859.
[51] Agnew SR, Duygulu O. Plastic anisotropy and the role of non-basal slip in magnesium alloy AZ31B. Int. J. Plast. 2005;21:1161.
[52] Lou XY, Li M, Boger RK, Agnew SR, Wagoner RH. Hardening evolution of AZ31B Mg sheet. Int. J. Plast. 2007;23:44.

[53] Choi SH, Kim DH, Lee HW, Seong BS, Piao K, Wagoner R. Evolution of the deformation texture and yield locus shape in an AZ31 Mg alloy sheet under uniaxial loading. Mater. Sci. Eng. A-Struct. Mater. Prop. Microstruct. Process. 2009;526:38.
[54] Agnew SR, Yoo MH, Tome CN. Application of texture simulation to understanding mechanical behavior of Mg and solid solution alloys containing Li or Y. Acta Mater. 2001;49:4277.
[55] Brown D, Agnew S, Abeln S, Blumenthal W, Bourke M, Mataya M, Tome C, Vogel S. The role of texture, temperature, and strain rate in the activity of deformation twinning. Mater Sci Forum 2005:1037.
[56] Brown DW, Almer JD, Clausen B, Mosbrucker PL, Sisneros TA, Vogel SC. Twinning and de-twinning in beryllium during strain path changes. Materials Science and Engineering: A 2013;559:29.
[57] Agnew S, Brown D, Vogel S, Holden T. In-situ measurement of internal strain evolution during deformation dominated by mechanical twinning. Ecrs 6: Proceedings of the 6th European Conference on Residual Stresses 2002:747.
[58] Christian JW, Mahajan S. Deformation Twinning. Prog Mater Sci 1995;39:1.
[59] Barnett MR. Twinning and the ductility of magnesium alloys Part I: "Tension" twins. Mater. Sci. Eng. A-Struct. Mater. Prop. Microstruct. Process. 2007;464:1.
[60] Proust G, Tome CN, Jain A, Agnew SR. Modeling the effect of twinning and detwinning during strain-path changes of magnesium alloy AZ31. Int. J. Plast. 2009;25:861.
[61] Dudamell NV, Ulacia I, Galvez F, Yi S, Bohlen J, Letzig D, Hurtado I, Perez-Prado MT. Twinning and grain subdivision during dynamic deformation of a Mg AZ31 sheet alloy at room temperature. Acta Mater. 2011;59:6949.
[62] Wu L. Mechanical Behavior and the Role of Deformation Twinning in Wrought Magnesium Alloys Investigated Using Neutron and Synchrotron X-ray Diffraction. In: Materials Science and Engineering, vol. Ph.D. Knoxville: The University of Tennessee, 2009.
[63] Ando D, Koike J, Sutou Y. Relationship between deformation twinning and surface step formation in AZ31 magnesium alloys. Acta Mater 2010;58:4316.
[64] Wang J, Beyerlein IJ, Hirth JP. Nucleation of elementary {(1)over-bar 0 1 1} and {(1)over-bar 0 1 3} twinning dislocations at a twin boundary in hexagonal close-packed crystals. Model Simul Mater Sc 2012;20.
[65] Wu BL, Zhang YD, Wan G, Humbert M, Wagner F, Esling C. Primary twinning selection with respect to orientation of deformed grains in ultra-rapidly compressed AZ31 alloy. Mat Sci Eng a-Struct 2012;541:120.
[66] Mu SJ, Jonas JJ, Gottstein G. Variant selection of primary, secondary and tertiary twins in a deformed Mg alloy. Acta Mater 2012;60:2043.
[67] Yoo MH, Lee JK. Deformation Twinning in Hcp Metals and Alloys. Philos Mag A 1991;63:987.
[68] Gray GT. Deformation Twinning in Al-4.8 Wt-Percent Mg. Acta Metallurgica 1988;36:1745.
[69] Chun JS, Byrne JG, Borneman.A. Inhibition of Deformation Twinning by Precipitates in a Magnesium-Zinc Alloy. Philos Mag 1969;20:291.

[70] Hull D. Effect of Grain Size and Temperature on Slip, Twinning and Fracture in 3-Percent Silicon Iron. Acta Metallurgica 1961;9:191.
[71] Li M. CONSTITUTIVE MODELING OF SLIP, TWINNING, AND UNTWINNING IN AZ31B MAGNESIUM. In: Materials Science and Engineering, vol. Ph.D. Columbus: The Ohio State University, 2006.
[72] Altshule.Tl, Christia.Jw. Low Temperature Twinning in Pure Iron. Acta Metallurgica 1966;14:903.
[73] Boucher NA, Christian JW. The influence of pre-strain on deformation twinning in niobium single crystals. Acta Metallurgica 1972;20:581.
[74] Marcinkowski MJ, Lipsitt HA. The plastic deformation of chromium at low temperatures. Acta Metallurgica 1962;10:95.
[75] Bohlen J, Nurnberg MR, Senn JW, Letzig D, Agnew SR. The texture and anisotropy of magnesium-zinc-rare earth alloy sheets. Acta Mater 2007;55:2101.
[76] Wu BL, Wan G, Zhang YD, Esling C. Twinning characteristics in textured AZ31 alloy under impact loading along specified direction. Mater Lett 2010;64:636.
[77] Ishihara S, Nan Z, Goshirna T. Effect of microstructure on fatigue behavior of AZ31 magnesium alloy. Mater. Sci. Eng. A-Struct. Mater. Prop. Microstruct. Process. 2007;468:214.
[78] Kim HK, Lee YI, Chung CS. Fatigue properties of a fine-grained magnesium alloy produced by equal channel angular pressing. Scripta Mater 2005;52:473.
[79] Jain A, Duygulu O, Brown D, Tome C, Agnew S. Grain size effects on the tensile properties and deformation mechanisms of a magnesium alloy, AZ31B, sheet. Mat Sci Eng a-Struct 2008:545.
[80] Muransky O, Barnett MR, Carr DG, Vogel SC, Oliver EC. Investigation of deformation twinning in a fine-grained and coarse-grained ZM20 Mg alloy: Combined in situ neutron diffraction and acoustic emission. Acta Mater. 2010;58:1503.
[81] Muransky O, Carr DG, Sittner P, Oliver EC. In situ neutron diffraction investigation of deformation twinning and pseudoelastic-like behaviour of extruded AZ31 magnesium alloy. Int. J. Plast. 2009;25:1107.
[82] Muranskya O, Carr DG, Barnett MR, Oliver EC, Sittner P. Investigation of deformation mechanisms involved in the plasticity of AZ31 Mg alloy: In situ neutron diffraction and EPSC modelling. Mater. Sci. Eng. A-Struct. Mater. Prop. Microstruct. Process. 2008;496:14.
[83] Hao H, Maijer D, Rogge R. Investigation of residual strains by neutron diffraction in an AZ31 direct chill cast billet. Ndt&E Int 2009;42:704.
[84] Woo W, Choo H, Prime MB, Feng Z, Clausen B. Microstructure, texture and residual stress in a friction-stir-processed AZ31B magnesium alloy. Acta Mater. 2008;56:1701.
[85] Clausen B, Tome CN, Brown DW, Agnew SR. Reorientation and stress relaxation due to twinning: Modeling and experimental characterization for Mg. Acta Mater. 2008;56:2456.
[86] Davies CHJ, Yi S, Bohlen J, Kainer KU, Brokmeier HG. Synchrotron radiation investigation of twinning in extruded magnesium alloy AZ31. Mater Sci Forum 2005;495-497:1633.

[87] Gharghouri MA, Weatherly GC, Embury JD, Root J. Study of the mechanical properties of Mg-7.7at.% Al by in-situ neutron diffraction. Philos Mag A 1999;79:1671.
[88] Renner F, Zenner H. Fatigue strength of die-cast magnesium components. Fatigue Fract Eng M 2002;25:1157.
[89] Lee SG, Patel GR, Gokhale AM. Inverse surface macro-segregation in high-pressure die-cast AM60 magnesium alloy and its effects on fatigue behavior. Scripta Mater 2005;52:1063.
[90] Mayer H, Papakyriacou M, Zettl B, Stanzl-Tschegg SE. Influence of porosity on the fatigue limit of die cast magnesium and aluminium alloys. Int J Fatigue 2003;25:245.
[91] Horstemeyer MF, Yang N, Gall K, McDowell D, Fan J, Gullett P. High cycle fatigue mechanics in a cast AM60B magnesium alloy. Fatigue Fract Eng M 2002;25:1045.
[92] Potzies C, Kainer KU. Fatigue of magnesium alloys. Adv. Eng. Mater. 2004;6:281.
[93] Park SH, Hong SG, Lee BH, Bang W, Lee CS. Low-cycle fatigue characteristics of rolled Mg-3Al-1Zn alloy. Int. J. Fatigue 2010;32:1835.
[94] Begum S, Chen DL, Xu S, Luo AA. Low cycle fatigue properties of an extruded AZ31 magnesium alloy. Int. J. Fatigue 2009;31:726.
[95] Begum S, Chen DL, Xu S, Luo AA. Strain-Controlled Low-Cycle Fatigue Properties of a Newly Developed Extruded Magnesium Alloy. Metall. Mater. Trans. A-Phys. Metall. Mater. Sci. 2008;39A:3014.
[96] Kwon S, Song K, Shin KS, Kwun SI. Low cycle fatigue properties and cyclic deformation behavior of as-extruded AZ31 magnesium alloy. Trans. Nonferrous Met. Soc. China 2010;20:S533.
[97] Lin XZ, Chen DL. Strain controlled cyclic deformation behavior of an extruded magnesium alloy. Mater. Sci. Eng. A-Struct. Mater. Prop. Microstruct. Process. 2008;496:106.
[98] Li QZ, Yu Q, Zhang JX, Jiang YY. Effect of strain amplitude on tension-compression fatigue behavior of extruded Mg6Al1ZnA magnesium alloy. Scr. Mater. 2010;62:778.
[99] Chen C, Liu TM, Lv CL, Lu LW, Luo DZ. Study on cyclic deformation behavior of extruded Mg-3Al-1Zn alloy. Mater. Sci. Eng. A-Struct. Mater. Prop. Microstruct. Process. 2012;539:223.
[100] Lv F, Yang F, Li SX, Zhang ZF. Effects of hysteresis energy and mean stress on low-cycle fatigue behaviors of an extruded magnesium alloy. Scr. Mater. 2011;65:53.
[101] Zhang J, Yu Q, Jiang Y, Li Q. An experimental study of cyclic deformation of extruded AZ61A magnesium alloy. International Journal of Plasticity 2011;27:768.
[102] Yu Q, Zhang J, Jiang Y, Li Q. Effect of strain ratio on cyclic deformation and fatigue of extruded AZ61A magnesium alloy. Int. J. Fatigue 2012;44:225.

[103] Begum S, Chen DL, Xu S, Luo AA. Effect of strain ratio and strain rate on low cycle fatigue behavior of AZ31 wrought magnesium alloy. Mater. Sci. Eng. A-Struct. Mater. Prop. Microstruct. Process. 2009;517:334.
[104] Li Q, Yu Q, Zhang J, Jiang Y. Microstructure and deformation mechanism of Mg6Al1ZnA alloy experienced tension–compression cyclic loading. Scr. Mater. 2011;64:233.
[105] Guillemer C, Clavel M, Cailletaud G. Cyclic behavior of extruded magnesium: Experimental, microstructural and numerical approach. Int. J. Plast. 2011;27:2068.
[106] Tsushida M, Shikada K, Kitahara H, Ando S, Tonda H. Relationship between fatigue strength and grain size in AZ31 magnesium alloys. Mater. Trans. 2008;49:1157.
[107] Liu WC, Wu GH, Zhai CQ, Ding WJ, Korsunsky AM. Grain refinement and fatigue strengthening mechanisms in as-extruded Mg-6Zn-0.5Zr and Mg-10Gd-3Y-0.5Zr magnesium alloys by shot peening. Int. J. Plast. 2013;49:16.
[108] Yin SM, Li SX. Low-cycle Fatigue Behaviors of an As-extruded Mg-12%Gd-3%Y-0.5%Zr Alloy. J. Mater. Sci. Technol. 2013;29:775.
[109] Mirza FA, Chen DL, Li DJ, Zeng XQ. Low cycle fatigue of a rare-earth containing extruded magnesium alloy. Mater. Sci. Eng. A-Struct. Mater. Prop. Microstruct. Process. 2013;575:65.
[110] Wu LY, Yang Z, Xia WJ, Chen ZH, Yang L. The cyclic softening and evolution of microstructures for Mg-10Gd-2.0Y-0.46Zr alloy under low cycle fatigue at 573 K. Mater. Des. 2012;36:47.
[111] Zhu R, Ji WQ, Wu YJ, Cai XT, Yu Y. Effect of aging treatment on low-cycle fatigue behavior of extruded Mg-8Al-0.5Zn alloys. Mater. Des. 2012;41:203.
[112] Gall K, Biallas G, Maier HJ, Gullett P, Horstemeyer MF, McDowell DL, Fan JH. In-situ observations of high cycle fatigue mechanisms in cast AM60B magnesium in vacuum and water vapor environments. Int. J. Fatigue 2004;26:59.
[113] Sajuri ZB, Miyashita Y, Mutoh Y. Effects of humidity and temperature on the fatigue behaviour of an extruded AZ61 magnesium alloy. Fatigue Fract. Eng. Mater. Struct. 2005;28:373.
[114] Bhuiyan MS, Mutoh Y, Murai T, Iwakami S. Corrosion fatigue behavior of extruded magnesium alloy AZ61 under three different corrosive environments. Int. J. Fatigue 2008;30:1756.
[115] Jordon JB, Brown HR, El Kadiri H, Kistler HM, Lett RL, Baird JC, Luo AA. Investigation of fatigue anisotropy in an extruded magnesium alloy. Int. J. Fatigue 2013;51:8.
[116] Lv F, Yang F, Duan QQ, Yang YS, Wu SD, Li SX, Zhang ZF. Fatigue properties of rolled magnesium alloy (AZ31) sheet: Influence of specimen orientation. Int. J. Fatigue 2011;33:672.
[117] Wu YJ, Zhu R, Wang JT, Ji WQ. Role of twinning and slip in cyclic deformation of extruded Mg-3%Al-1%Zn alloys. Scr. Mater. 2010;63:1077.
[118] Park SH, Hong SG, Bang W, Lee CS. Effect of anisotropy on the low-cycle fatigue behavior of rolled AZ31 magnesium alloy. Mater. Sci. Eng. A-Struct. Mater. Prop. Microstruct. Process. 2010;527:417.

[119] Wang H, Wu PD, Wang J, Tome CN. A crystal plasticity model for hexagonal close packed (HCP) crystals including twinning and de-twinning mechanisms. Int. J. Plast. 2013;49:36.
[120] Wang H, Wu PD, Wang J. Modeling inelastic behavior of magnesium alloys during cyclic loading-unloading. Int. J. Plast. 2013;47:49.
[121] Shi BD, Mosler J. On the macroscopic description of yield surface evolution by means of distortional hardening models: Application to magnesium. Int. J. Plast. 2013;44:1.
[122] Ostapovets A, Seda P, Jager A, Lejcek P. New misorientation scheme for a visco-plastic self-consistent model: Equal channel angular pressing of magnesium single crystals. Int. J. Plast. 2012;29:1.
[123] Mayama T, Noda M, Chiba R, Kuroda M. Crystal plasticity analysis of texture development in magnesium alloy during extrusion. Int. J. Plast. 2011;27:1916.
[124] Homayonifar M, Mosler J. On the coupling of plastic slip and deformation-induced twinning in magnesium: A variationally consistent approach based on energy minimization. Int. J. Plast. 2011;27:983.
[125] Hama T, Takuda H. Crystal-plasticity finite-element analysis of inelastic behavior during unloading in a magnesium alloy sheet. Int. J. Plast. 2011;27:1072.
[126] Fernandez A, Prado MTP, Wei YJ, Jerusalem A. Continuum modeling of the response of a Mg alloy AZ31 rolled sheet during uniaxial deformation. Int. J. Plast. 2011;27:1739.
[127] Choi SH, Kim DW, Seong BS, Rollett AD. 3-D simulation of spatial stress distribution in an AZ31 Mg alloy sheet under in-plane compression. Int. J. Plast. 2011;27:1702.
[128] Li M, Lou XY, Kim JH, Wagoner RH. An efficient constitutive model for room-temperature, low-rate plasticity of annealed Mg AZ31B sheet. Int. J. Plast. 2010;26:820.
[129] Levesque J, Inal K, Neale KW, Mishra RK. Numerical modeling of formability of extruded magnesium alloy tubes. Int. J. Plast. 2010;26:65.
[130] Neil CJ, Agnew SR. Crystal plasticity-based forming limit prediction for non-cubic metals: Application to Mg alloy AZ31B. Int. J. Plast. 2009;25:379.
[131] Lee MG, Wagoner RH, Lee JK, Chung K, Kim HY. Constitutive modeling for anisotropic/asymmetric hardening behavior of magnesium alloy sheets. Int. J. Plast. 2008;24:545.
[132] Yu Q, Zhang JX, Jiang YY, Li QZ. An experimental study on cyclic deformation and fatigue of extruded ZK60 magnesium alloy. Int. J. Fatigue 2012;36:47.
[133] Yin SM, Yang HJ, Li SX, Wu SD, Yang F. Cyclic deformation behavior of as-extruded Mg-3%Al-1%Zn. Scr. Mater. 2008;58:751.
[134] Morrow B, McCabe R, Cerreta E, Tomé C. In-Situ TEM Observation of Twinning and Detwinning During Cyclic Loading in Mg. Metall and Mat Trans A 2013:1.
[135] Brown DW, Jain A, Agnew SR, Clausen B. Twinning and detwinning during cyclic deformation of Mg alloy AZ31B. In: Chandra T, Tsuzaki K, Militzer M, Ravindran C, editors. Thermec 2006, Pts 1-5, vol. 539-543. Stafa-Zurich: Trans Tech Publications Ltd, 2007. p.3407.

[136] Tokaji K, Kamakura M, Ishiizumi Y, Hasegawa N. Fatigue behaviour and fracture mechanism of a rolled AZ31 magnesium alloy. Int J Fatigue 2004;26:1217.
[137] Tvergaard V, Hutchinson JW. The Relation between Crack-Growth Resistance and Fracture Process Parameters in Elastic Plastic Solids. Journal of the Mechanics and Physics of Solids 1992;40:1377.
[138] Evans AG, Hutchinson JW, Wei Y. Interface adhesion: Effects of plasticity and segregation. Acta Mater 1999;47:4093.
[139] Van der Giessen E, Needleman A. Micromechanics simulations of fracture. Annu Rev Mater Res 2002;32:141.
[140] Zheng LL, Gao YF, Lee SY, Barabash RI, Lee JH, Liaw PK. Intergranular strain evolution near fatigue crack tips in polycrystalline metals. Journal of the Mechanics and Physics of Solids 2011;59:2307.
[141] Zeng RC, Han EH, Ke W. A critical discussion on influence of loading frequency on fatigue crack propagation behavior for extruded Mg-Al-Zn alloys. Int J Fatigue 2012;36:40.
[142] Lee SY, Choo H, Liaw PK, An K, Hubbard CR. A study on fatigue crack growth behavior subjected to a single tensile overload: Part II. Transfer of stress concentration and its role in overload-induced transient crack growth (vol 59, pg 495, 2011). Acta Mater 2011;59:4254.
[143] Lee SY, Liaw PK, Choo H, Rogge RB. A study on fatigue crack growth behavior subjected to a single tensile overload: Part I. An overload-induced transient crack growth micromechanism (vol 59, pg 485, 2011). Acta Mater 2011;59:4253.
[144] Zeng RC, Ke W, Han EH. Influence of load frequency and ageing heat treatment on fatigue crack propagation rate of as-extruded AZ61 alloy. Int J Fatigue 2009;31:463.
[145] Ishihara S, McEvily AJ, Sato M, Taniguchi K, Goshima T. The effect of load ratio on fatigue life and crack propagation behavior of an extruded magnesium alloy. Int J Fatigue 2009;31:1788.
[146] Zeng RC, Han EH, Ke W, Dietzel W, Kainer KU, Atrens A. Influence of microstructure on tensile properties and fatigue crack growth in extruded magnesium alloy AM60. Int J Fatigue 2010;32:411.
[147] Bian L, Taheri F. Fatigue fracture criteria and microstructures of magnesium alloy plates. Mat Sci Eng a-Struct 2008;487:74.
[148] Zeng RC, Xu YB, Ke W, Han EH. Fatigue crack propagation behavior of an as-extruded magnesium alloy AZ80. Mat Sci Eng a-Struct 2009;509:1.
[149] Xu F, Holt RA, Daymond MR. Modeling lattice strain evolution during uniaxial deformation of textured Zircaloy-2. Acta Mater 2008;56:3672.
[150] Molinari A, Canova GR, Ahzi S. A Self-Consistent Approach of the Large Deformation Polycrystal Viscoplasticity. Acta Metallurgica 1987;35:2983.
[151] Lebensohn RA, Tome CN. A Self-Consistent Anisotropic Approach for the Simulation of Plastic-Deformation and Texture Development of Polycrystals - Application to Zirconium Alloys. Acta Metallurgica Et Materialia 1993;41:2611.
[152] Jain A, Agnew SR. Modeling the temperature dependent effect of twinning on the behavior of magnesium alloy AZ31B sheet. Mat Sci Eng a-Struct 2007;462:29.

[153] Turner PA, Tome CN. A Study of Residual-Stresses in Zircaloy-2 with Rod Texture. Acta Metallurgica Et Materialia 1994;42:4143.
[154] Wang H, Wu PD, Tome CN, Huang Y. A finite strain elastic-viscoplastic self-consistent model for polycrystalline materials. Journal of the Mechanics and Physics of Solids 2010;58:594.
[155] Wang H, Wu PD, Tome CN, Wang J. A constitutive model of twinning and detwinning for hexagonal close packed polycrystals. Mat Sci Eng a-Struct 2012;555:93.
[156] Wang H, Wu PD, Tome CN, Wang J. Study of lattice strains in magnesium alloy AZ31 based on a large strain elastic-viscoplastic self-consistent polycrystal model. International Journal of Solids and Structures 2012;49:2155.
[157] Wang H, Wu PD, Tomé CN, Wang J. A constitutive model of twinning and detwinning for hexagonal close packed polycrystals. Materials Science and Engineering: A 2012;555:93.
[158] Wang H, Raeisinia B, Wu PD, Agnew SR, Tome CN. Evaluation of self-consistent polycrystal plasticity models for magnesium alloy AZ31B sheet. International Journal of Solids and Structures 2010;47:2905.
[159] Wang H, Wu PD, Neale KW. On the role of the constitutive model and basal texture on the mechanical behaviour of magnesium alloy AZ31B sheet. J Zhejiang Univ-Sc A 2010;11:744.
[160] Wang H, Wu PD, Boyle KP, Neale KW. On crystal plasticity formability analysis for magnesium alloy sheets. International Journal of Solids and Structures 2011;48:1000.
[161] ASTM Test Standard E647-13e1. 2013; DOI: 10.1520/E0647-13E01.
[162] Wang XL, Holden TM, Rennich GQ, Stoica AD, Liaw PK, Choo H, Hubbard CR. VULCAN - The engineering diffractometer at the SNS. Physica B-Condensed Matter 2006;385:673.
[163] Wang XL, Stoica AD. Focusing neutron guides for VULCAN-Design aspects, estimated performance, and detector deployment. Nucl Instrum Meth A 2009;600:309.
[164] Wu W, An K, Huang L, Lee SY, Liaw PK. Deformation dynamics study of a wrought magnesium alloy by real-time in situ neutron diffraction. Scr. Mater. 2013;69:358.
[165] An K. VDRIVE-Data Reduction and Interactive Visualization Software for Event Mode Neutron Diffraction. ORNL Report No. ORNL-TM-2012-621 2012;Oak Ridge National Laboratory, Oak Ridge, TN.
[166] Santisteban JR, Daymond MR, James JA, Edwards L. ENGIN-X: a third-generation neutron strain scanner. J Appl Crystallogr 2006;39:812.
[167] Wang H, Wu PD, Tomé CN, Huang Y. A finite strain elastic–viscoplastic self-consistent model for polycrystalline materials. Journal of the Mechanics and Physics of Solids 2010;58:594.
[168] Wang H, Raeisinia B, Wu PD, Agnew SR, Tomé CN. Evaluation of self-consistent polycrystal plasticity models for magnesium alloy AZ31B sheet. International Journal of Solids and Structures 2010;47:2905.

[169] Wang H, Wu PD, Gharghouri MA. Effects of basal texture on mechanical behaviour of magnesium alloy AZ31B sheet. Materials Science and Engineering: A 2010;527:3588.
[170] Wang H, Wu PD, Tomé CN, Wang J. Study of lattice strains in magnesium alloy AZ31 based on a large strain elastic-viscoplastic self-consistent polycrystal model. International Journal of Solids and Structures 2012;49:2155.
[171] Wang H, Wu PD, Wang J. Modeling inelastic behavior of magnesium alloys during cyclic loading–unloading. Int. J. Plast. 2013;47:49.
[172] Roberts CS. Magnesium and its alloys. New York: John Wiley & Sons, Inc, 1960.
[173] Agnew S, Yoo M, Tome C. Application of texture simulation to understanding mechanical behavior of Mg and solid solution alloys containing Li or Y. Acta Mater 2001:4277.
[174] Caceres CH, Sumitomo T, Veidt M. Pseudoelastic behaviour of cast magnesium AZ91 alloy under cyclic loading-unloading. Acta Mater 2003;51:6211.
[175] Benafan O, Noebe RD, Padula Ii SA, Gaydosh DJ, Lerch BA, Garg A, Bigelow GS, An K, Vaidyanathan R. Temperature-dependent behavior of a polycrystalline NiTi shape memory alloy around the transformation regime. Scripta Mater 2013;68:571.
[176] Lin YC, Chen XM, Liu ZH, Chen J. Investigation of uniaxial low-cycle fatigue failure behavior of hot-rolled AZ91 magnesium alloy. Int. J. Fatigue 2013;48:122.
[177] Yu Q, Zhang JX, Jiang YY, Li QZ. Multiaxial fatigue of extruded AZ61A magnesium alloy. Int. J. Fatigue 2011;33:437.
[178] Skippon T, Clausen B, Daymond MR. Effect of loading mode on lattice strain measurements via neutron diffraction. Mater. Sci. Eng. A-Struct. Mater. Prop. Microstruct. Process. 2013;577:169.
[179] Barabash R, Gao Y, Sun Y, Lee S, Choo H, Liaw P, Brown D, Ice G. Neutron and X-ray diffraction studies and choehsive interface model of the fatigue crack deformation behavior. Phil Mag Lett 2008;88:553.
[180] Lou XY, Li M, Boger RK, Wagoner RH. Hardening evolution of AZ31B Mg sheet. Int. J. Plast. 2007;23:44.
[181] Jain J, Poole WJ, Sinclair CW, Gharghouri MA. Reducing the tension-compression yield asymmetry in a Mg-8Al-0.5Zn alloy via precipitation. Scripta Mater 2010;62:301.

APPENDIX: TABLE AND FIGURES

Table 1 List of material parameters for slip and twin systems used in the EVPSC-TDT model. The parameter, h^{st}, lists latent hardening of the twinning activity upon other slip modes. All other latent-hardening parameters are 1.

Mode	τ_1 (MPa)	τ_2 (MPa)	h_0 (MPa)	h_1 (MPa)	h^{st}	A_1	A_2
Basal	12	1	10	0	1		
Prismatic	78	55	600	30	1		
Pyramidal	100	140	2500	40	1		
Extension twin	35	10	100	10	1	0.65	0.75

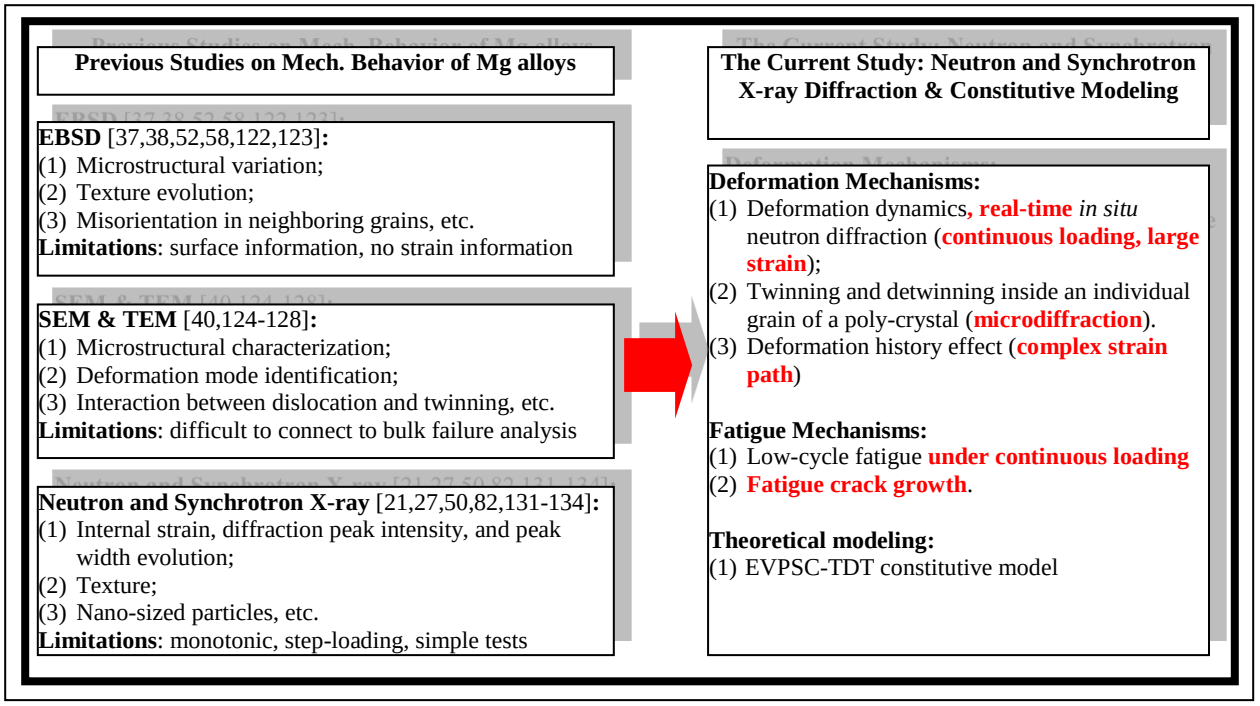

Figure 1.1 A comparison of literature and proposed work on the study of Mg alloys.

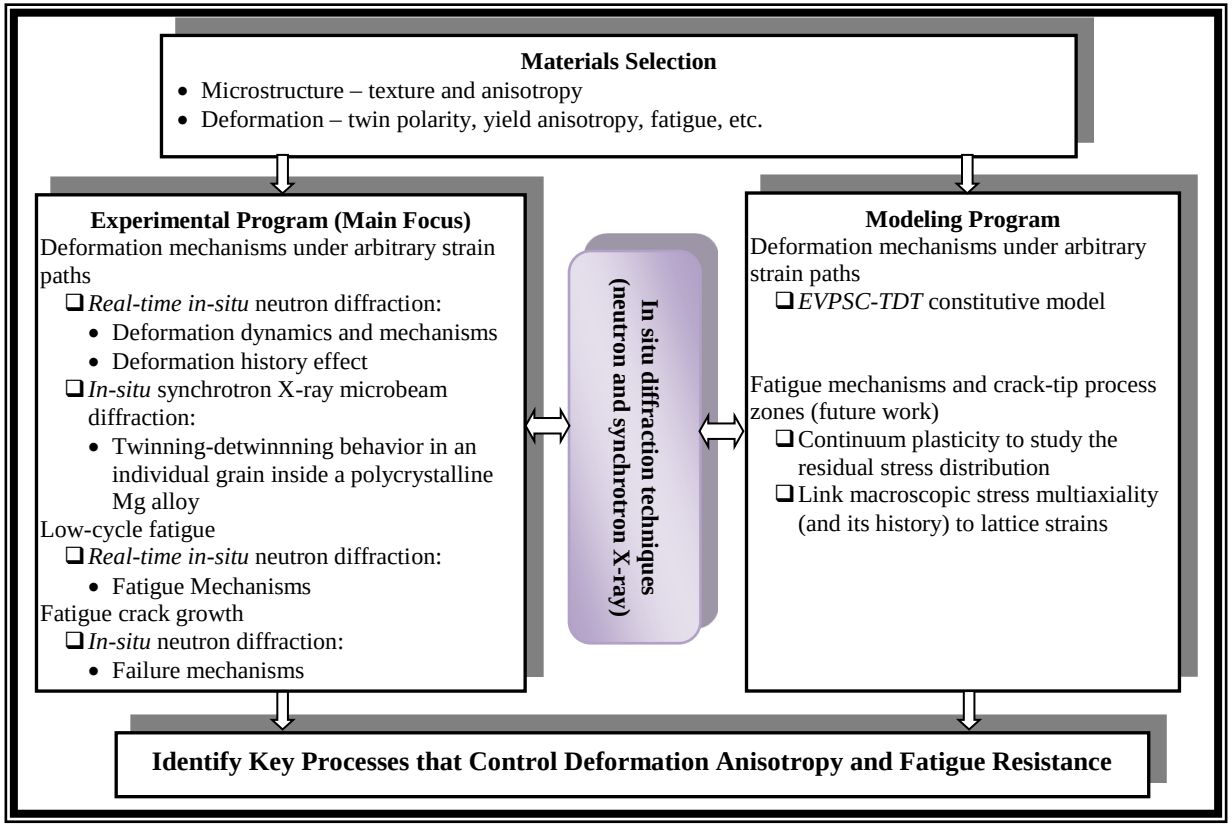

Figure 1.2 Schematic illustration of the proposed research.

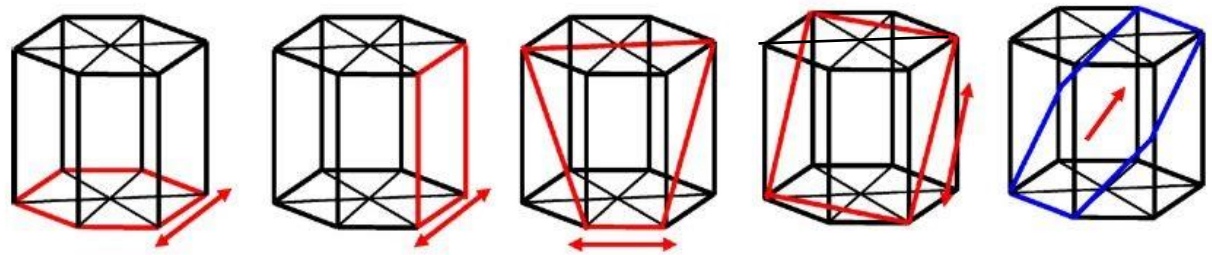

Basal <a> slip	Prismatic <a> slip	Pyramidal <a> slip	Pyramidal <c+a> slip	Extension twinning
{00.2}<11.0>	{10.0}<11.0>	{10.1}<11.0>	{11.2}<11.3>	{10.2}<10.1>

Figure 2.2 Deformation systems in Mg [22].

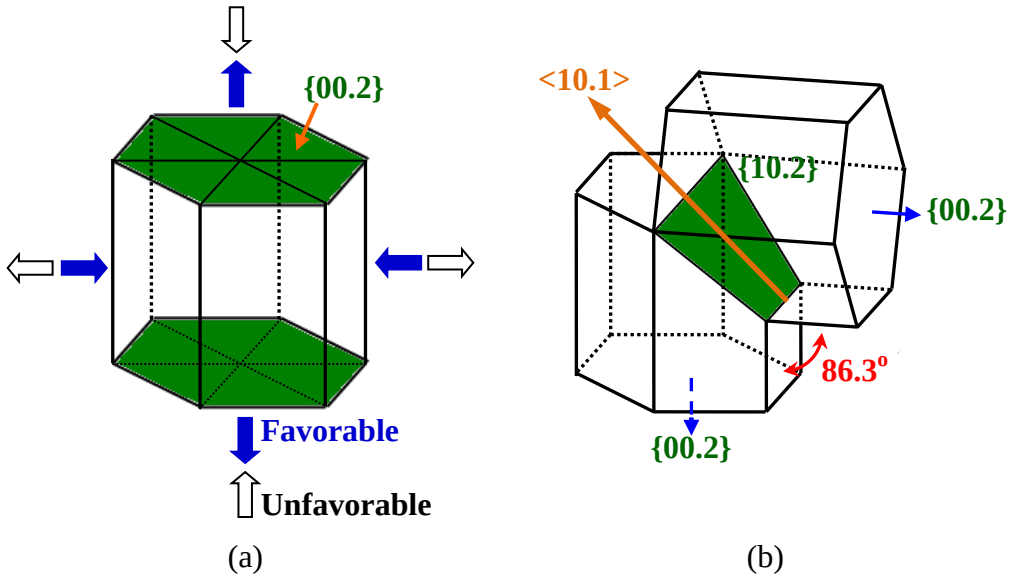

Figure 2.3 Schematic of the {10.2}<10.1> tensile twin system in Mg: (a) applied loading direction with respect of the c-axis. The solid arrows indicate the applied loading direction favorable for the tensile twinning, and the open arrows indicate the applied loading directions unfavorable for the tensile twinning. (b) 86.3^{o} reorientation of the twin grain relative to the parent grain [27].

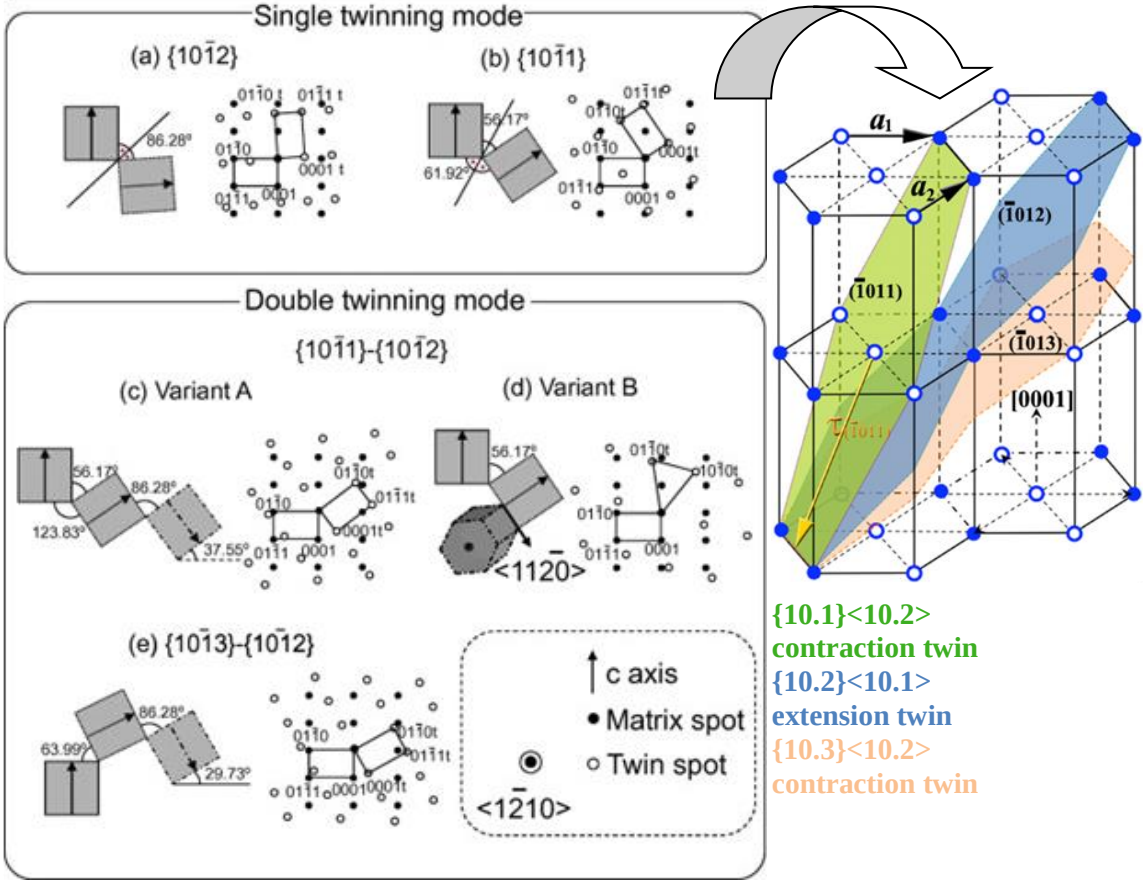

Figure 2.4 Schematic diagram of the HCP lattices and diffraction patterns are given for the matrix and twins [32,33].

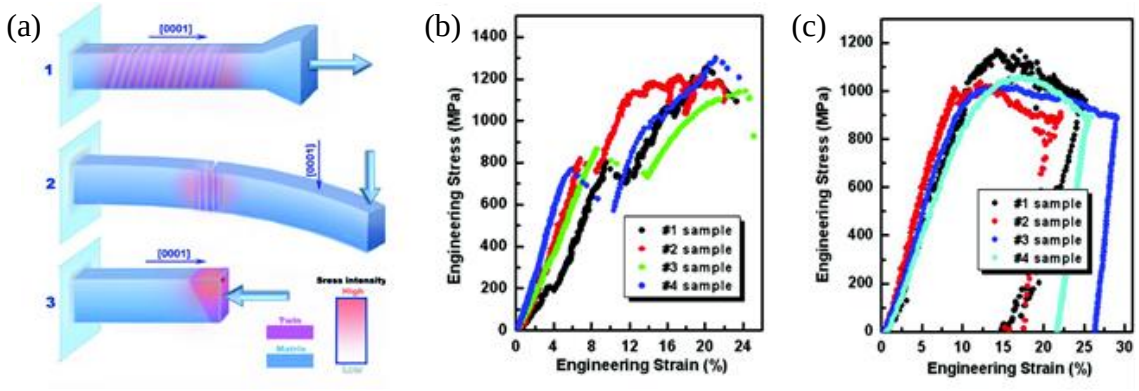

Figure 2.5 A schematic to illustrate different results from 1-tension, 2-bending, and 3-compression testing. (b) Stress−strain curves from in situ tensile tests. Formation stress of twins can be read at the beginning of strain burst. Strong strain hardening was observed. (c) Stress−strain curves from in situ compression tests. Strain softening is obvious [40].

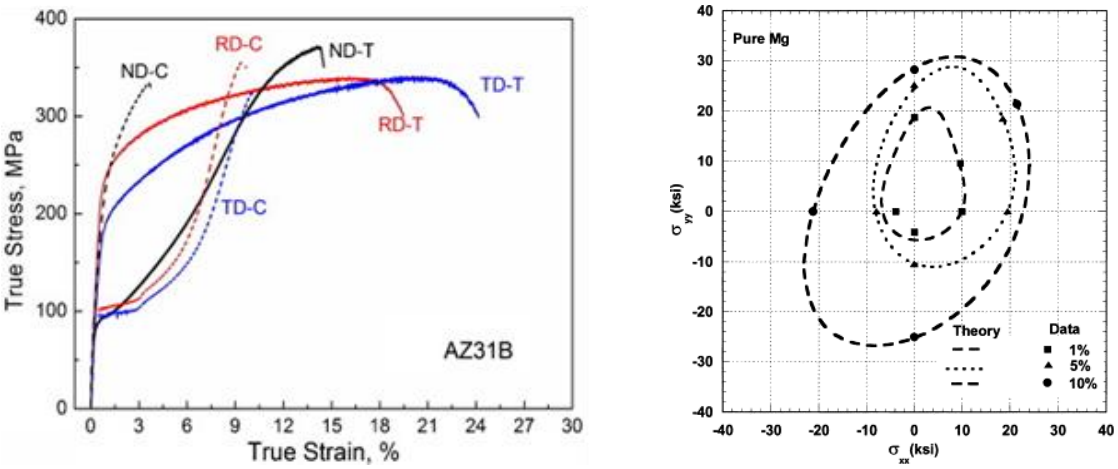

(a) (b)

Figure 2.6 The monotonic mechanical responses loaded, respectively, along the RD, TD and ND directions both under compression (C) and tension (T) of a wrought AZ31B alloy [50]. (b) Plane stress yield loci for a magnesium sheet predicted by the proposed theory and experiments [51].

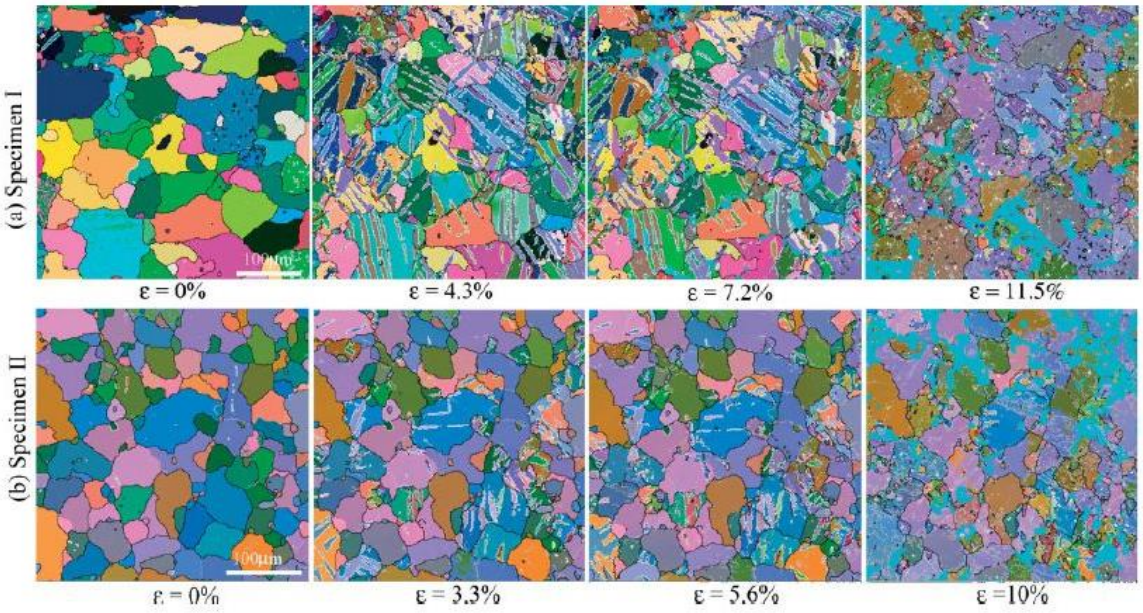

Figure 2.7 Euler angle contrast maps at different compressive strain using quasi-in-situ EBSD: (a) compression axis parallel to the extrusion direction, (b) compression axis perpendicular to the extrusion direction. White lines indicated the twin boundaries. Compression direction is horizontal [58].

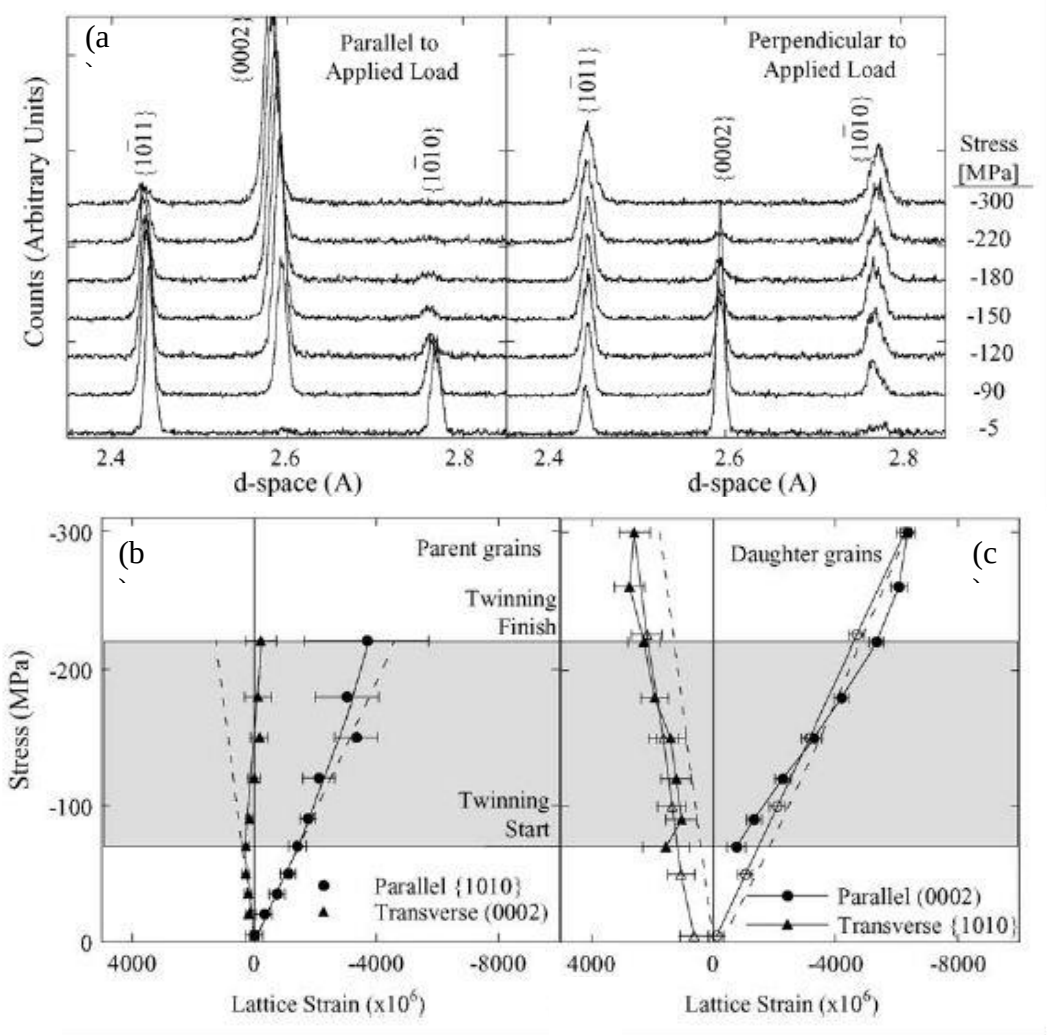

Figure 2.8 An example of "traditional" in-situ neutron diffraction measurements: (a) Diffraction patterns during in-plane compression of magnesium in parallel and perpendicular detector banks as a function of applied stress. The patterns have been offset vertically for clarity. (b) Internal strains parallel and perpendicular to the load axis in parent grains. (c) Internal strains parallel and perpendicular to the load axis in daughter grains. Closed (open) symbols represent data taken on loading (unloading). Dashed lines represent elastic behavior.

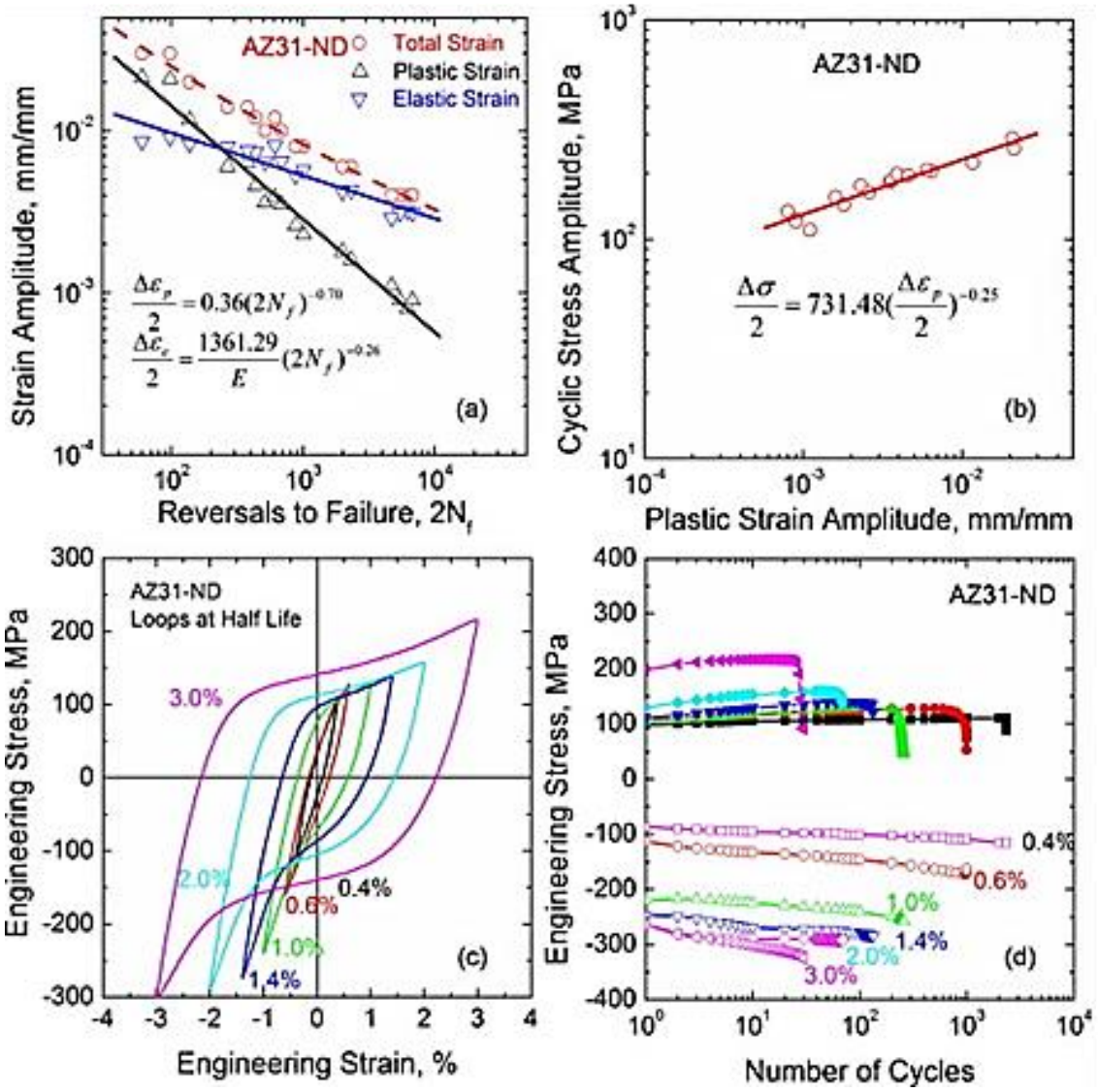

Figure 2.9 The low-cycle fatigue behavior of the as-rolled AZ31B alloy under the ND loading: (a) ε–N fatigue life curves; (b) cyclic stress and strain curves; (c) hysteresis loops at half-life for various total strain amplitudes; and (d) cyclic tensile and compressive peak stress responses [50].

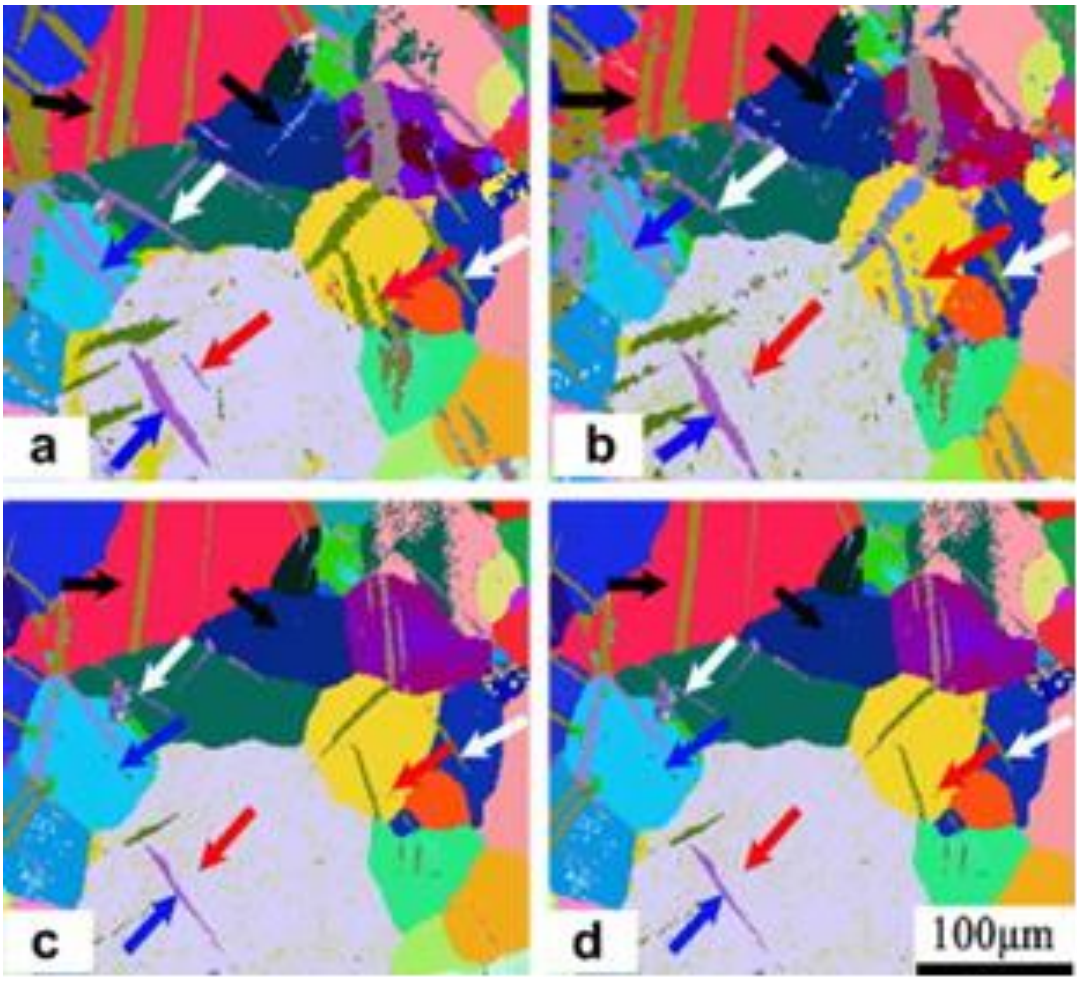

Figure 2.10 EBSD map of in situ observation. (a) Compressive strain ~0.5%, (b) unloading from compression, (c) loading reverses from compression to tension at tensile strain ~0.7%, (d) unloading from tension [81].

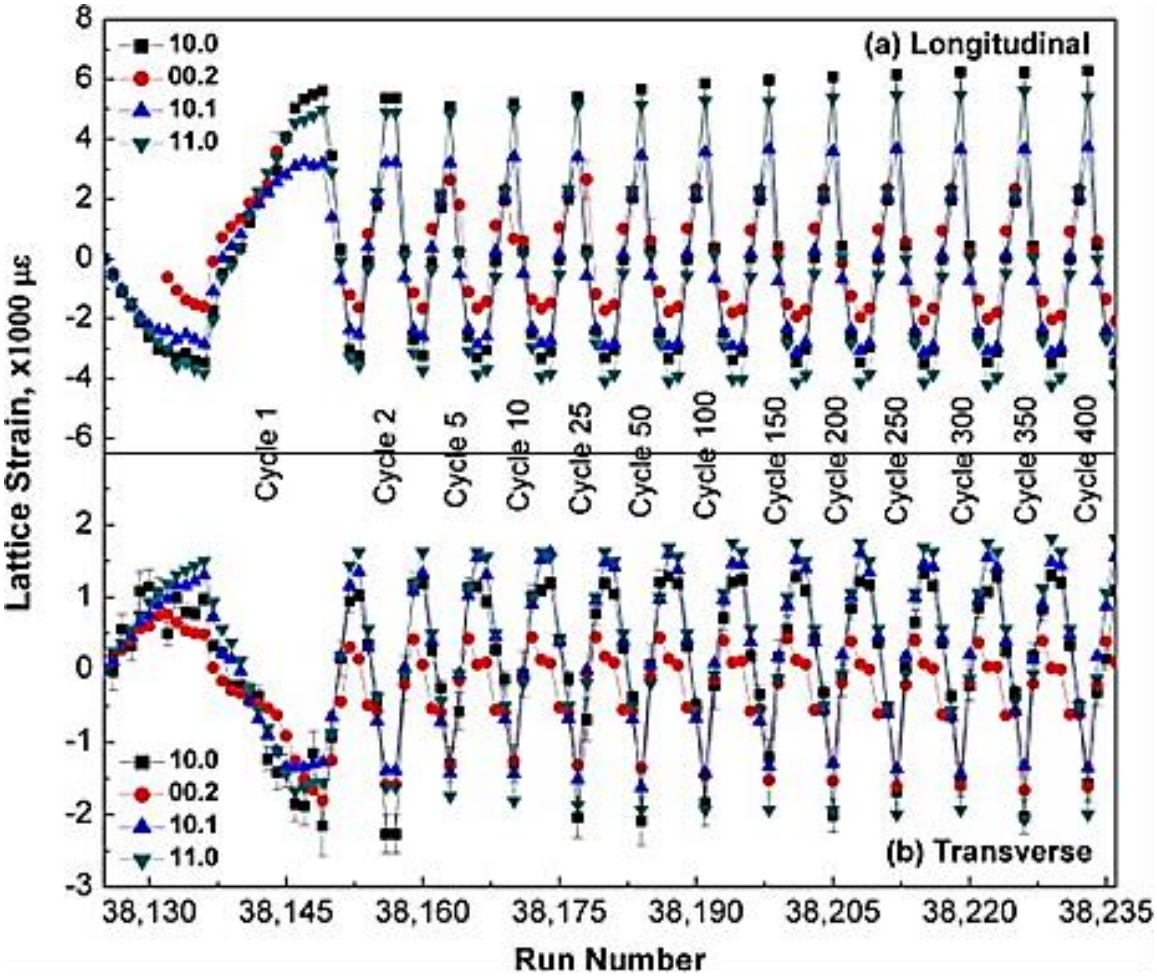

Figure 2.11 Lattice strains as a function of run number for a wrought ZK60 Mg alloy, indicating cyclic evolution of lattice strains: (a) in the longitudinal direction; (b) in the transverse direction. The internal strain development in the following cycles closely follows the evolution during the first cycle deformation [82].

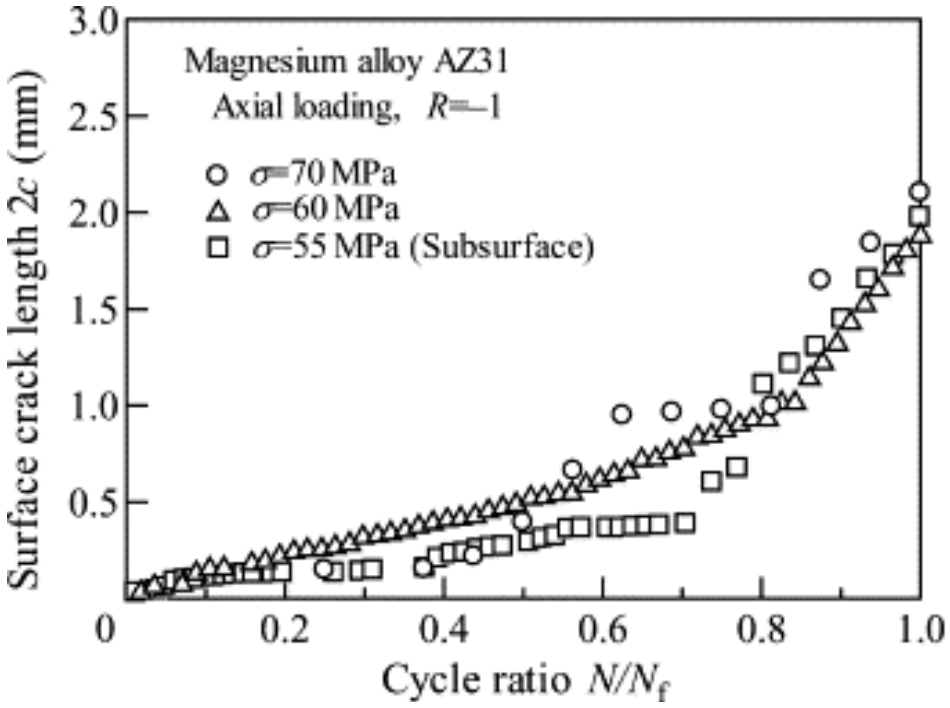

Figure 2.12 Surface crack length as a function of cycle ratio for a wrought AZ31B Mg alloy [83].

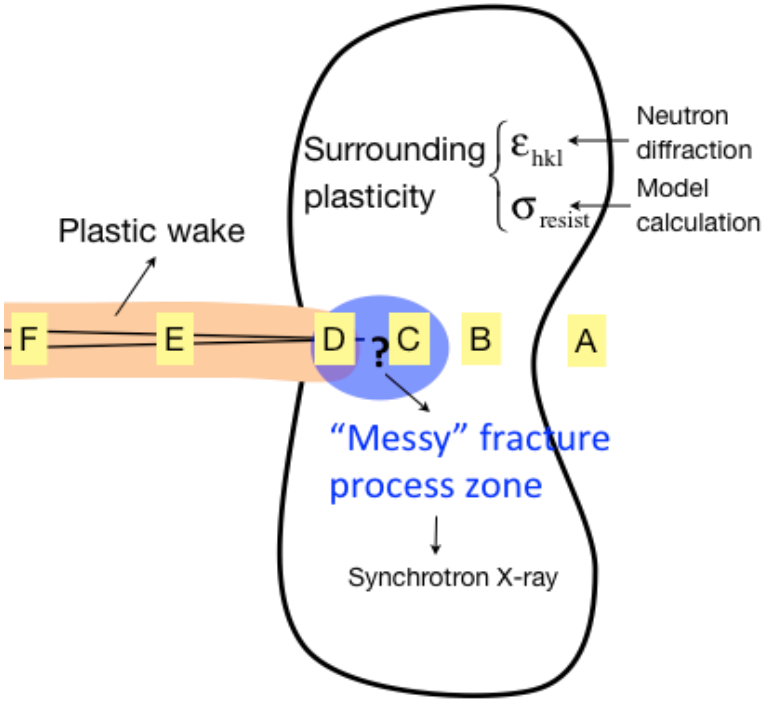

Figure 2.13 Multiscale nature of fatigue crack tip process zones [84-87].

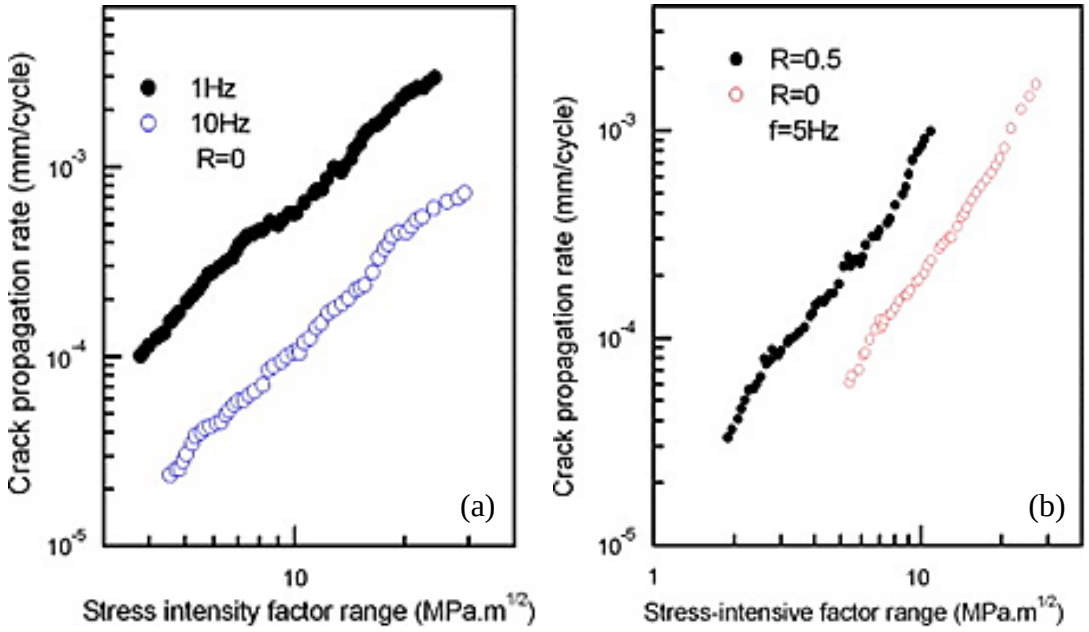

Figure 2.14 Influence of (a) frequency and (b) load ratio, R, on the fatigue crack propagation rate of as-extruded magnesium alloy AZ80 [95].

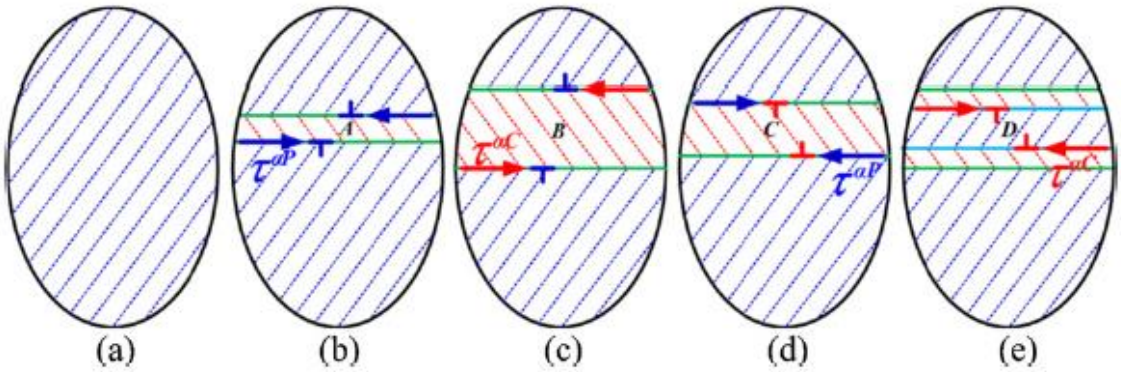

Figure 2.15 Schematic representation of twinning and detwinning in a grain.

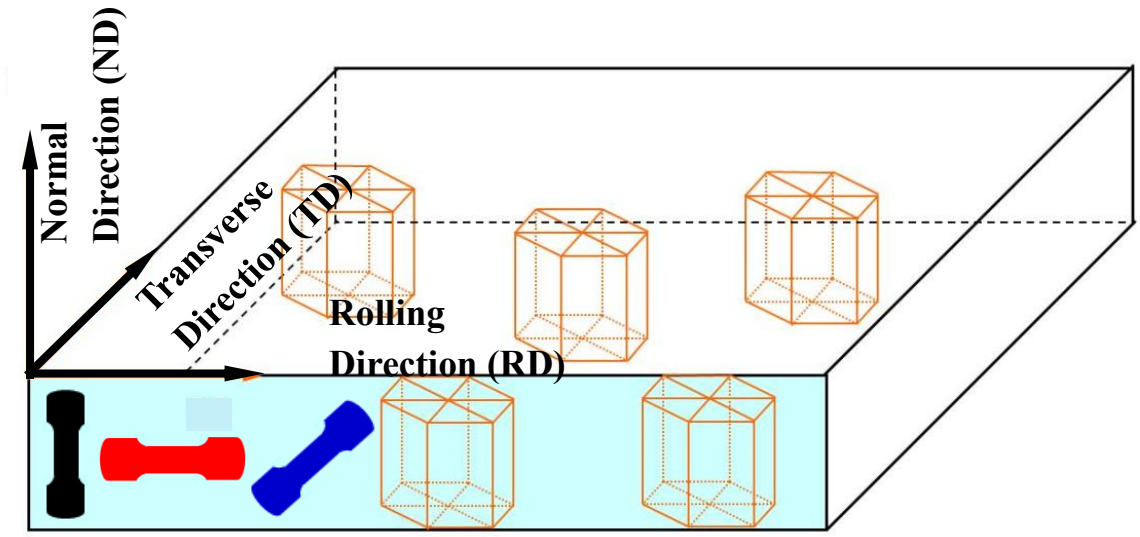

Figure 3.1 Schematic of AZ31B Mg rolled plate.

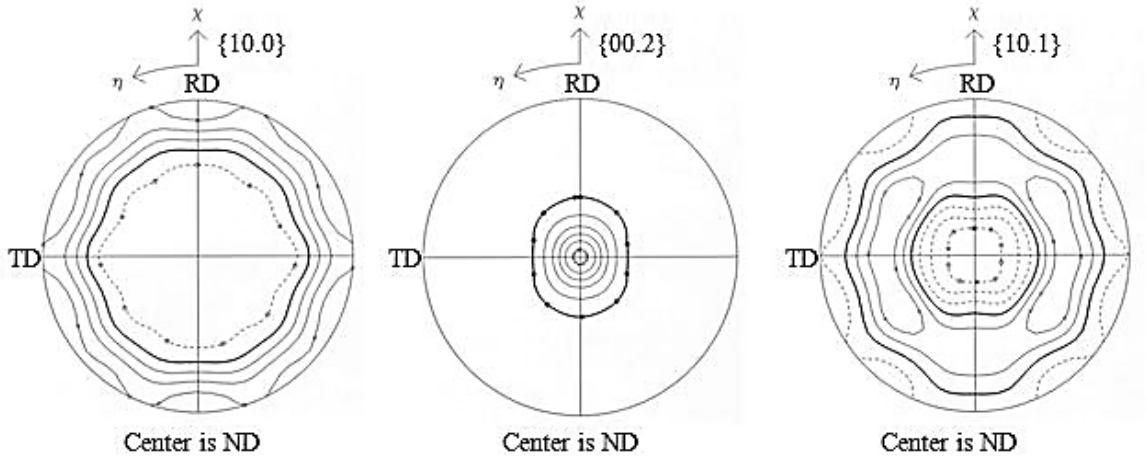

Figure 3.2 The Pole figures of the anneal sample.

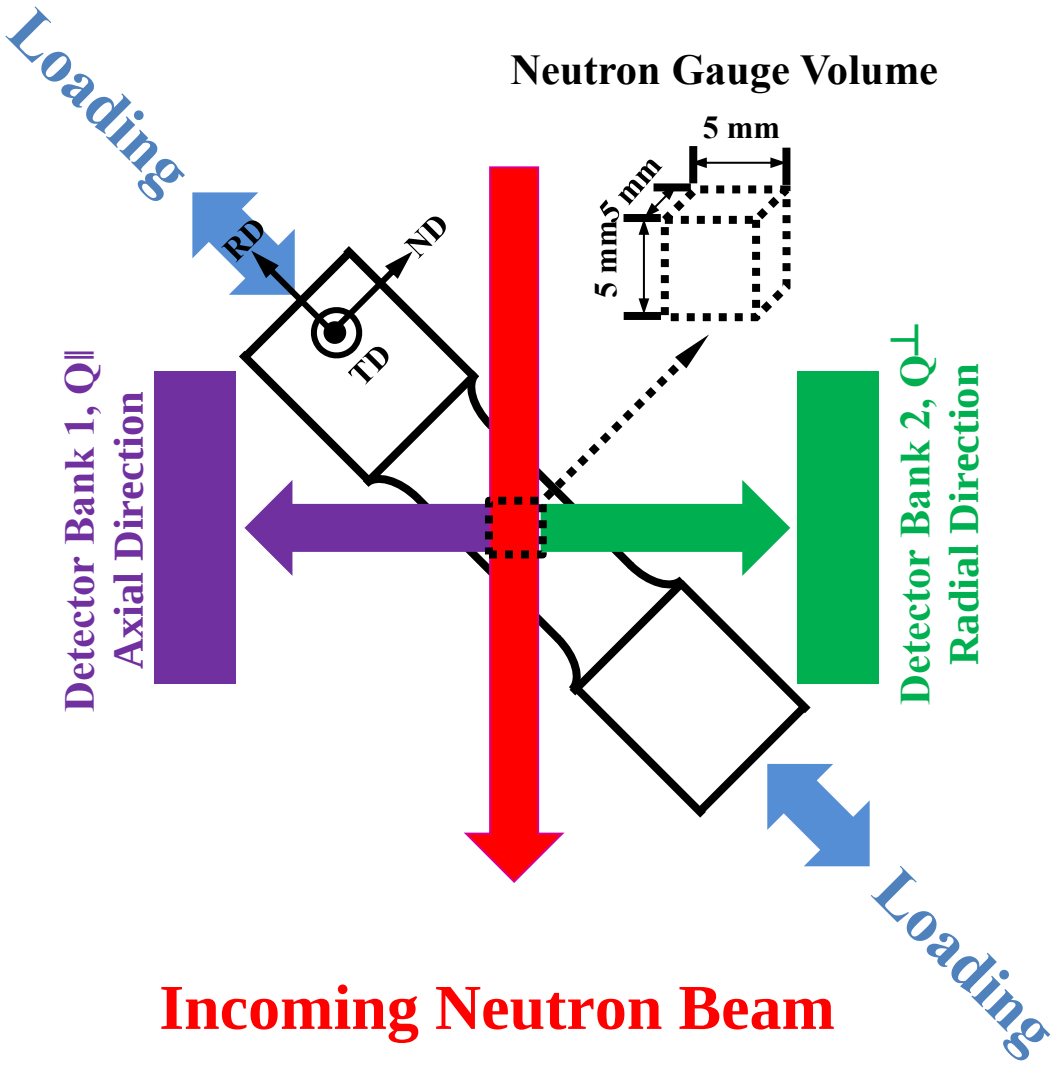

Figure 3.3 Schematic of a real-time in-situ neutron diffraction setup at VULCAN, SNS, ORNL.

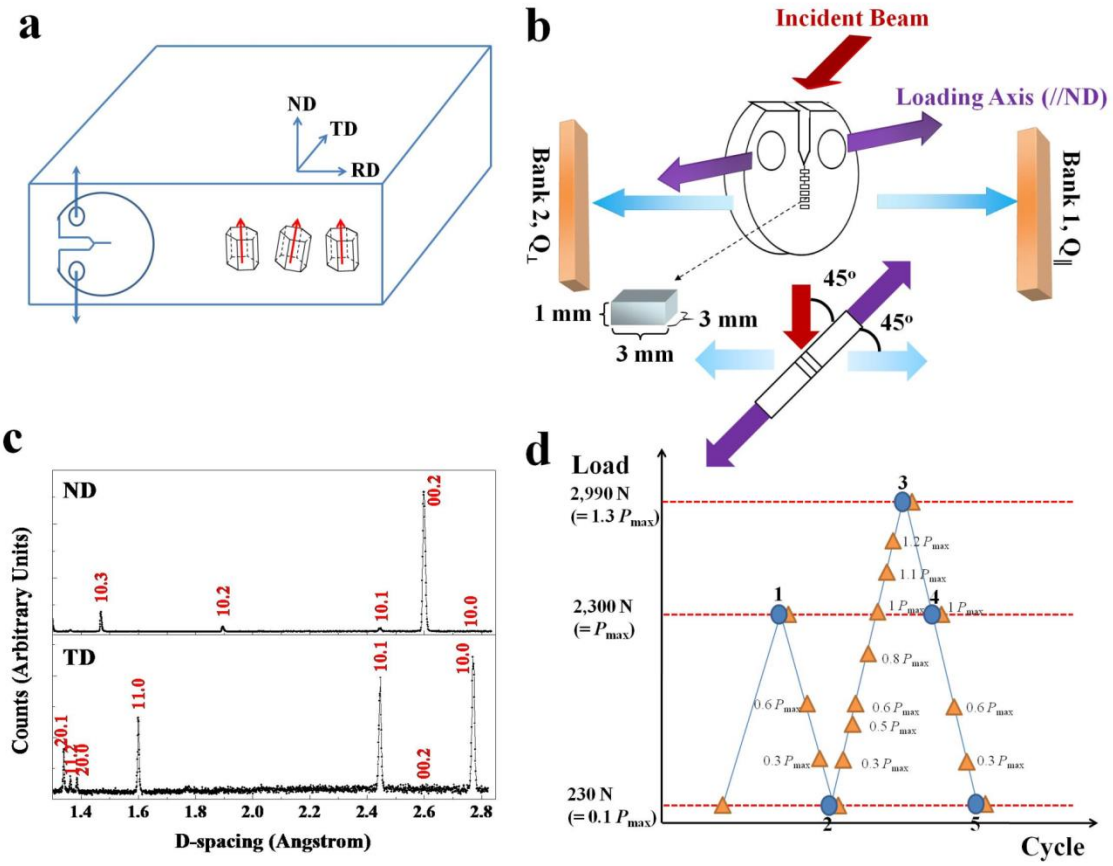

Figure 3.4 Geometry of the specimen and experimental setup at Engin-X, ISIS facility, for in-situ neutron-diffraction experiments: (a) disk-shaped compact-tension specimen was cut from a 76-mm thick hot-rolled AZ31B magnesium plate in the plane of the rolling direction (RD) and normal direction (ND). The fatigue loading direction and crack growth direction are parallel to the plate ND and RD, respectively. (b) schematic of the diffraction geometry for in-situ neutron-diffraction measurements. The bank 1 collects the *hkl* grains with the scattering vector parallel to the fatigue loading direction, which corresponds to the ND, Fig 1a. The bank 2 collects the *hkl* grains with the scattering vector perpendicular to the fatigue loading direction, which corresponds to the TD, Fig. 1a. The strain mapping is performed along the crack growth direction, RD, Fig. 1a. (c) diffraction patterns measured from both detector banks show the strong initial rolling texture of a wrought AZ31B magnesium alloy. (d) The strain mapping is conducted as a function of the distance from the crack tip (covering –2 to 3 mm) at five different loading points marked with a blue circle. More detailed loading steps (marked with an orange triangle) are employed only at 0.5 mm in front of the crack tip, where high stress concentration is expected.

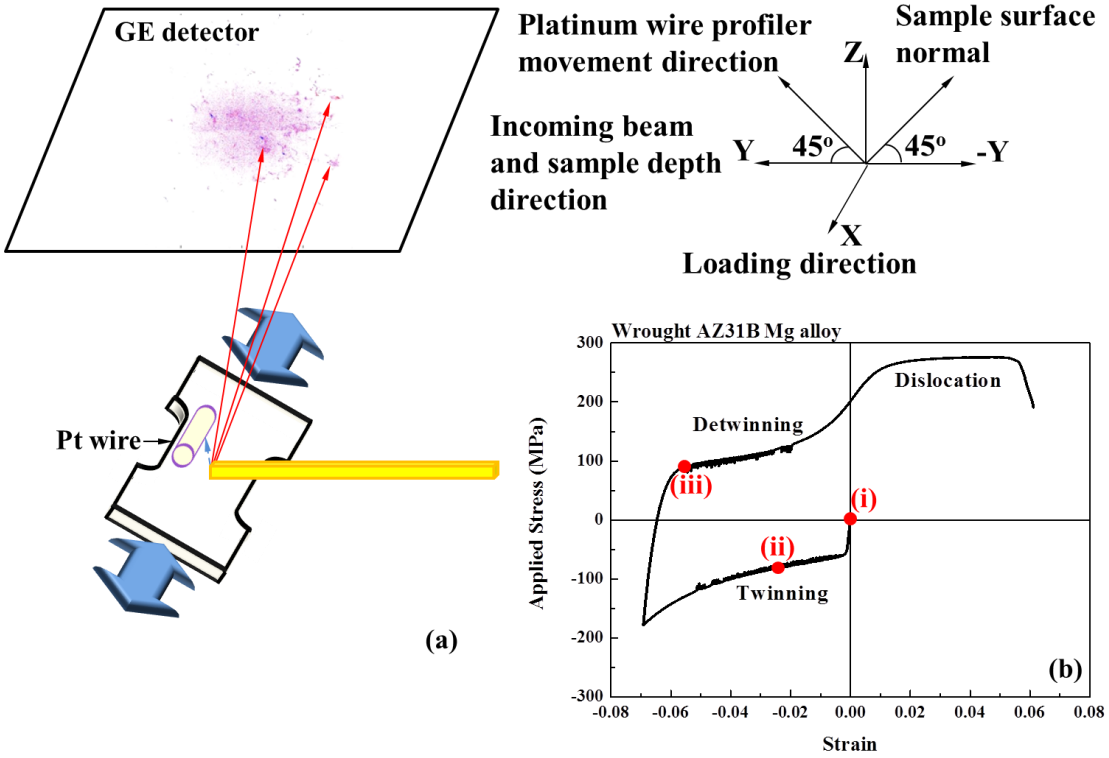

Figure 3.5 (a) Schematic of synchrotron X-ray microbeam diffraction. (b) The stress-strain curve for a wrought AZ31B Mg alloy. The red dots represent the synchrotron X-ray microbeam diffraction measurements.

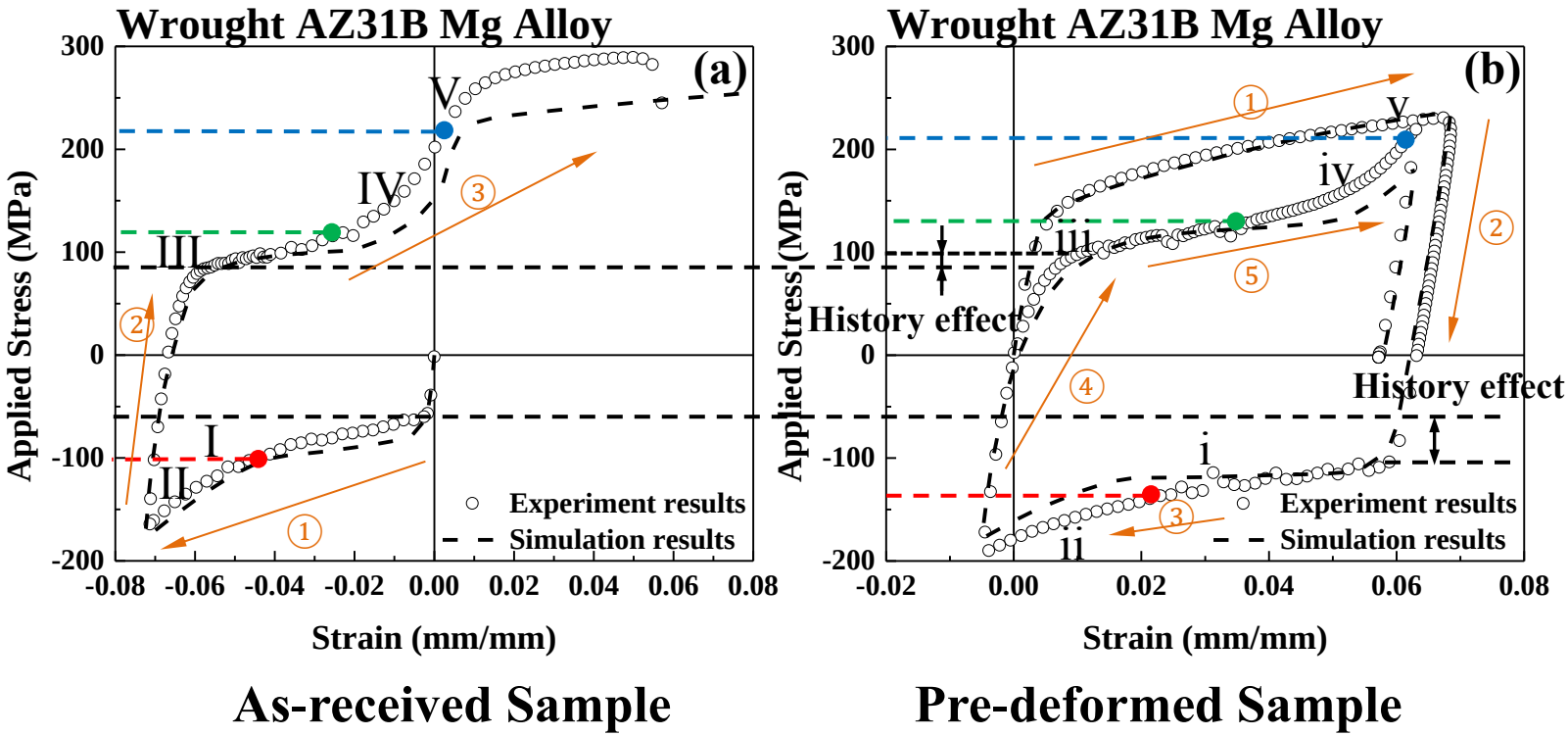

Figure 4. 1 The stress vs. strain curves during strain-path changes for: (a) the as-received sample and (b) the pre-deformed sample [44]. The loading sequence was marked by the orange arrows and circled numbers. The inflection points of the stress-strain curves were marked by colored dots.

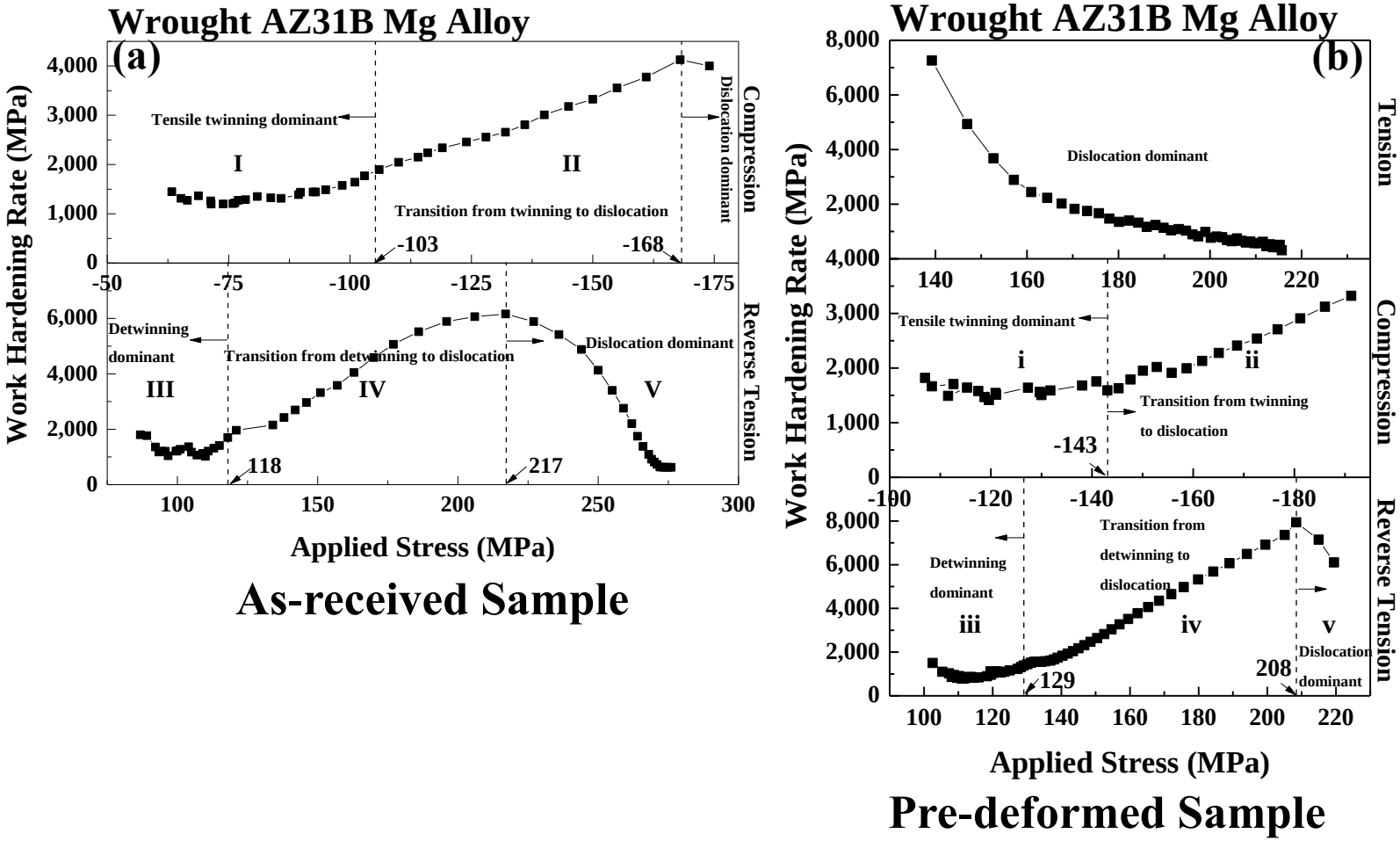

Figure 4.2 The work-hardening rate as a function of stress during the strain-path changes for: (a) the as-received sample and (b) the pre-deformed sample. The stress ranges were divided based on the work-hardening rate changes, denoted by Roman numerals.

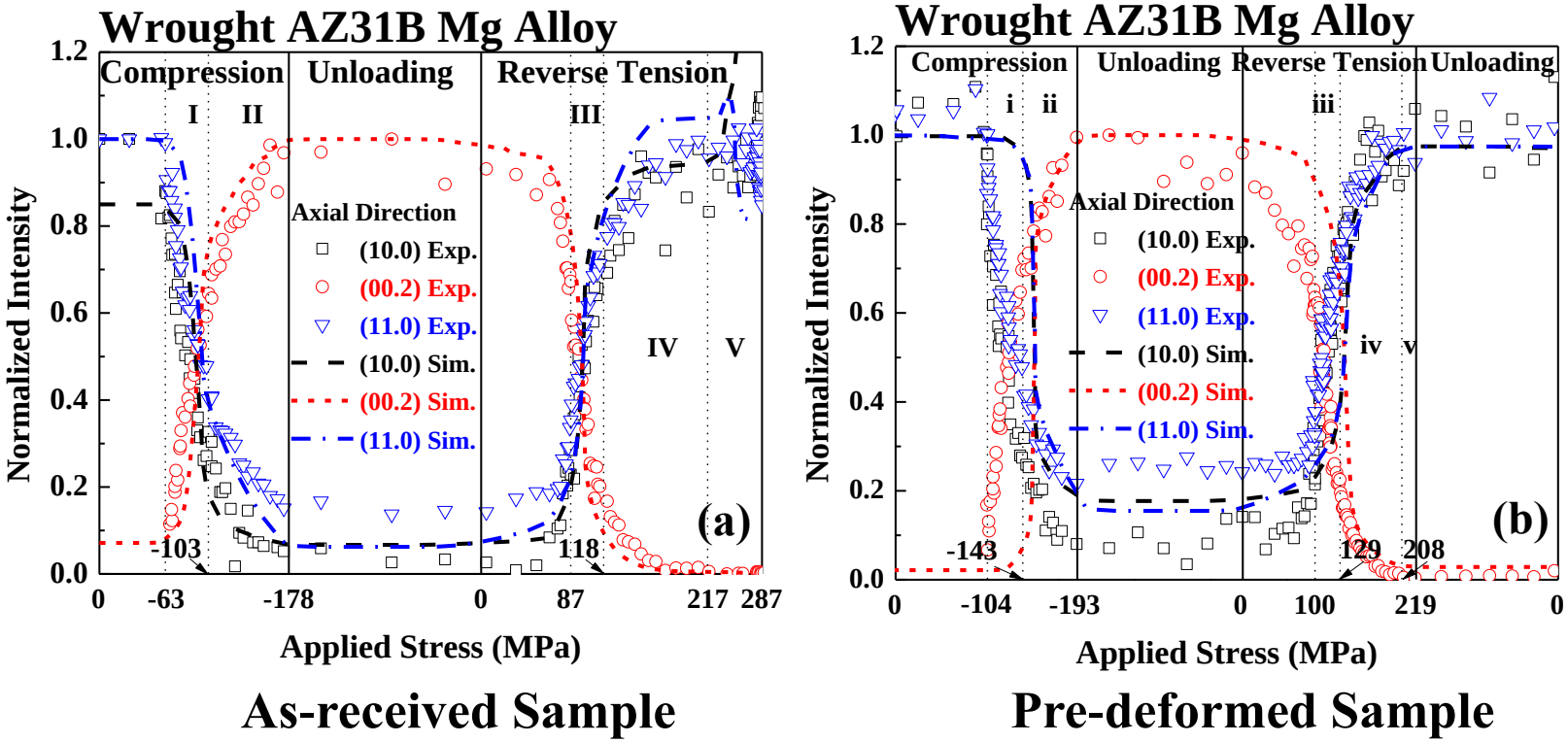

Figure 4.3 The diffraction peak intensity evolution of certain *hkl*s as a function of stress in the axial direction from real-time in-situ neutron diffraction measurements (open symbols) and simulations (dashed lines) for: (a) the as-received sample and (b) the pre-deformed sample.

Figure 4.4 The internal-strain evolutions of certain *hkl*s from real-time in-situ neutron diffraction measurements. (a), (c), (e), and (g) represent the lattice-strain evolution of the as-received sample, and (b), (d), (f), and (h) are the lattice-strain evolution of the pre-deformed sample during strain-path changes.

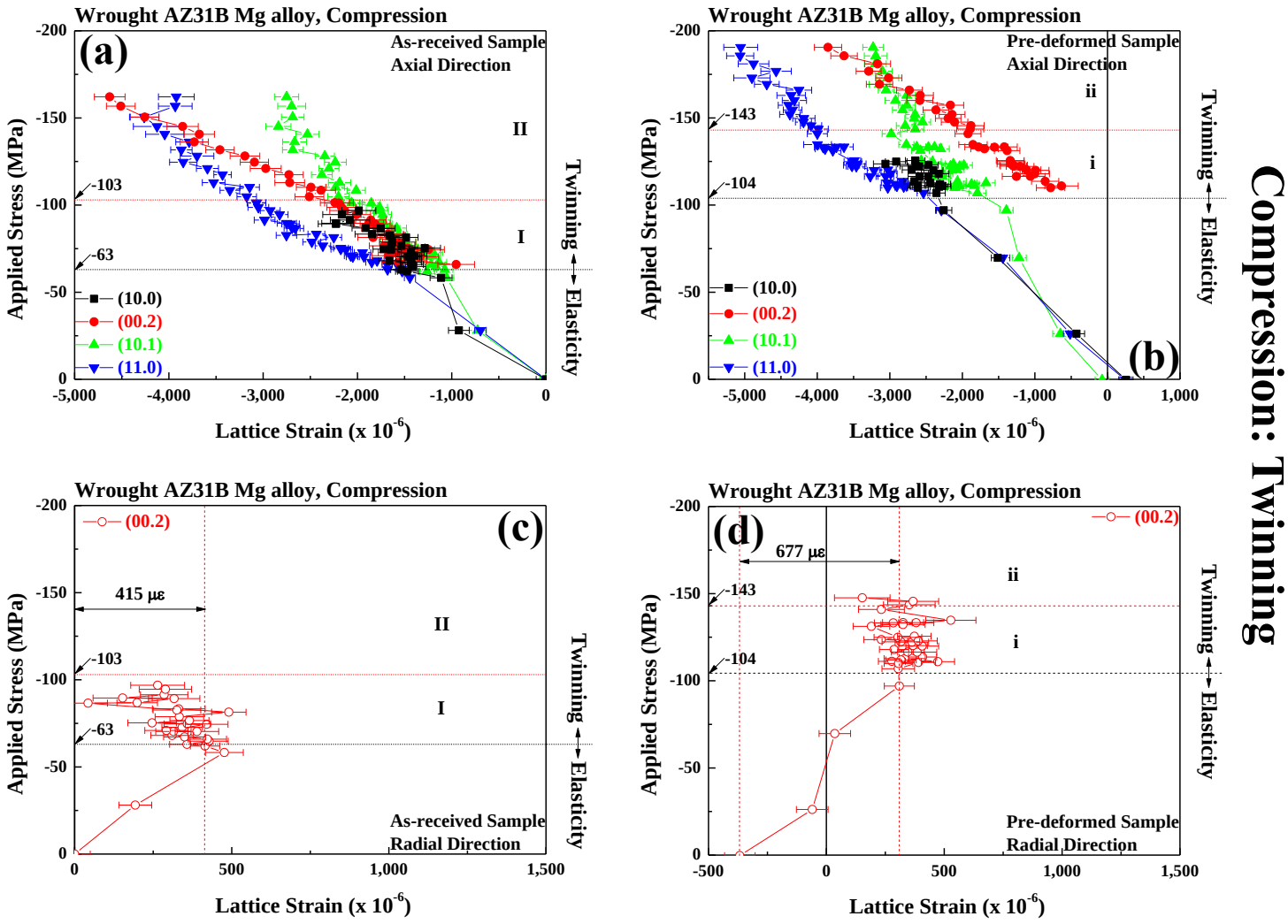

Figure 4.4 continued

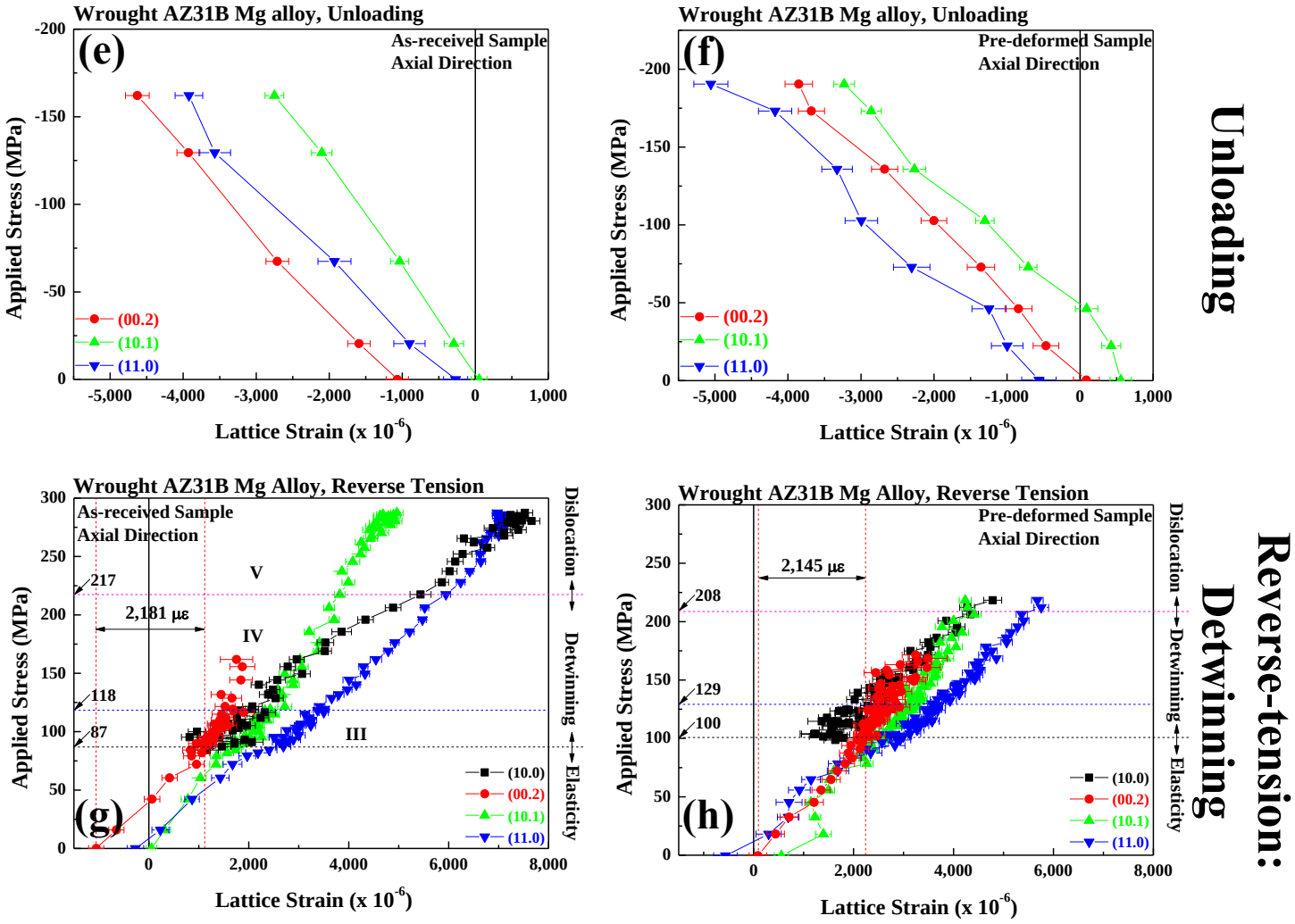

Figure 4.4 continued

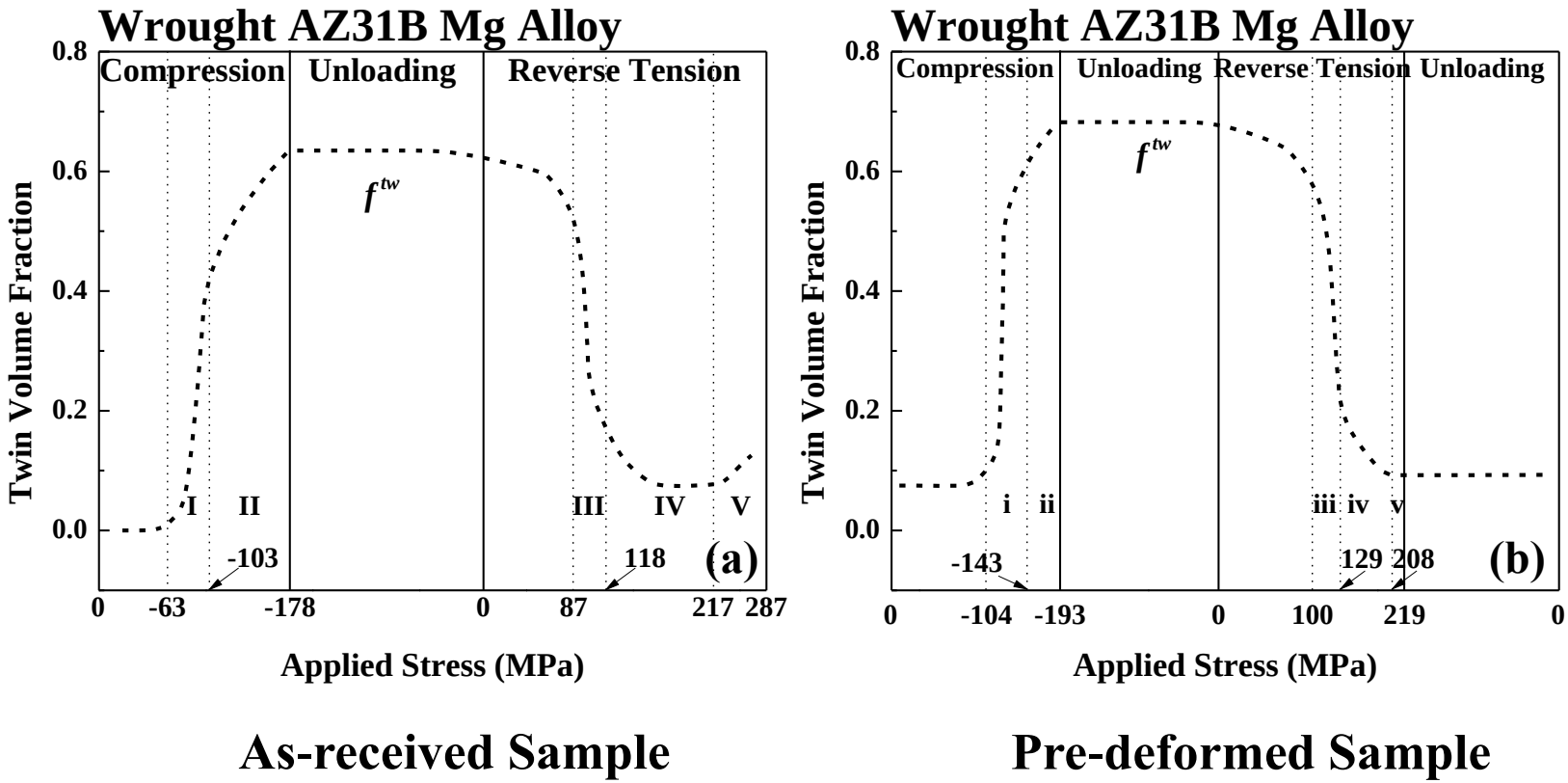

Figure 4.5 The simulation results of the twin-volume-fraction variation during strain-path changes for: (a) the as-received sample and (b) the pre-deformed sample.

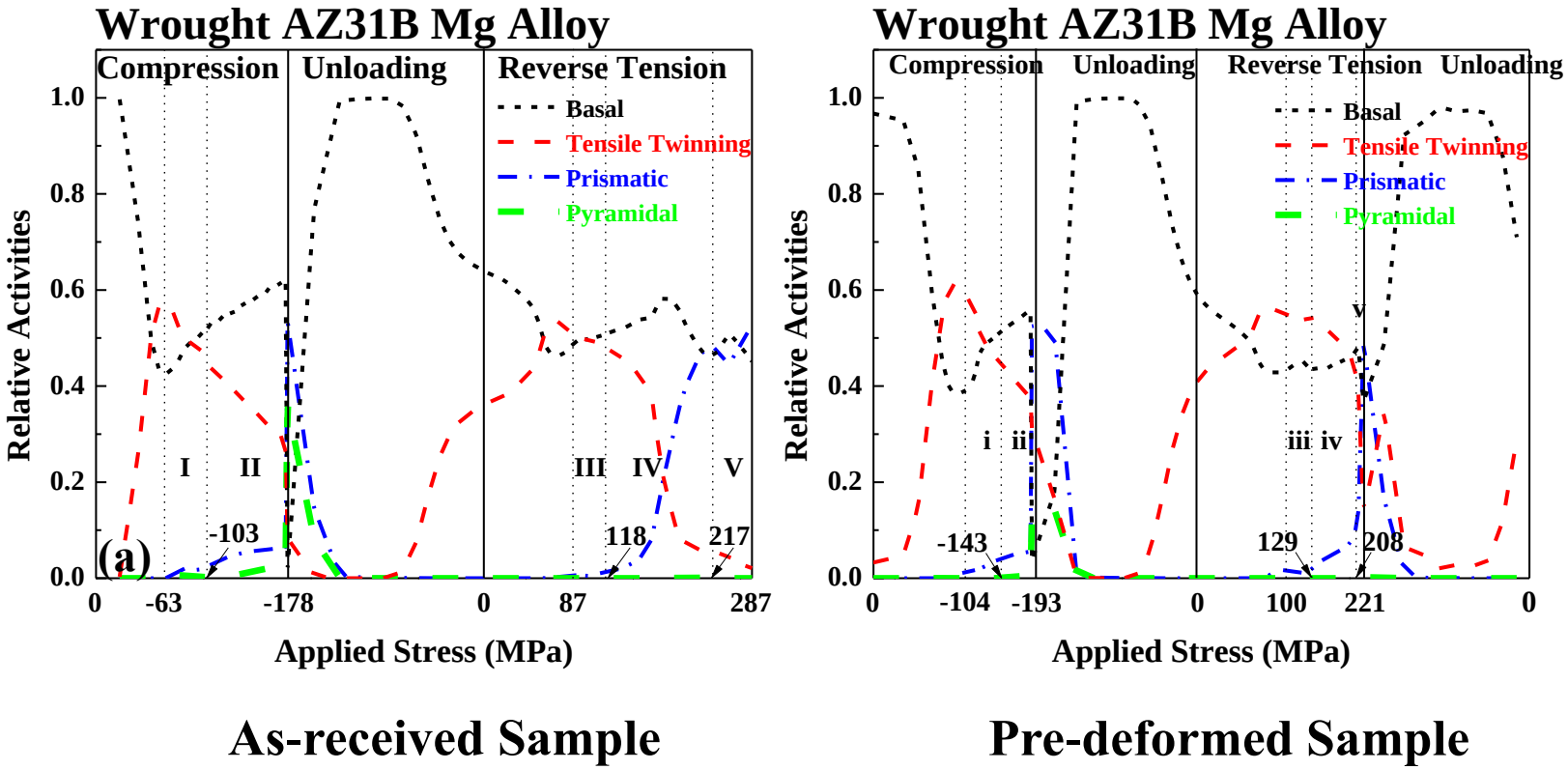

Figure 4.6 The relative activities of interested deformation modes during the strain-path changes from the EVPSC-TDT model for: (a) as-received sample and (b) pre-deformed sample.

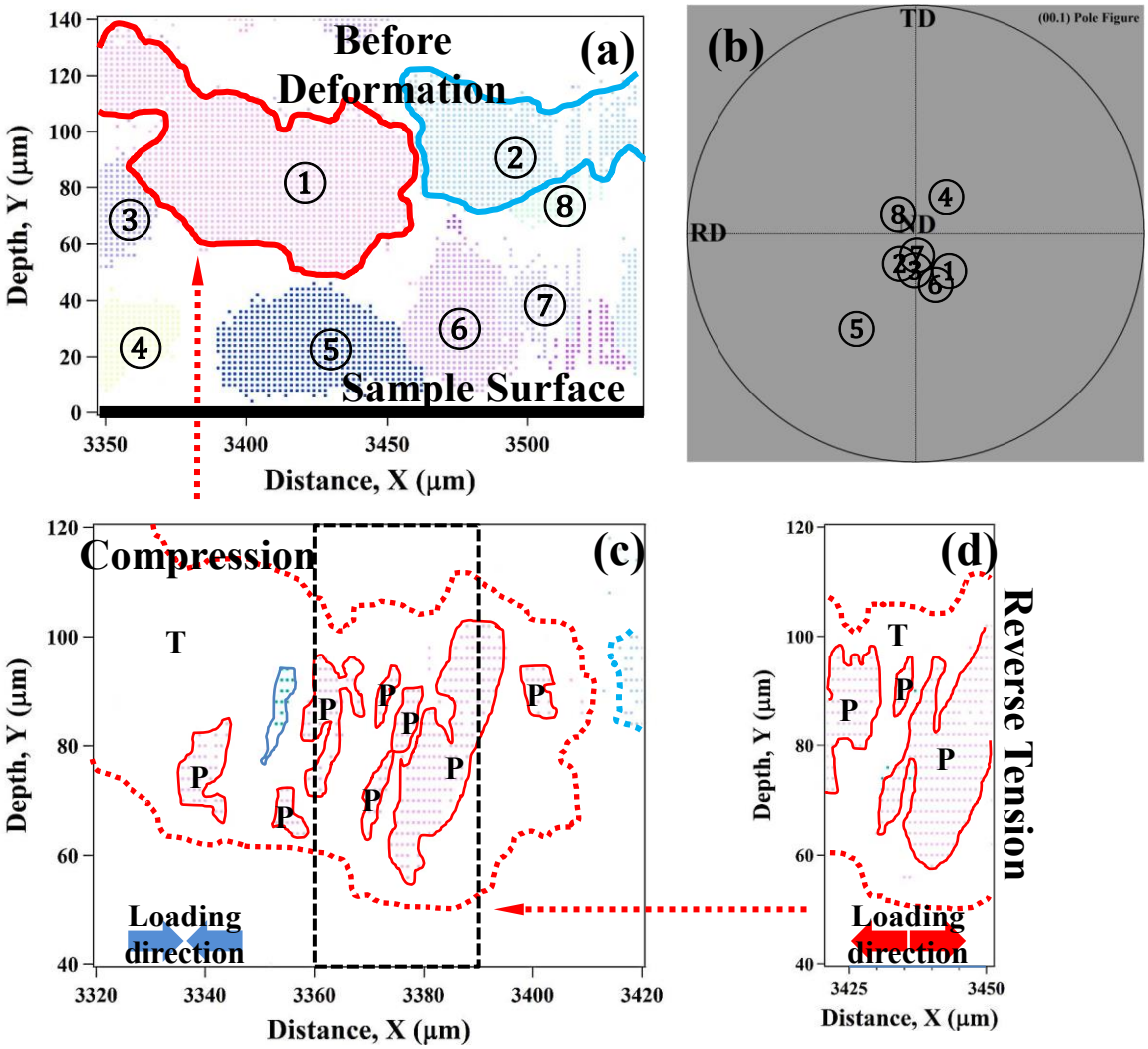

Figure 4.7 The grain orientation maps before deformation, under compression, and under reverse tension [correlated to (i), (ii), and (iii) marked in Fig. 1(b)] are demonstrated in (a), (c), and (d), respectively. The (00.1) pole figure of a wrought AZ31B Mg alloy before deformation is shown in (b). The letters P and T marked in (c) and (d) represent the "parent grain" and twins, respectively.

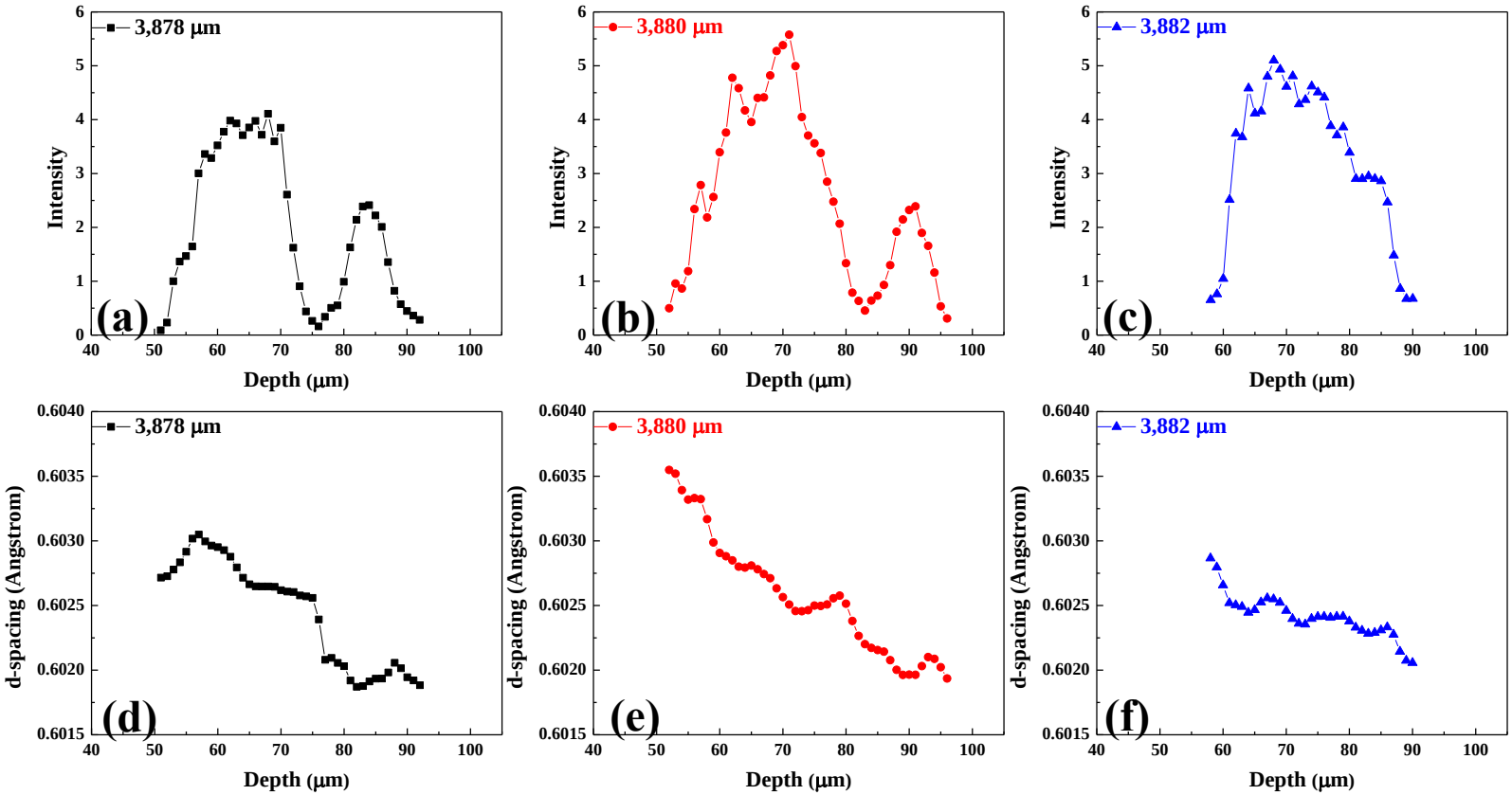

Figure 4.8 The diffraction peak intensity variations of (12.8) peak in a parent grain as a function of depth at different locations [at 3878, 3880, and 3882 μm on X-axis in Fig. 2(c)] during compression are presented in (a), (b), and (c), respectively. The d-spacing evolutions of (12.8) grain vs. depth at different locations are illustrated in (d), (e), and (f), respectively.

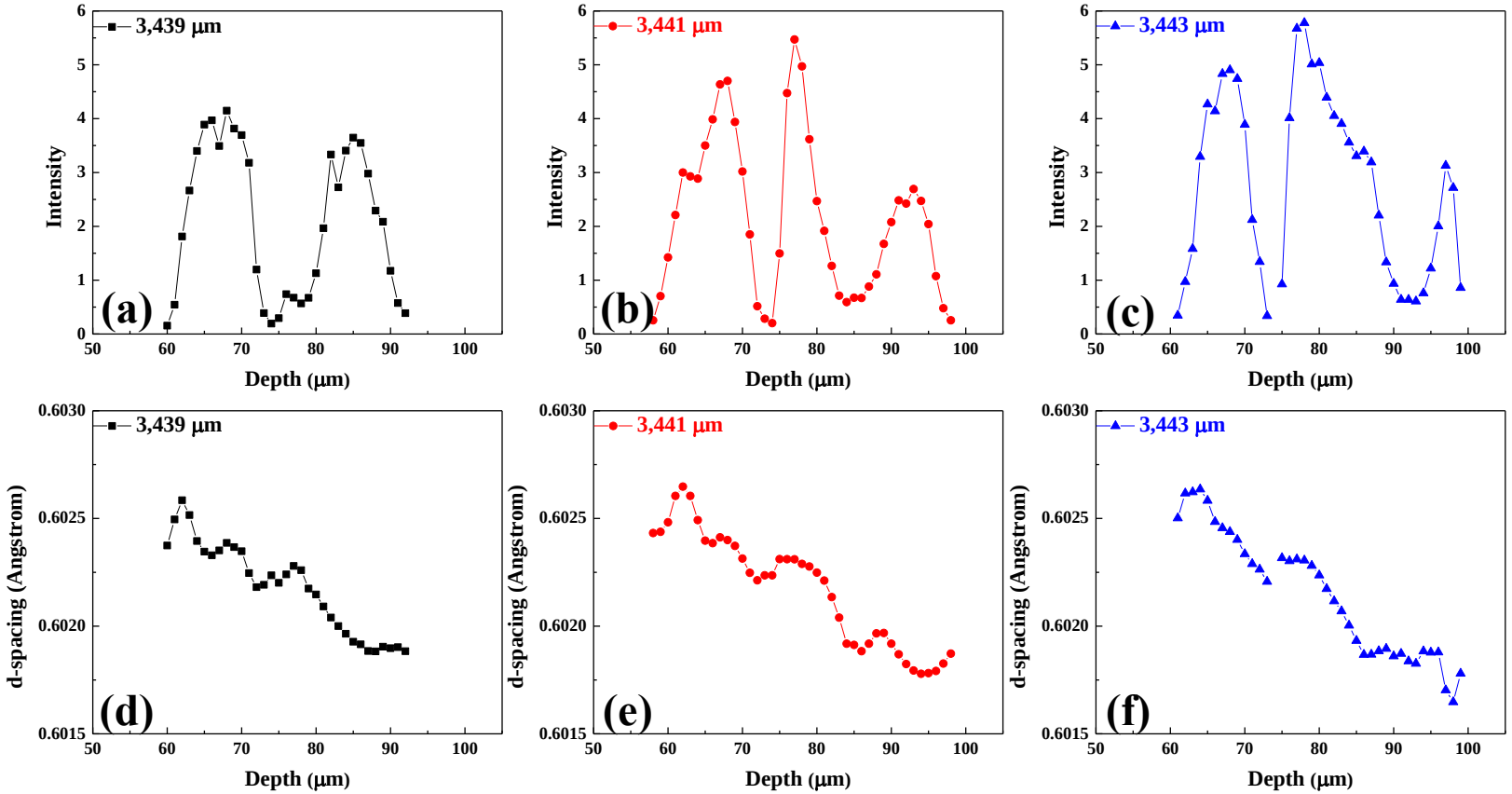

Figure 4.9 The diffraction peak intensity variations of (21.8) peak in a parent grain as a function of depth at different locations [at 3439, 3441, and 3443 μm on X-axis in Fig. 2(d)] during compression are presented in (a), (b), and (c), respectively. The d-spacing evolutions of (21.8) grain vs. depth at different locations are illustrated in (d), (e), and (f), respectively.

Figure 4.10 The two-dimensional (2-D) and three-dimensional (3-D) real-time in-situ neutron diffraction results of the measured d range during the low-cycle fatigue for: (a) the 2-D patterns in the axial direction, (b) the 2-D pattern in the radial direction, (c) the 3-D pattern in the axial direction, and (d) the 3-D pattern in the radial direction.

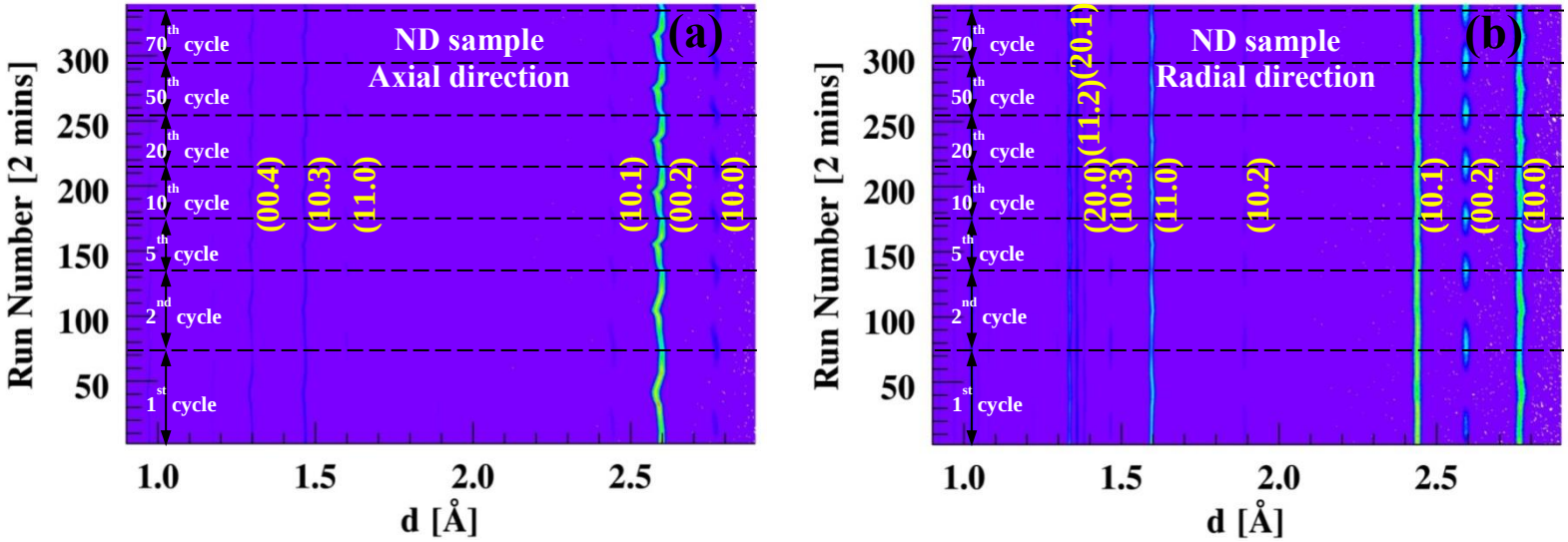

Figure 4.10 continued

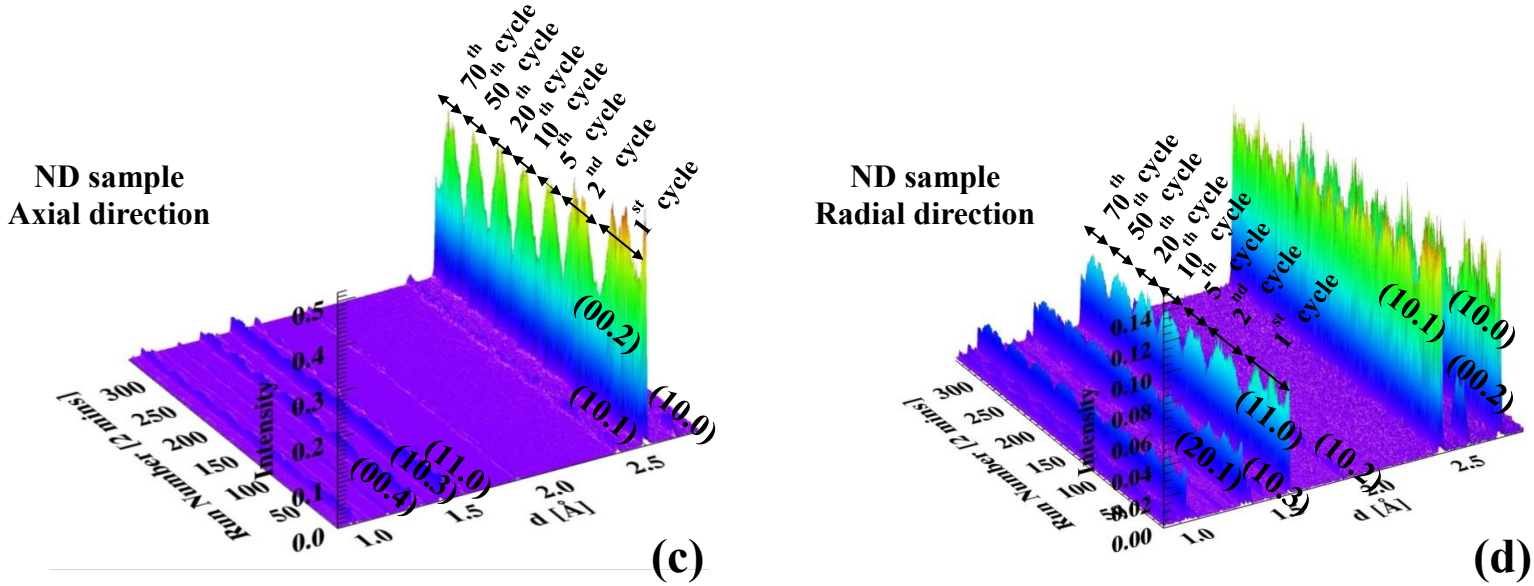

Figure 4.10 continued

Figure 4.11 (a) The hysteresis loop at different fatigue cycles under a total strain amplitude of 2% for a ND sample. (b) The peak stress, stress at zero strain, and mean stress variation during the low-cycle fatigue. (c) The yield strength evolution as a function of fatigue life. (d) The plastic strain as a function of fatigue life.

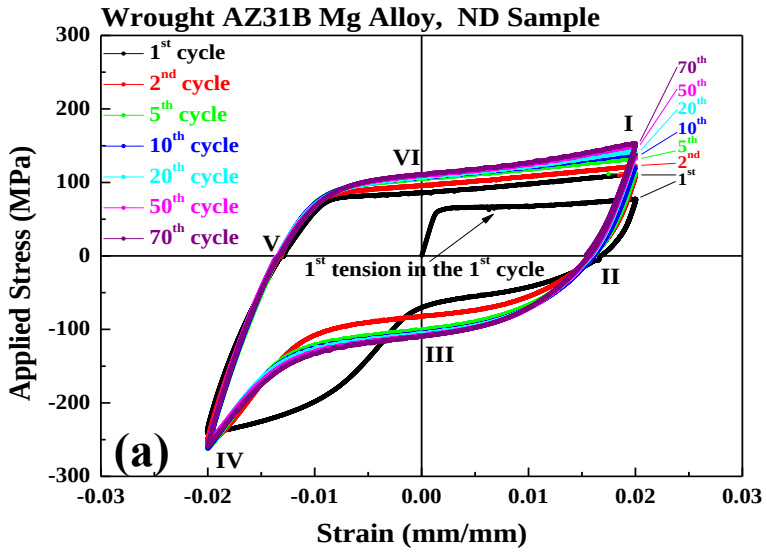

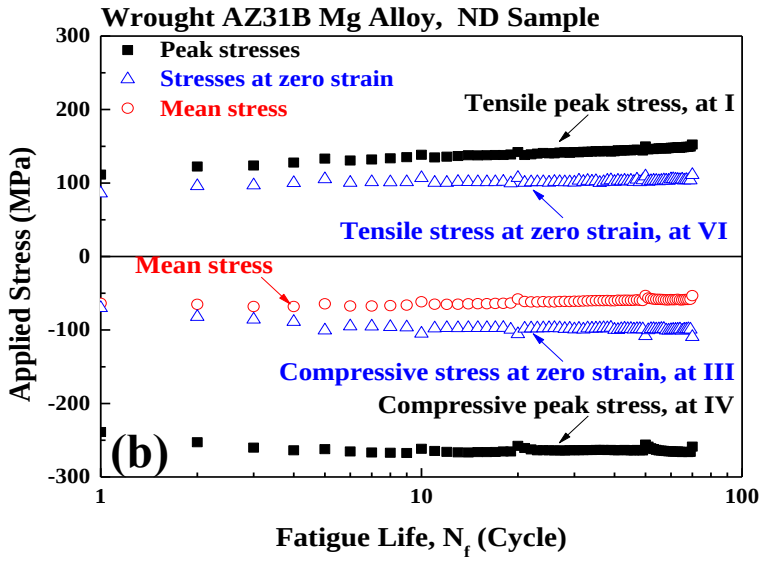

Figure 4.11 continued

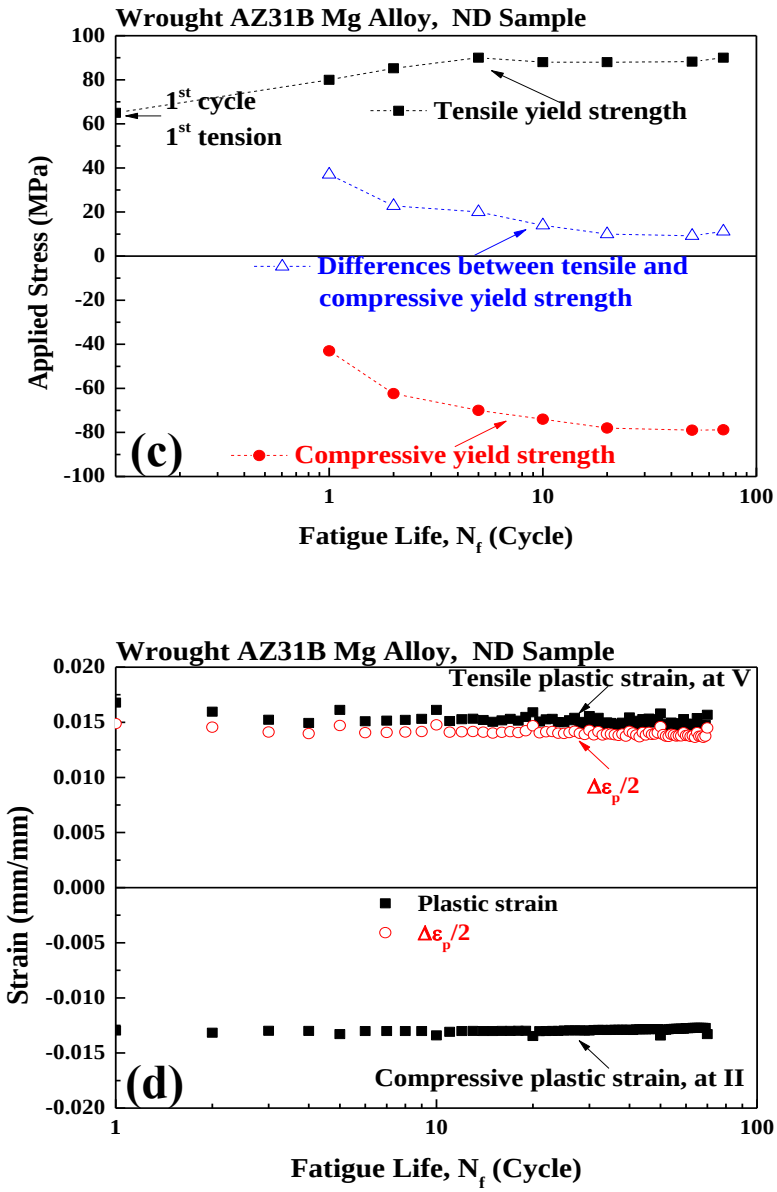

Figure 4.11 continued

Figure 4.12 The work-hardening rate as a function of stress at different fatigue cycles: (a), (b), (c), (d), (e), (f), and (g) represent the 1^{st}, 2^{nd}, 5^{th}, 10^{th}, 20^{th}, 50^{th}, and 70^{th} fatigue cycles, respectively.

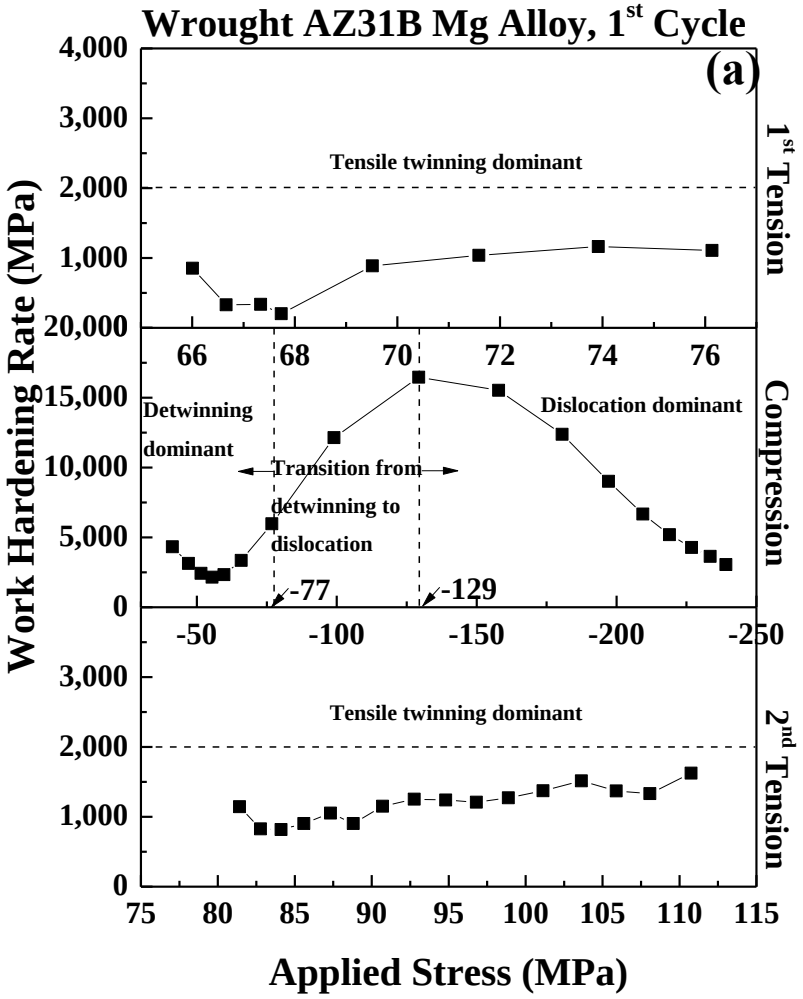

Figure 4.12 continued

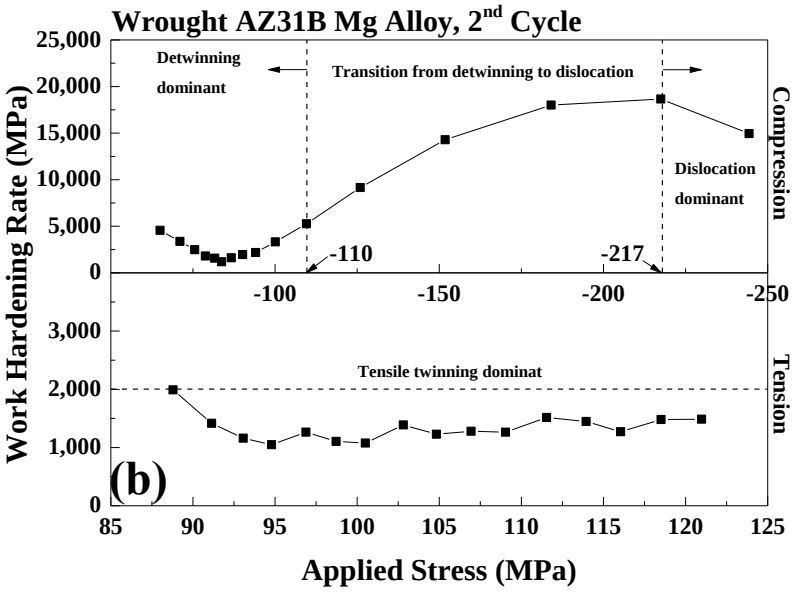

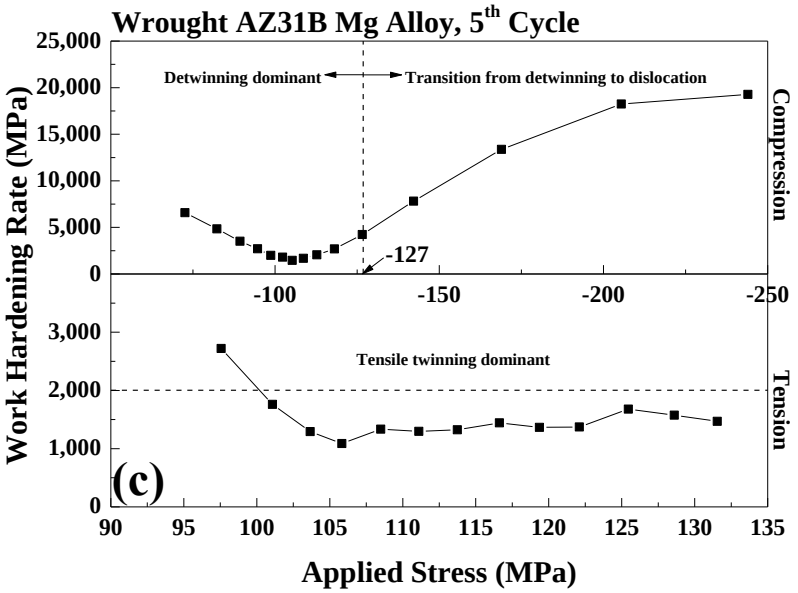

Figure 4.12 continued

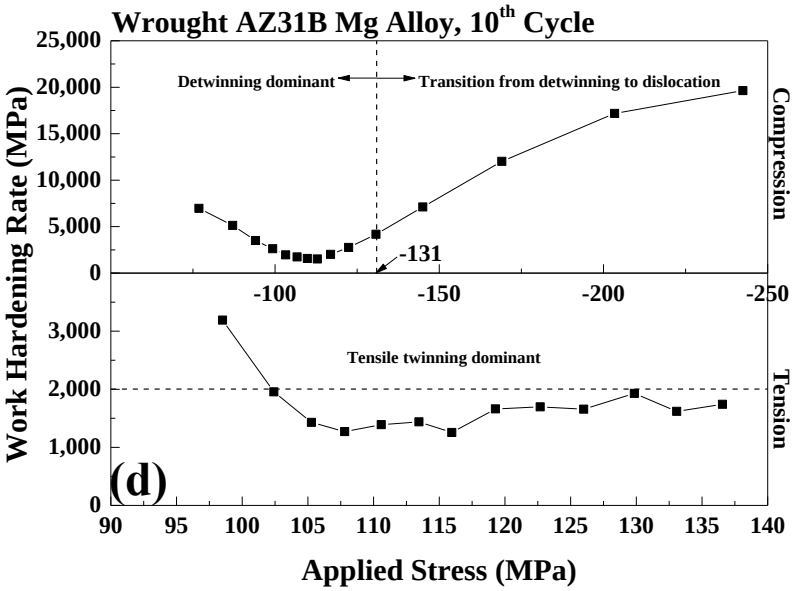

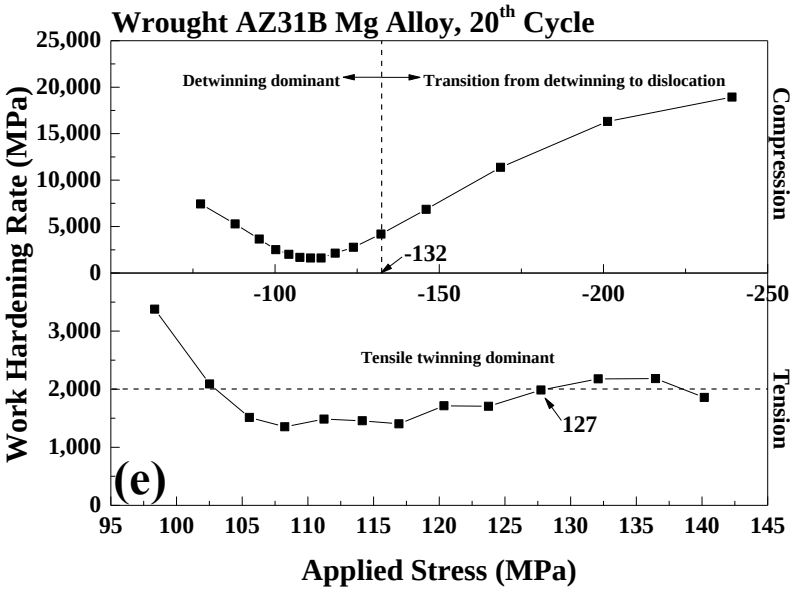

Figure 4.12 continued

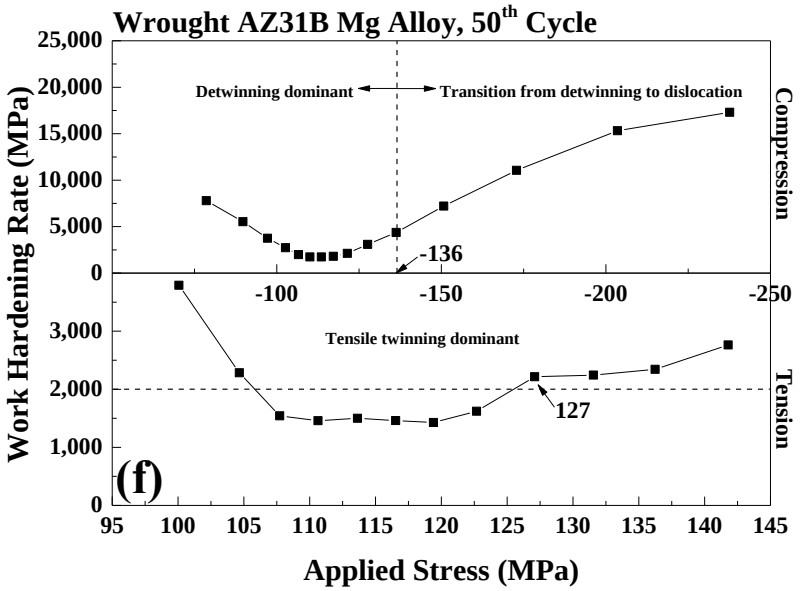

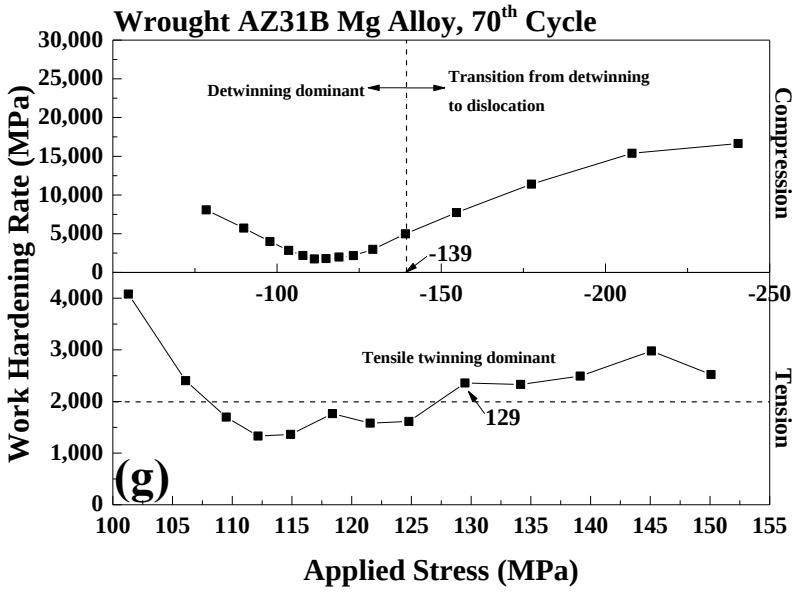

Figure 4.12 continued

Figure 4.13 The real-time in-situ neutron diffraction peak intensity, lattice strain, and peak width evolution at different fatigue cycles: (a) and (b) the diffraction peak intensity variation in axial and radial direction, respectively, (c) lattice strain changes of certain *hkl*s in the axial direction, and (d) the peak width evolution at full width at half maximum (FWHM) in the (00.2) grains in the axial direction. The mechanical stress evolution in each fatigue cycle is plotted on the secondary Y-axis in each figure.

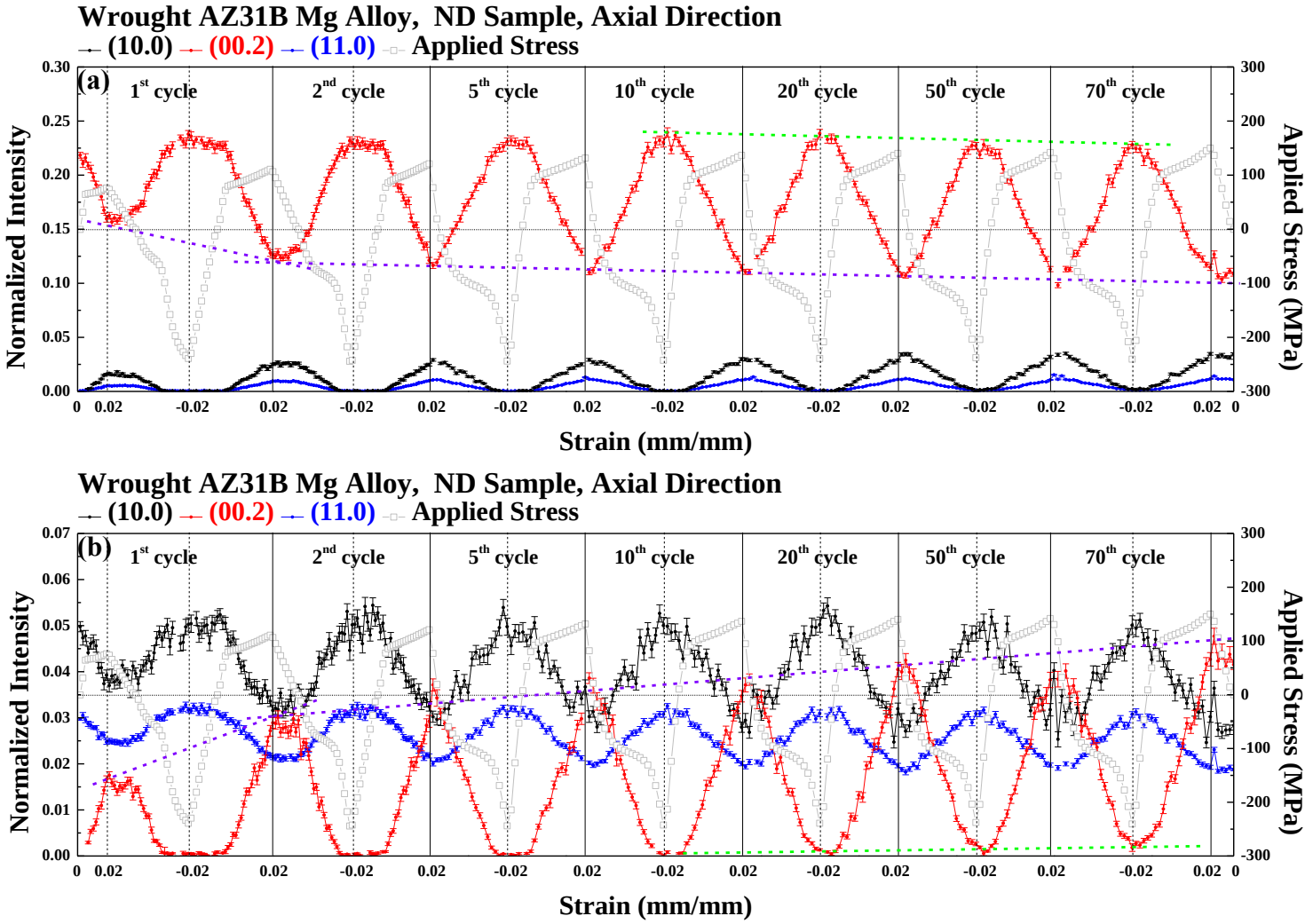

Figure 4.13 continued

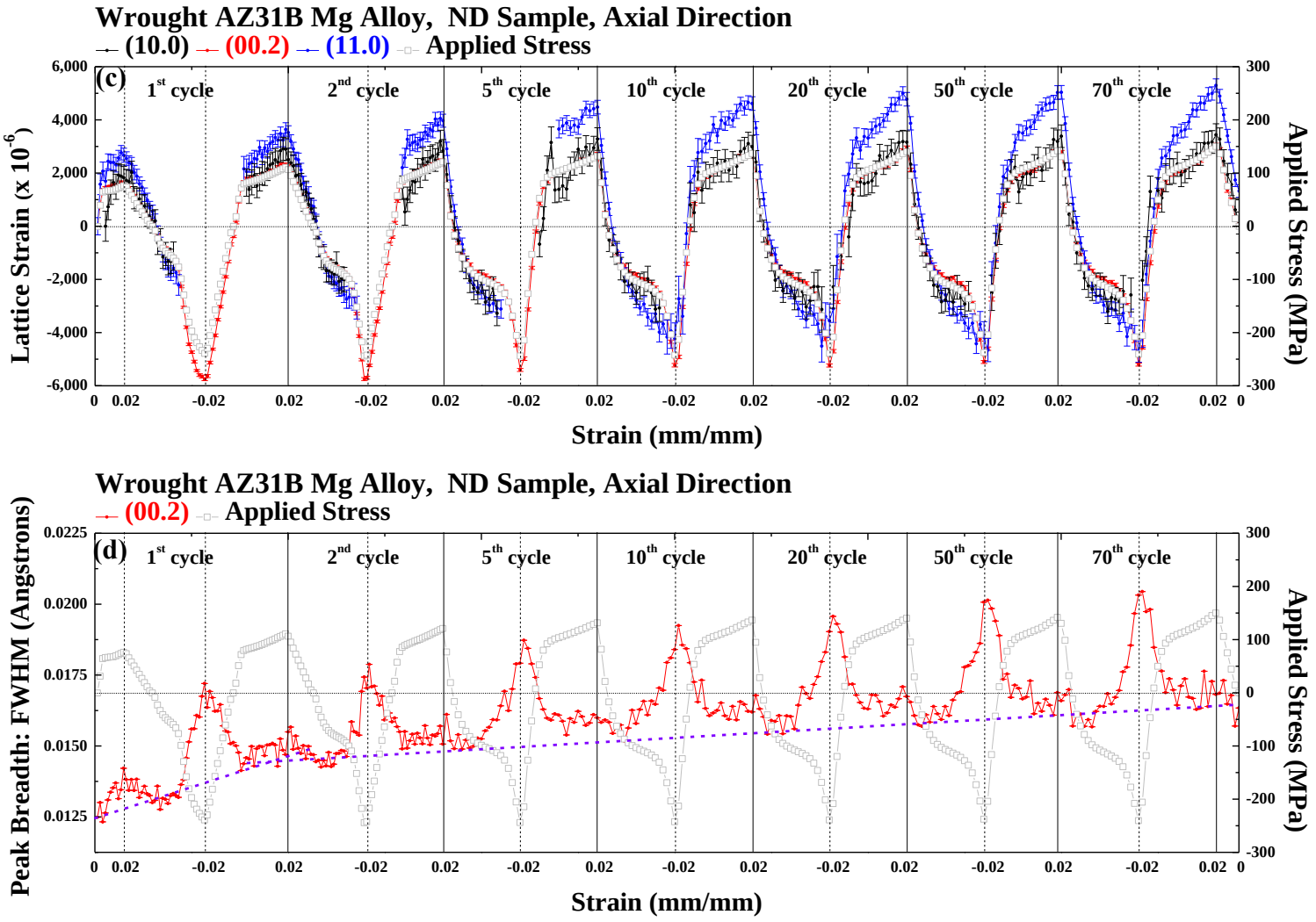

Figure 4.13 continued

Figure 4.14 The real-time in-situ neutron diffraction peak intensity evolution of certain *hkl*s in the axial direction at different low-cycle fatigue cycles: (a), (b), (c), (d), (e), (f), and (g) represent the 1^{st}, 2^{nd}, 5^{th}, 10^{th}, 20^{th}, 50^{th}, and 70^{th} cycles, respectively. The secondary Y-axis represents the macroscopic stress variation, with which the diffraction peak intensity can be correlated.

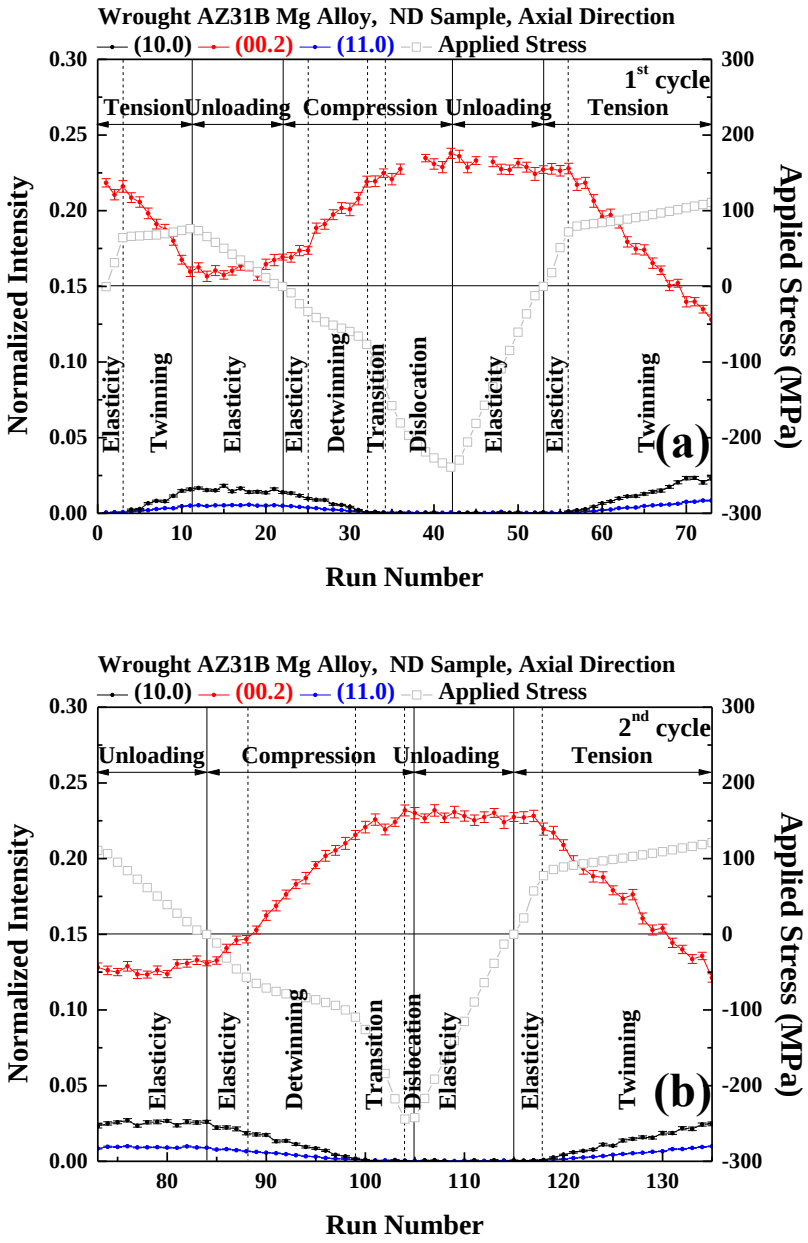

Figure 4.14 continued

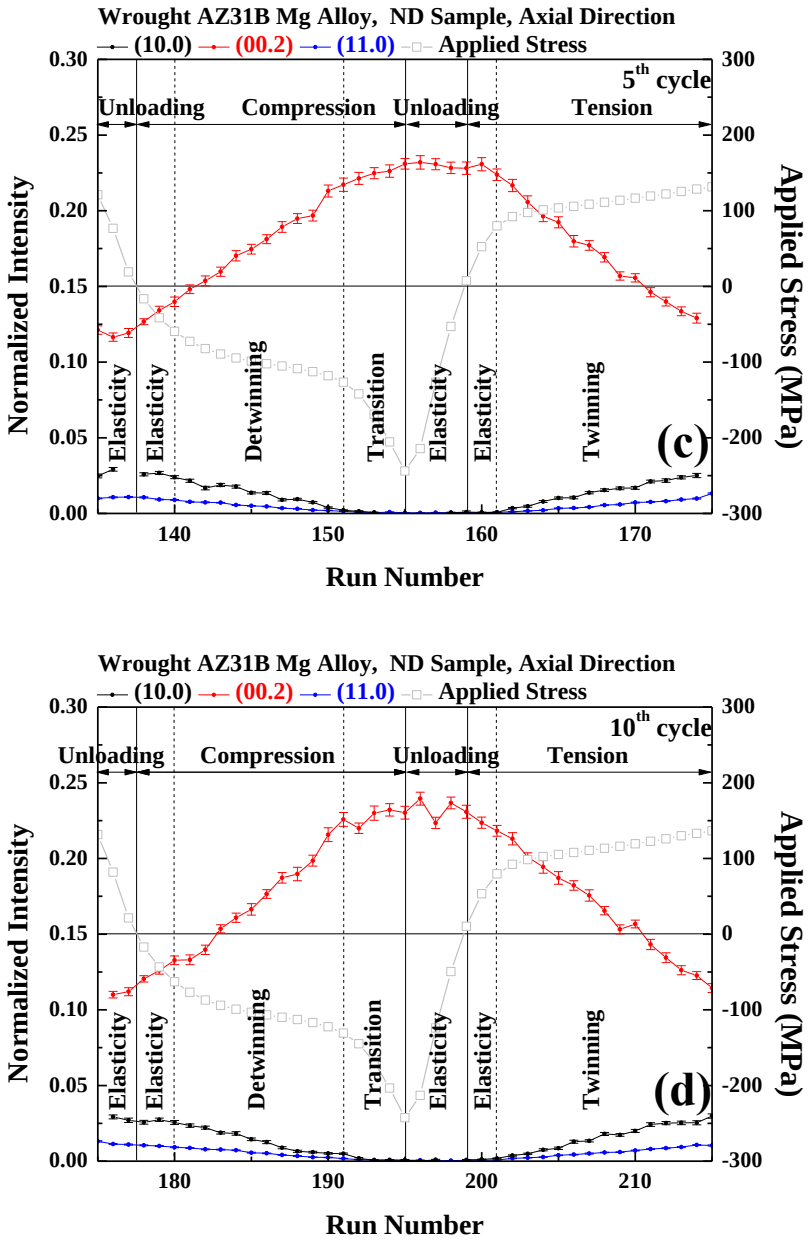

Figure 4.14 continued

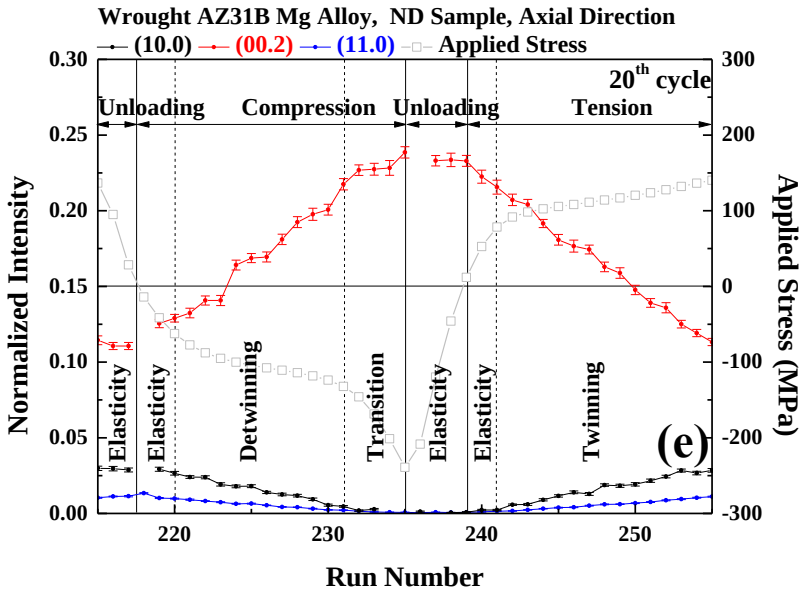

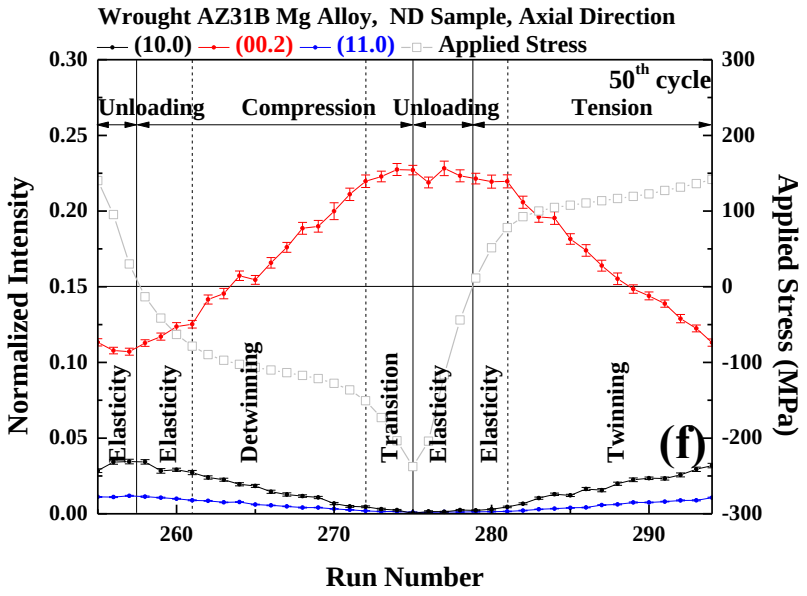

Figure 4.14 continued

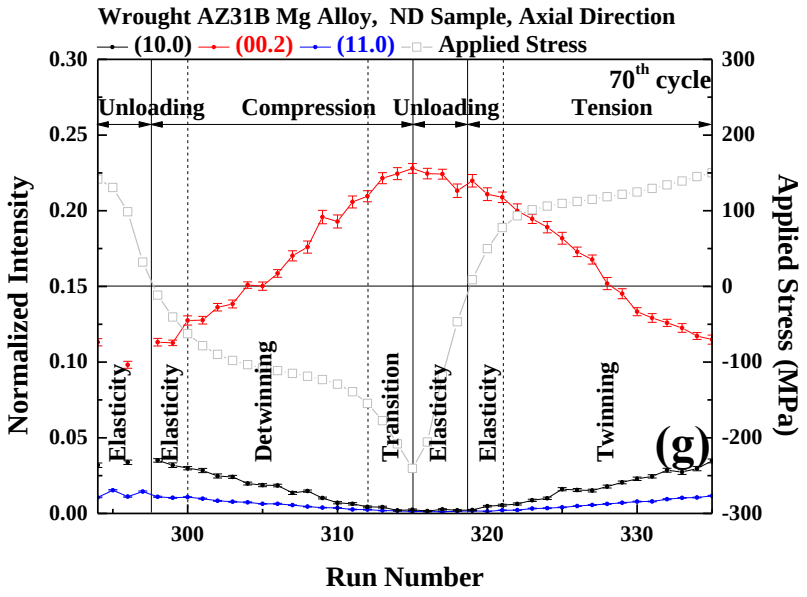

Figure 4.14 continued

Figure 4.15 The real-time in-situ neutron diffraction lattice strain evolution of the (00.2) grains in the axial direction at different low-cycle fatigue cycles: (a), (b), (c), (d), (e), (f), and (g) represent the 1^{st}, 2^{nd}, 5^{th}, 10^{th}, 20^{th}, 50^{th}, and 70^{th} cycles, respectively. The inset in Fig. 7(a) is the lattice strain evolution of (00.2) grains in the axial direction during the 1^{st} tension in the 1^{st} cycle. (h) Demonstration of the loading sequence in the 50^{th} fatigue cycle. Noted that i, ii, iii, and iv represent unloading from tension, compression, unloading from compression, and tension, respectively.

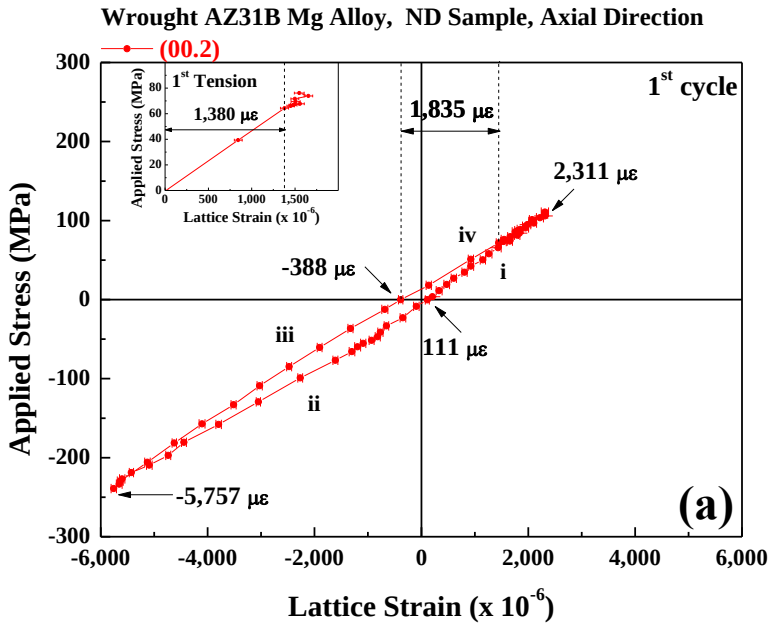

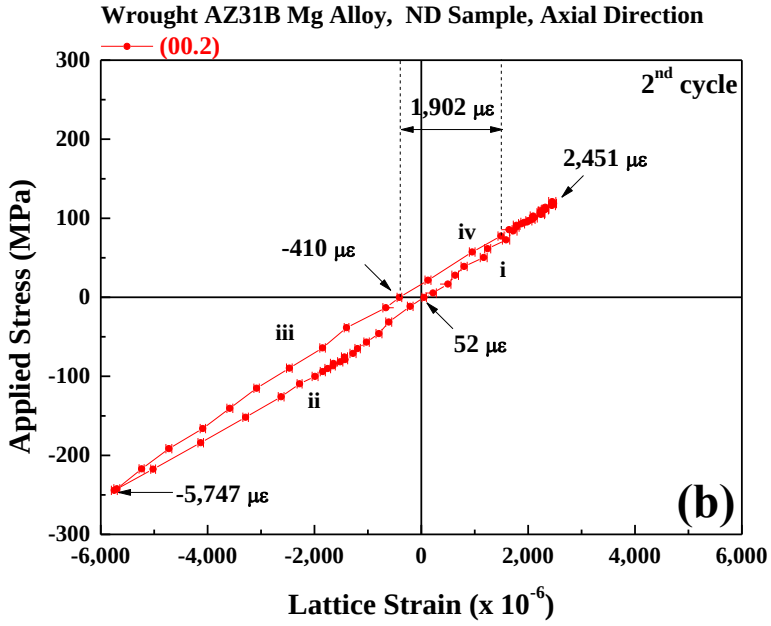

Figure 4.15 continued

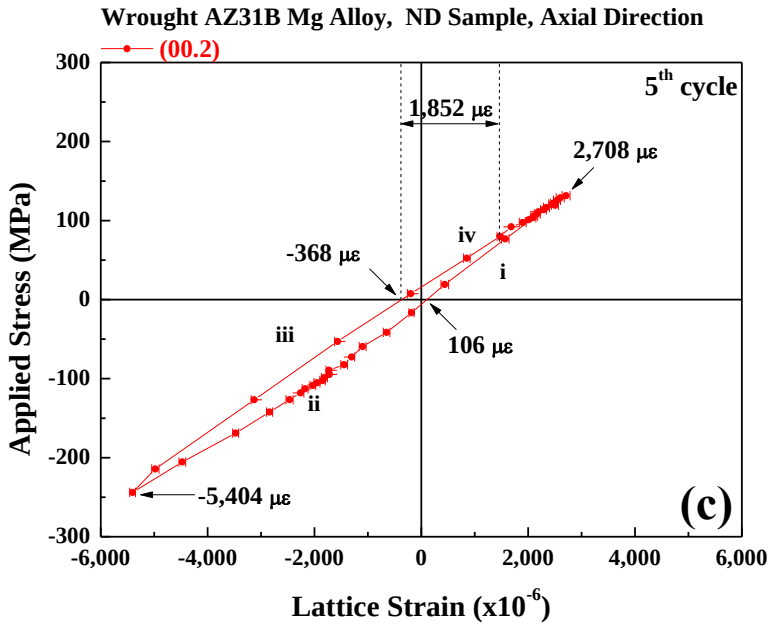

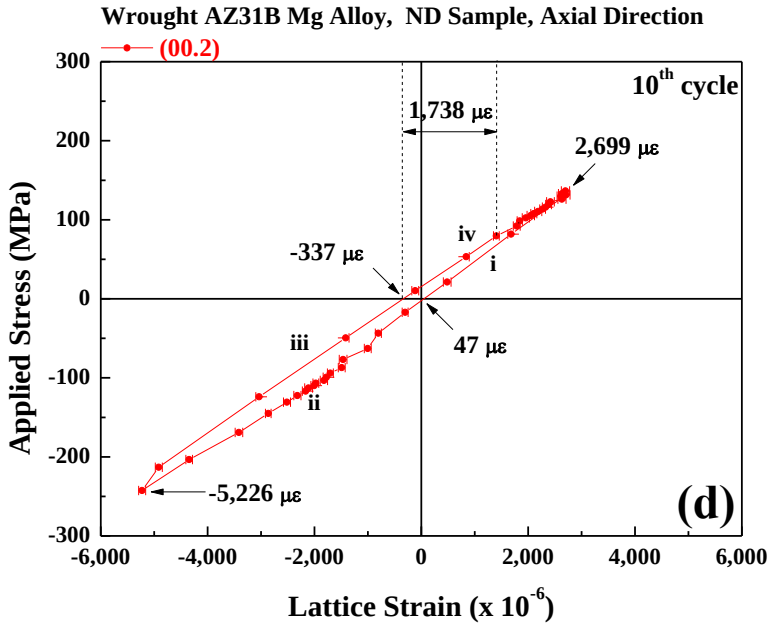

Figure 4.15 continued

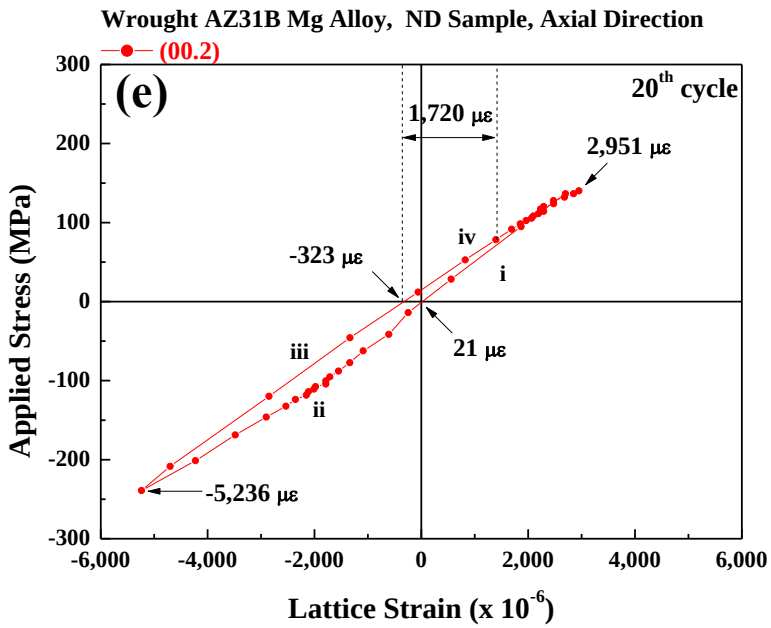

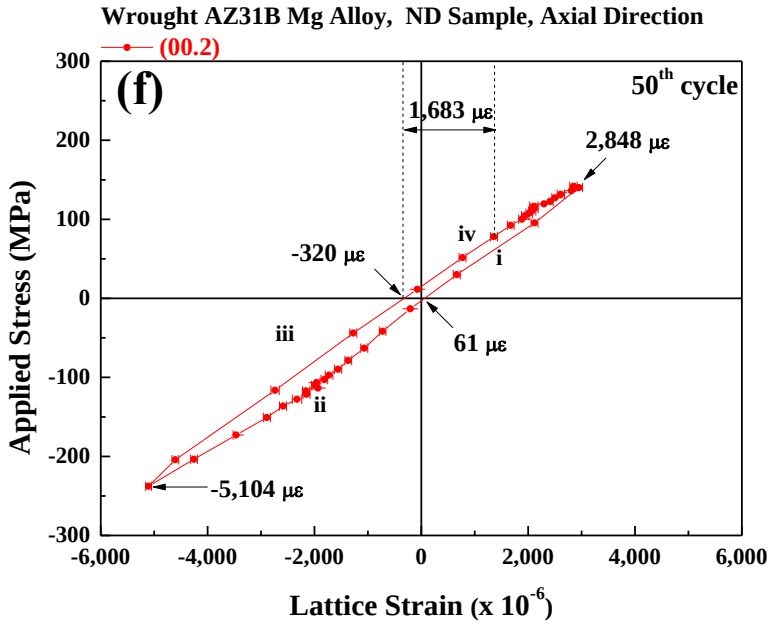

Figure 4.15 continued

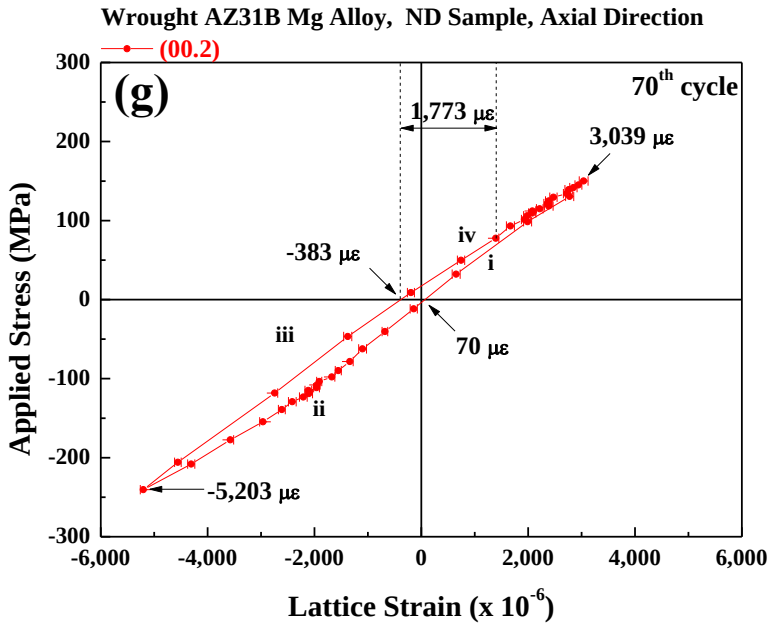

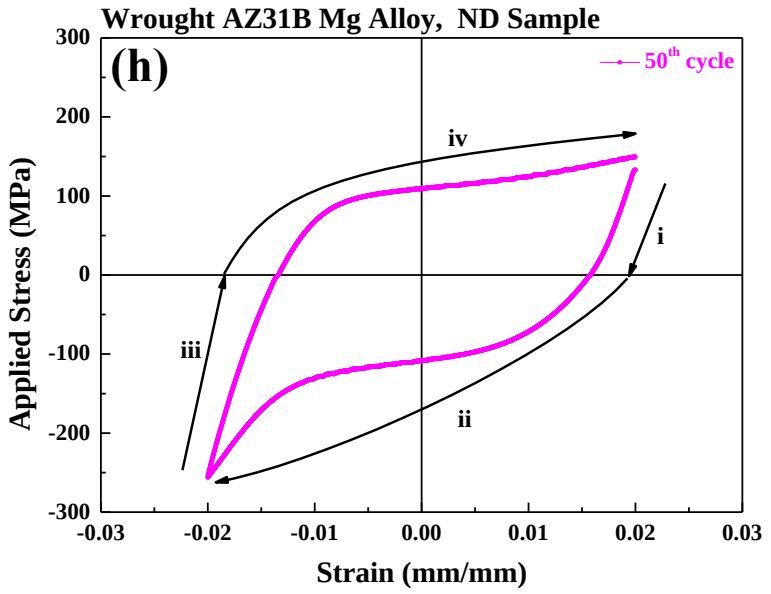

Figure 4.15 continued

Figure 4.16 (a) The stress-strain hysteresis loop of the 50^{th} fatigue cycle. (b) The area of stress-strain hysteresis loop as a function of fatigue life. (c) The peak stresses, yield stresses, and stresses at dividing point as a function of fatigue life. (d) Top: the variation of tensile peak stress, stress at dividing point between detwinning and transition region, and their difference vs. fatigue life. Bottom: Stress range in twinning dominated deformation region, stress range in detwinning dominated deformation region, and their difference vs. fatigue life.

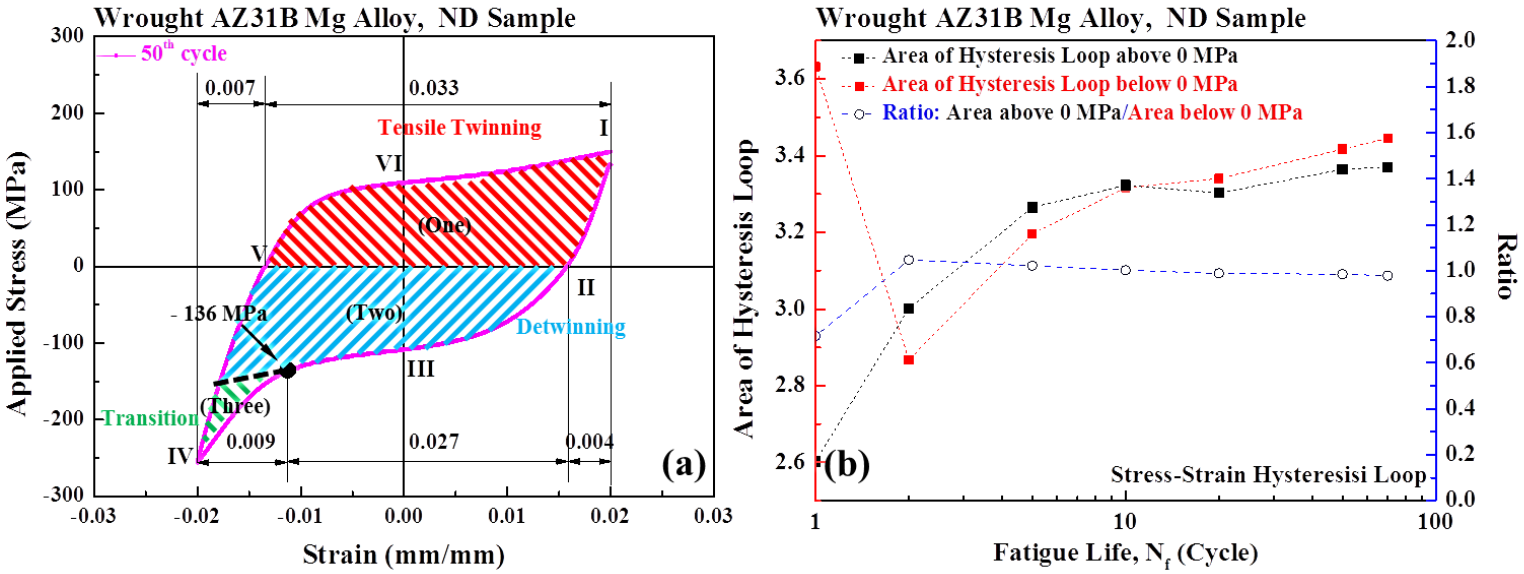

Figure 4.16 continued

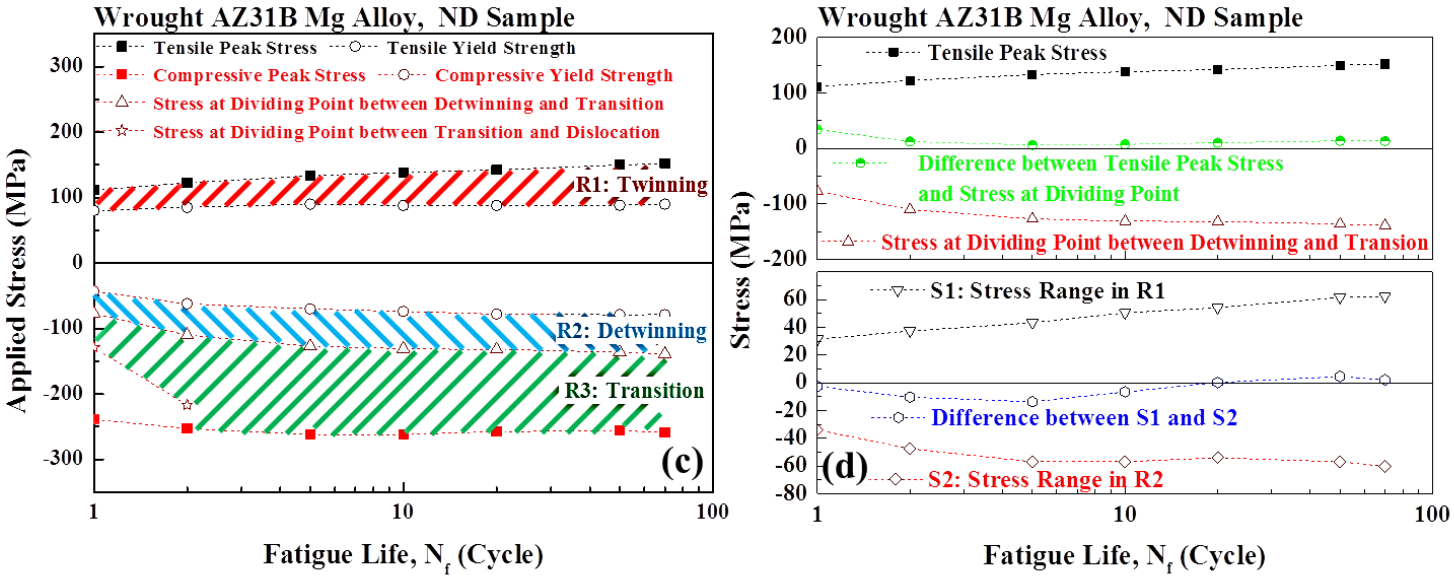

Figure 4.16 continued

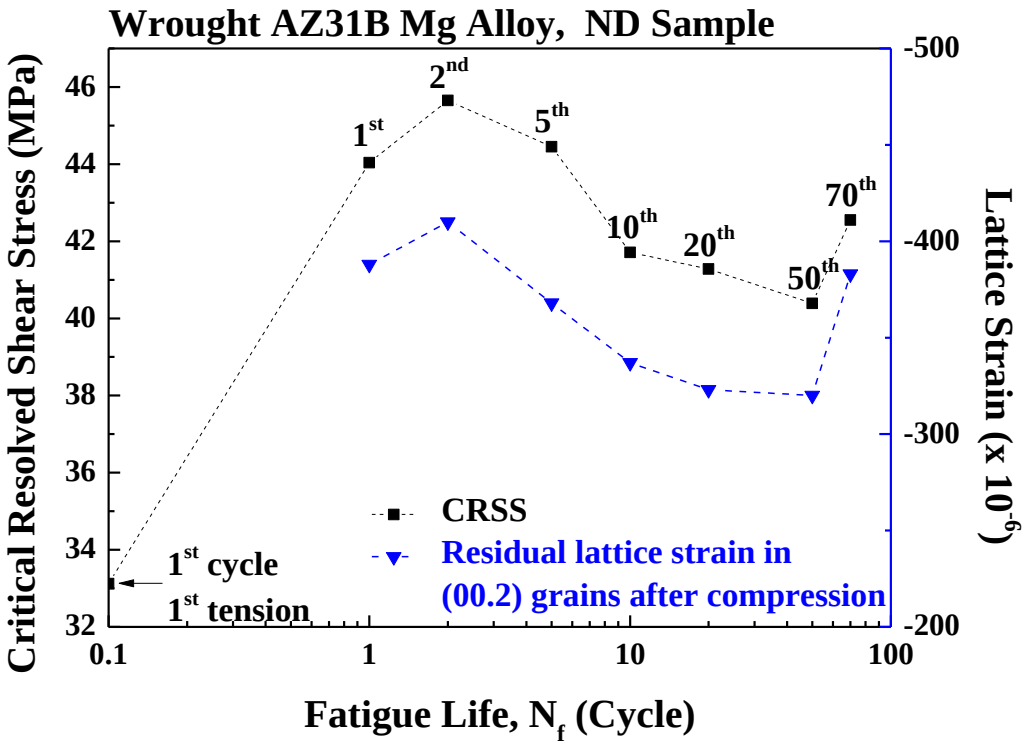

Figure 4.17 The critical resolved shear stress variation at different fatigue cycles. The residual lattice strain of (00.2) grains in the axial direction as a function of fatigue cycles is plotted on the secondary Y-axis.

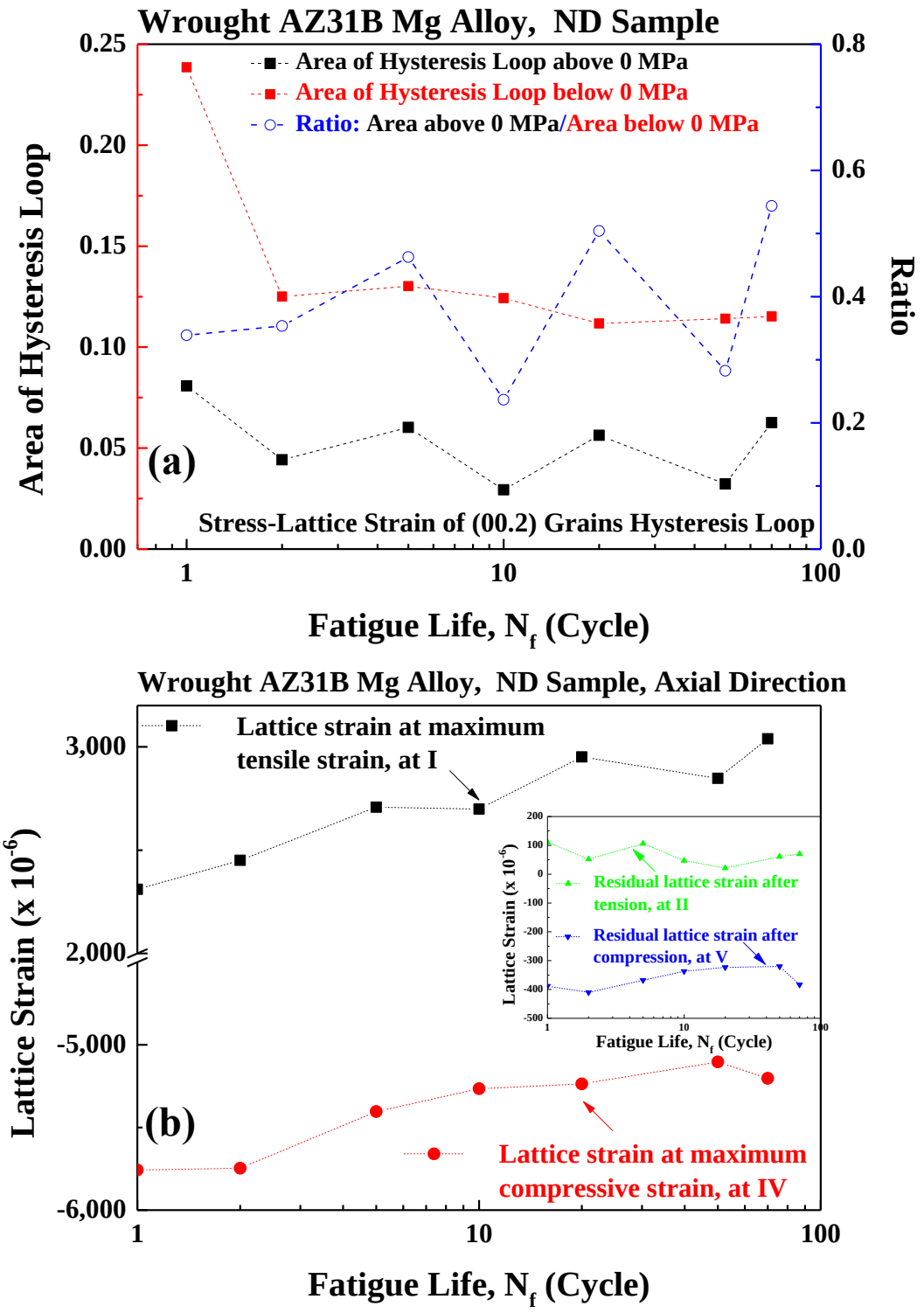

Figure 4. 18 (a) The area of stress-lattice strain of (00.2) grains hysteresis loop vs. fatigue life. (b) The maximum and minimum lattice strain variation as a function of fatigue life. The inset is the residual lattice strain changes during low-cycle fatigue. The Roman numeral I, II, IV, and V are indicated in Fig. 4.11(a).

Figure 4.19 The maximum and minimum lattice strain variation as a function of fatigue life. The inset is the residual lattice strain changes during low-cycle fatigue.

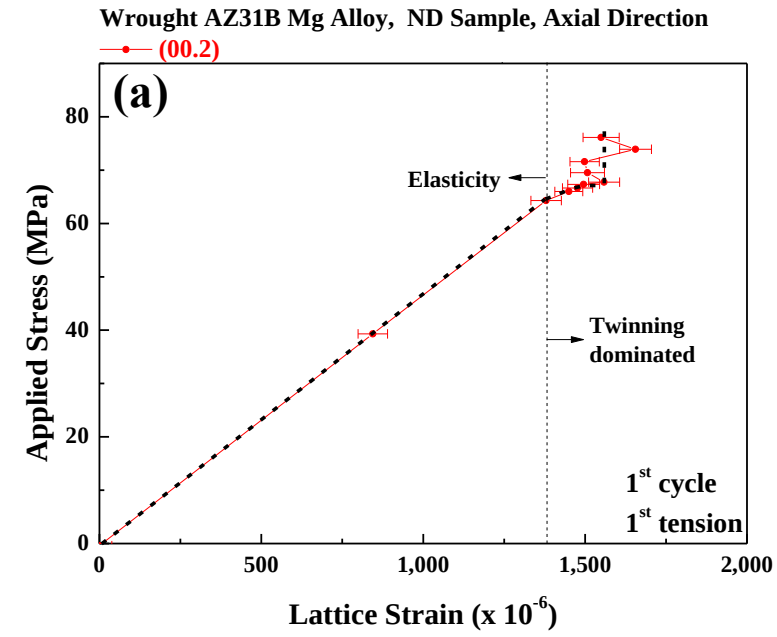

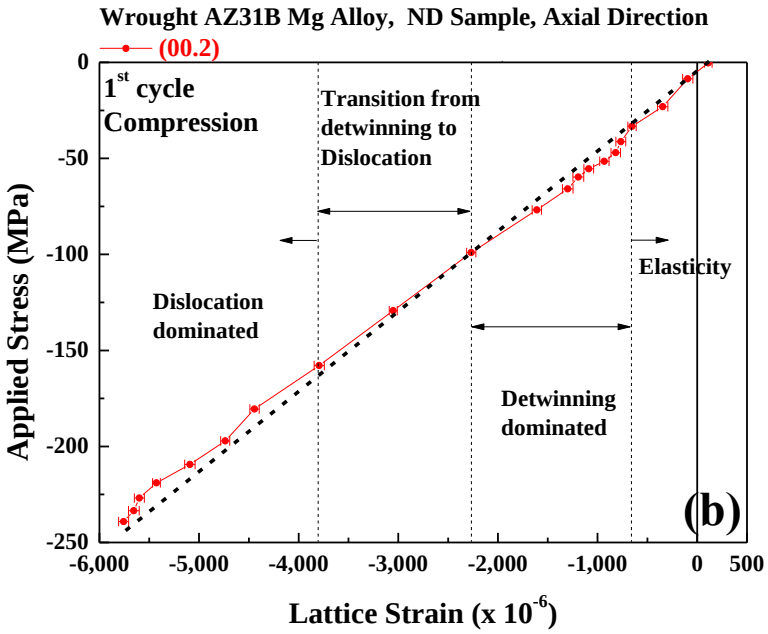

Figure 4.19 continued

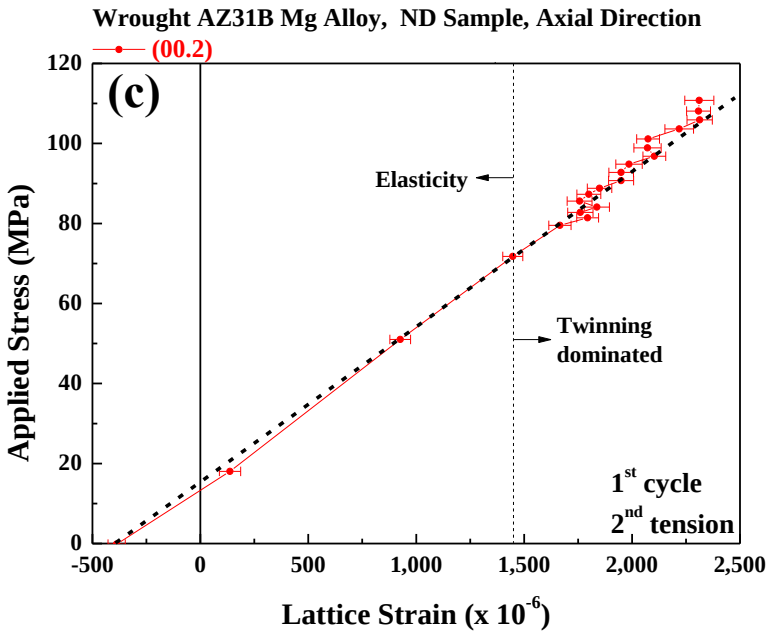

Figure 4.19 continued

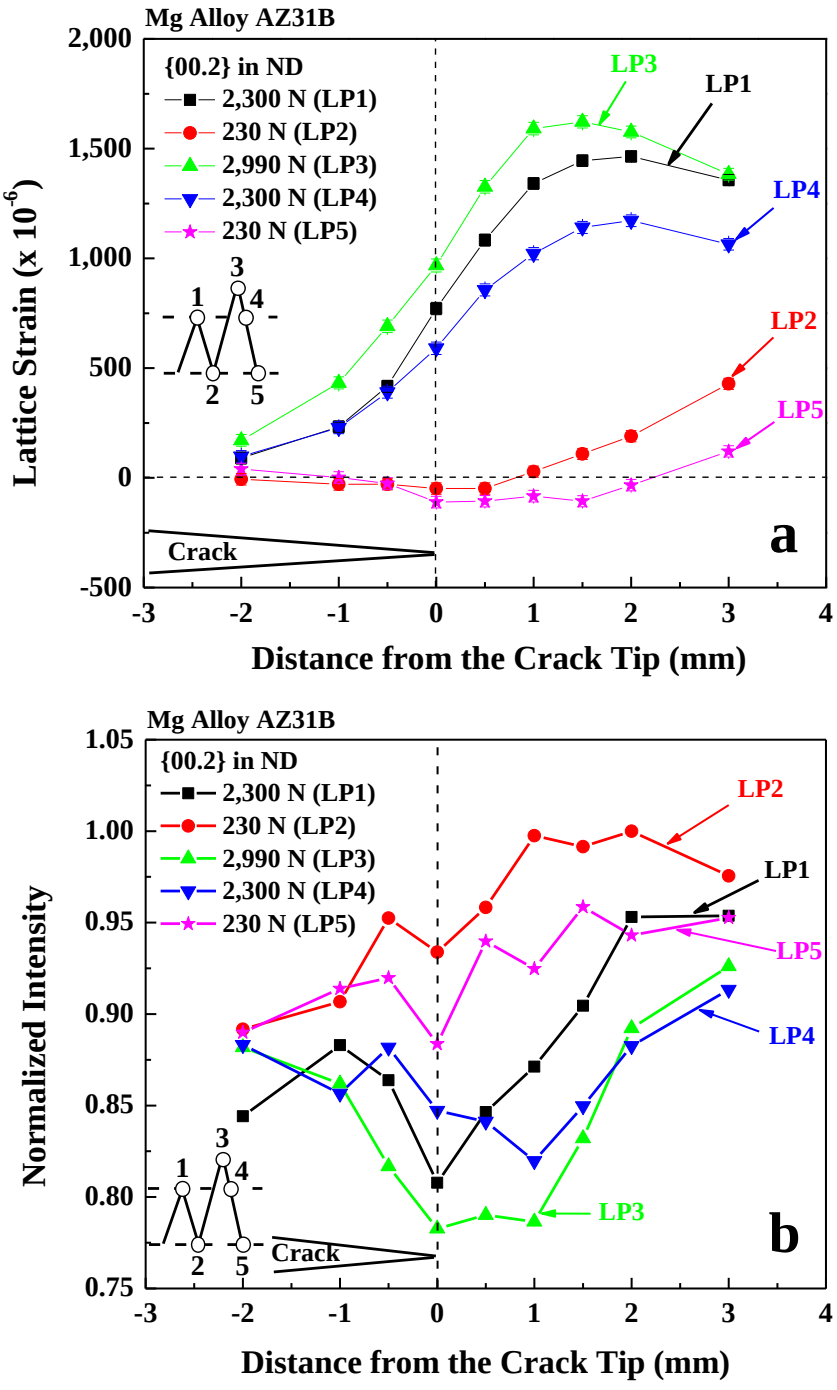

Figure 4.20 In-situ neutron-diffraction results obtained from the {00.2} reflection in bank 1: (a) lattice strain and (b) diffraction peak intensity evolution is measured at the five different loadings (marked with a blue circle, Fig. 3.4(d) during loading-unloading cycles.

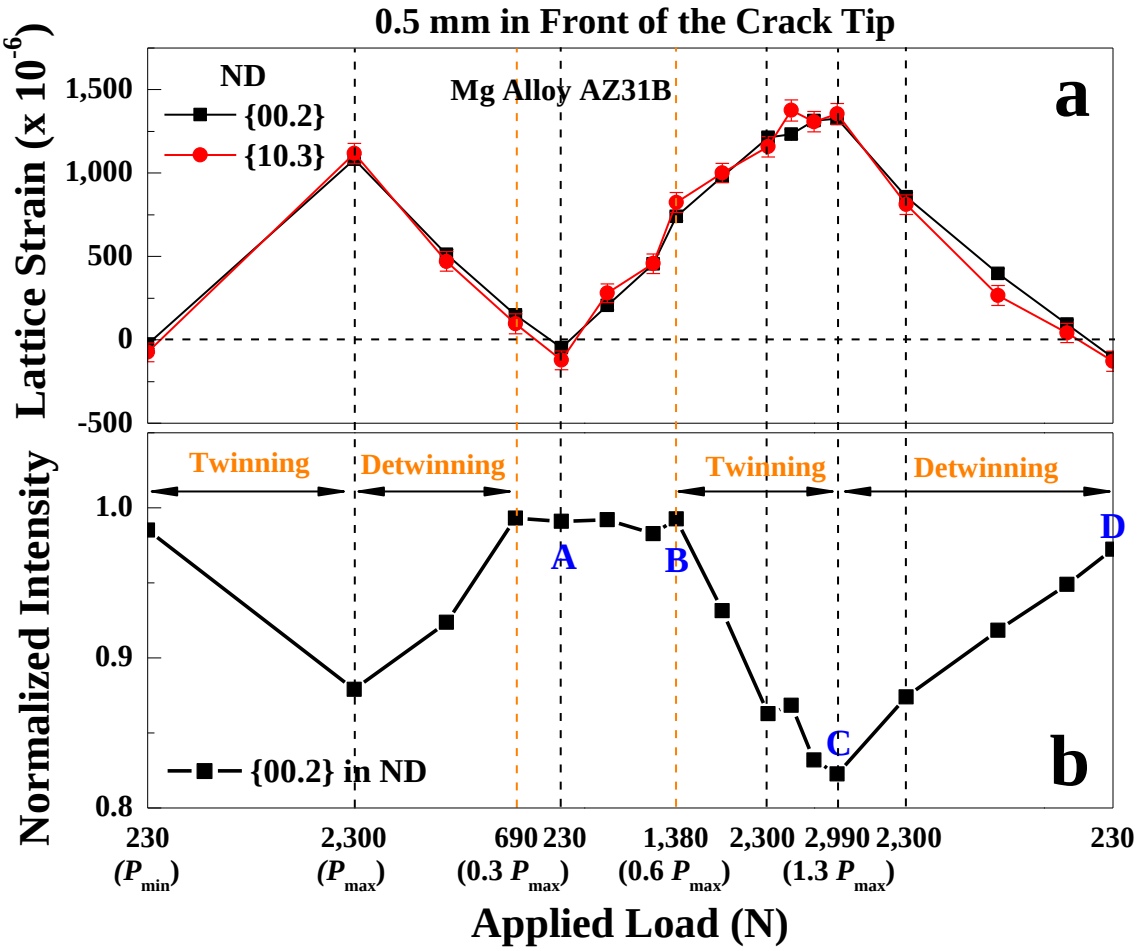

Figure 4.21 In-situ neutron-diffraction results measured at 0.5 mm in front of the crack tip: (a) the internal-strain evolution is examined as a function of the applied load [marked with an orange triangle, Fig. 3.4(d)] for the loading-unloading-overloading-unloading sequence. (b) the {00.2} peak intensity variation, which is parallel to the loading direction, is presented to describe the twinning-detwinning behavior during the loading-path change.

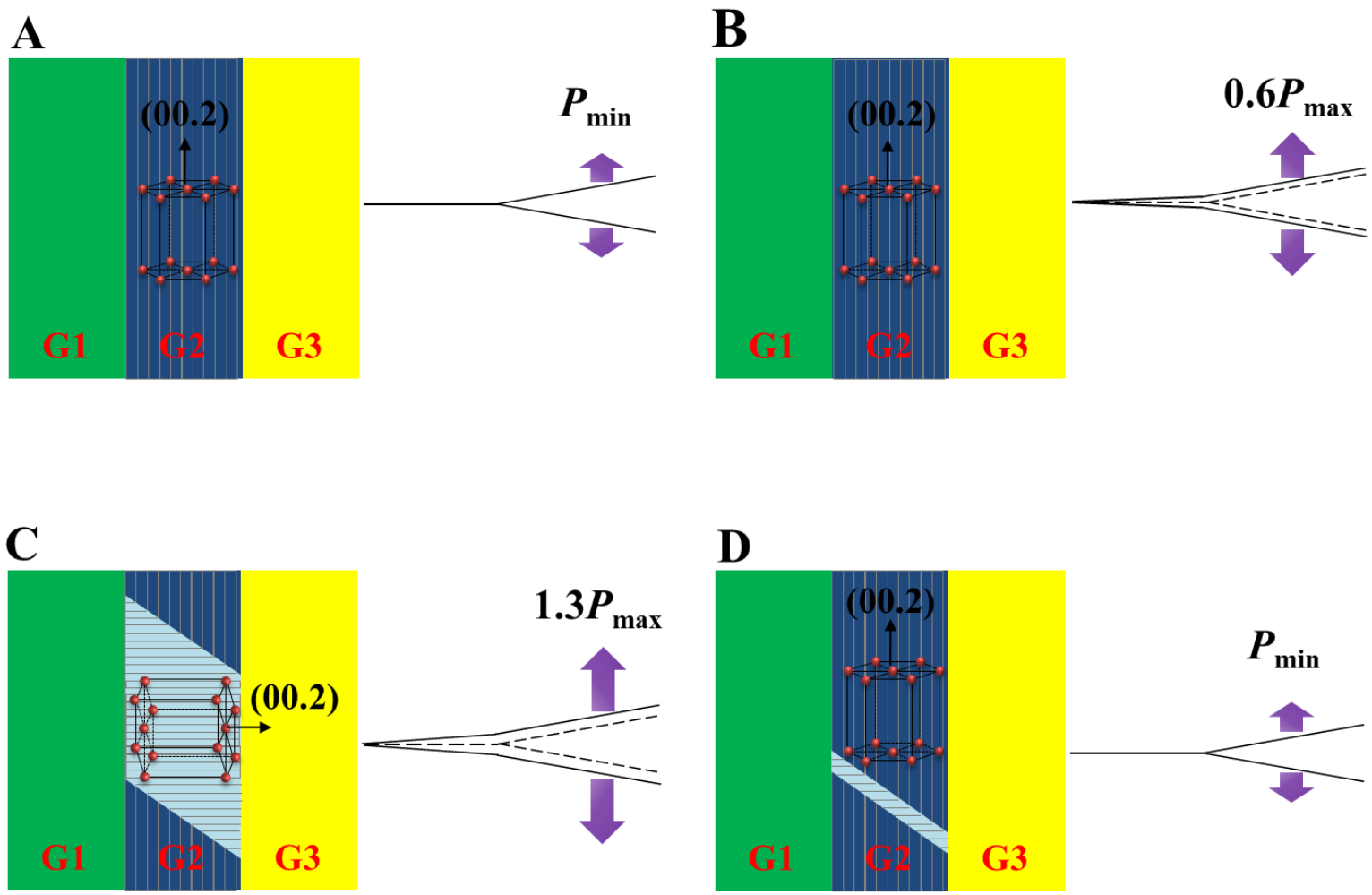

Figure 4.22 The evolution of microstructures under applied loads (i.e., A, B, C, and D) marked in Fig. 4.21(b).

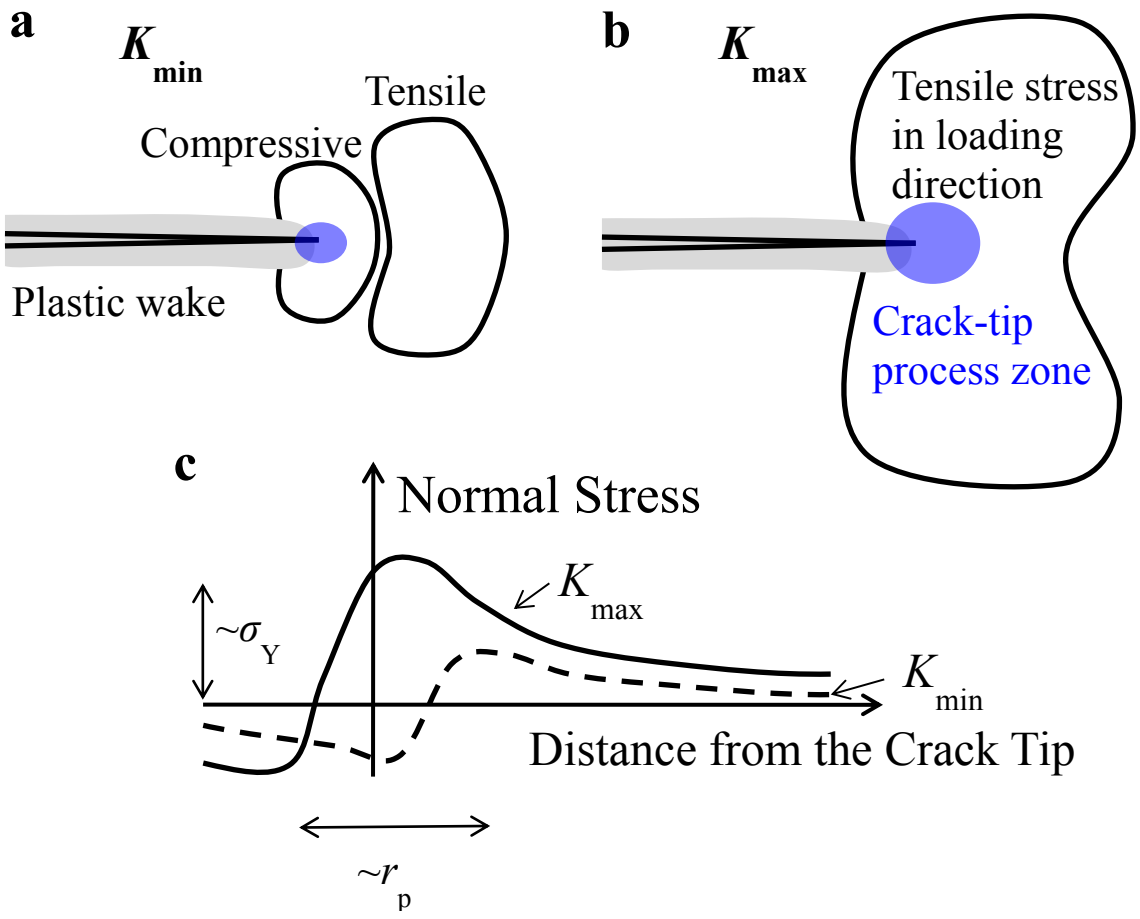

Figure 4.23 Schematic illustration of the deformation fields near the fatigue crack tip: (a) and (b) tensile and compressive stress zones at K_{min} and K_{max}, respectively. (c) stress distributions along the crack plane.

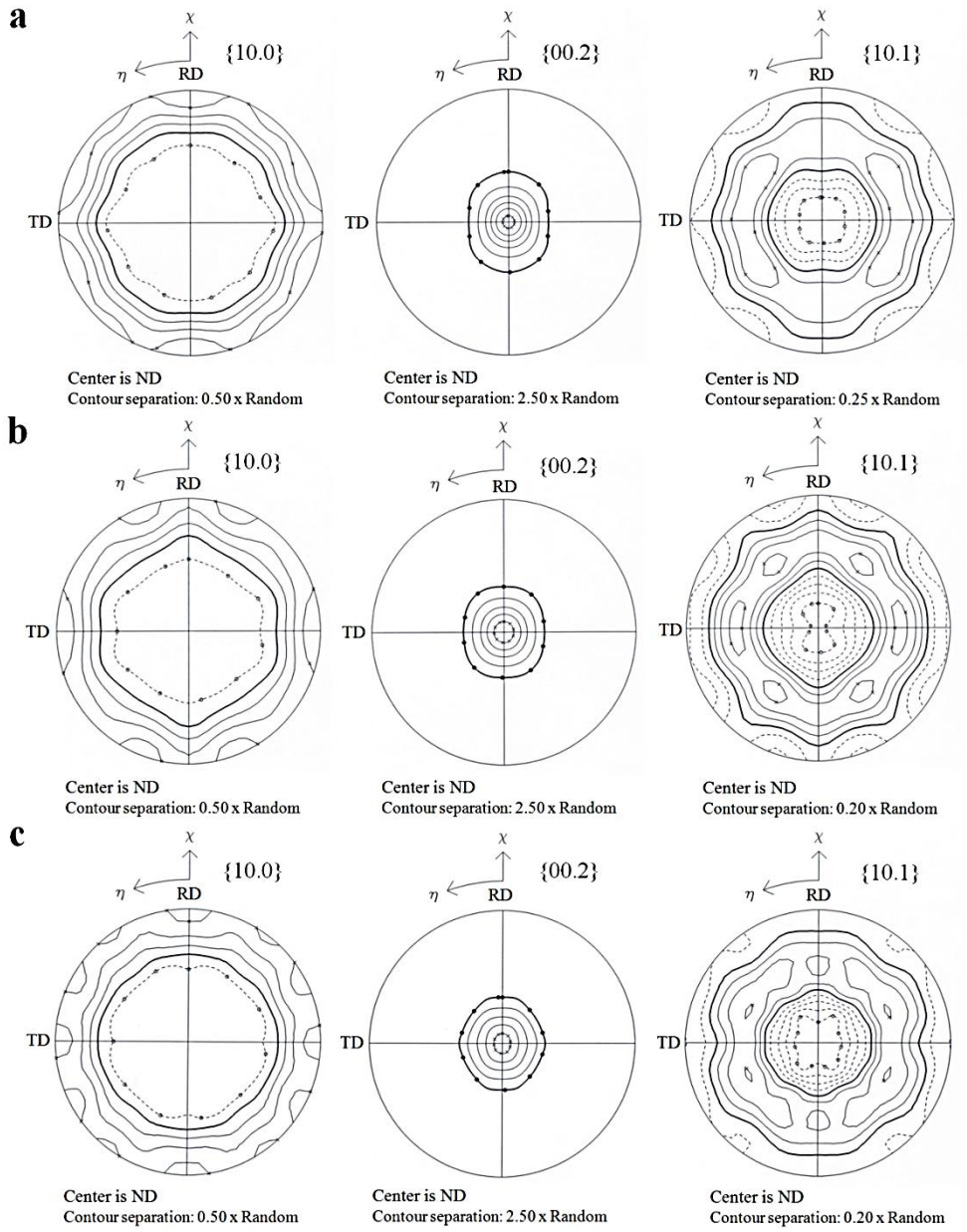

Figure 4.24 Neutron-diffraction texture measurement results: (a) texture is measured at the locations covering 3 to 5.2 mm far away from the crack tip, where the material was deformed elastically. (b) texture is measured at the locations covering 0.5 to 2.7 mm right in front of the crack tip, where the material was deformed plastically. (c) texture is measured at the locations covering –2.7 to –0.5 mm behind the crack tip, where the material was already subjected to the severe plastic deformation followed by fracture. Note that the center of the pole figure corresponds to the ND, which is the loading direction. The pole figures are contoured in multiples of random distribution (m.r.d) with the thick solid black line corresponding to 1 m.r.d. The contour levels above and below 1 m.r.d are given by solid and dotted lines, respectively.

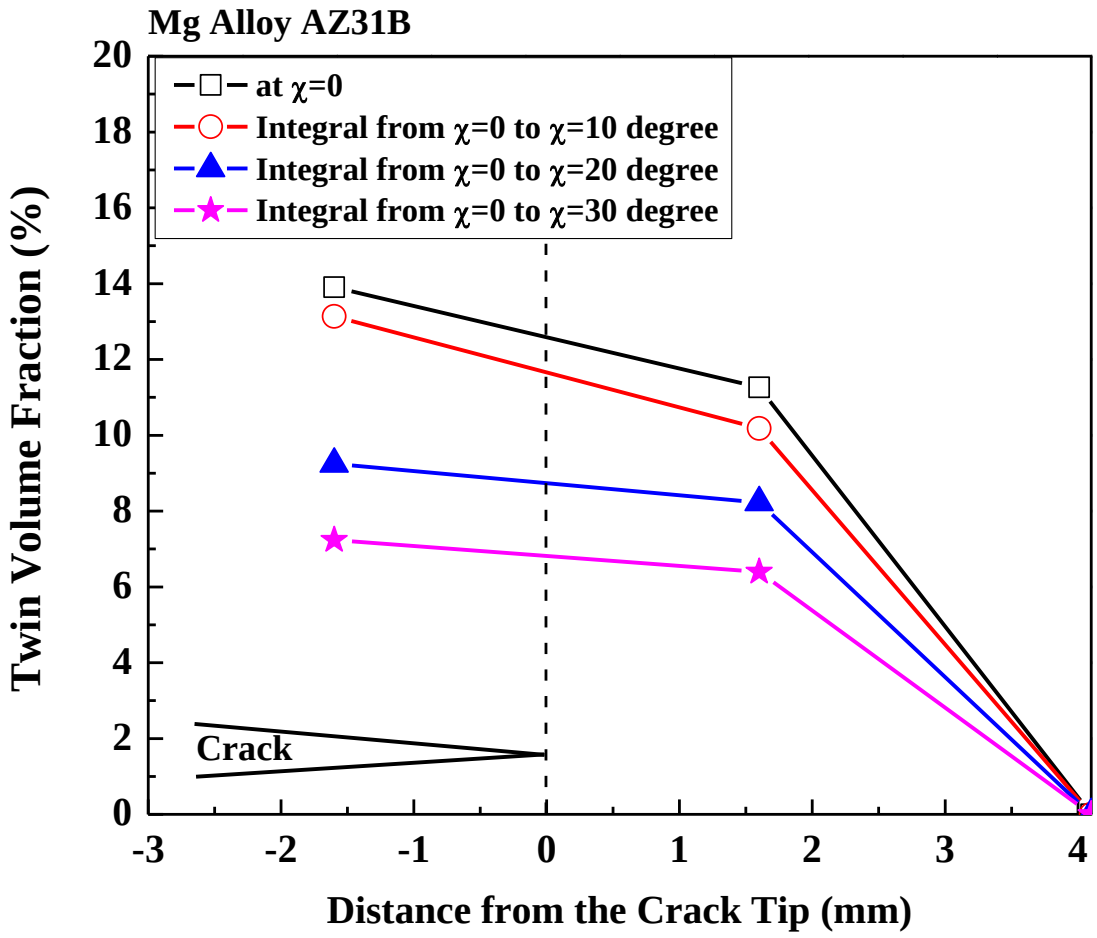

Figure 4.25 Volume fraction of residual extension twins at various locations away from the crack tip.

VITA

Wei Wu was born in Tianjin, China, on April 22, 1980. He graduated with his B. S. degree from Department of Materials Science and Engineering, at Shenyang University of Technology, China, in 2002. He earned his M. S. degree from Department of Materials Science and Engineering, at Shenyang University of Technology, China, in 2007. In January 2009, he started his doctoral study in the Department of Materials Science and Engineering at the University of Tennessee, Knoxville, USA and obtained his Ph.D. degree in December 2013.